Low cycle fatigue of shape memory alloys

Yahui Zhang

▶ To cite this version:

Yahui Zhang. Low cycle fatigue of shape memory alloys. Material chemistry. Université Paris Saclay (COmUE), 2018. English. NNT : 2018SACLY004 . tel-01880307

HAL Id: tel-01880307
https://pastel.hal.science/tel-01880307

Submitted on 24 Sep 2018

HAL is a multi-disciplinary open access archive for the deposit and dissemination of scientific research documents, whether they are published or not. The documents may come from teaching and research institutions in France or abroad, or from public or private research centers.

L'archive ouverte pluridisciplinaire **HAL**, est destinée au dépôt et à la diffusion de documents scientifiques de niveau recherche, publiés ou non, émanant des établissements d'enseignement et de recherche français ou étrangers, des laboratoires publics ou privés.

NNT : 2018SACLY004

Thèse de doctorat

Low cycle fatigue of shape memory alloys

Thèse de doctorat de l'Université Paris-Saclay
préparée à L'ENSTA PARISTECH

École doctorale n°579 sciences mécaniques et énergétiques, matériaux et géosciences (SMEMAG)
Spécialité de doctorat: Mécanique des solides

Thèse présentée et soutenue à Palaiseau, le 22 juin 2018, par

M. ZHANG Yahui

Composition du Jury :

M. Jean-Baptiste LEBLOND Professeur, Université Pierre et Marie Curie	Président
M. Tarak BEN ZINEB Professeur, Université de Lorraine	Rapporteur
M. Etienne PATOOR Professeur, Georgia Tech-Lorraine	Rapporteur
M. Günay ANLAS Professeur, Bogaziçi University	Examinateur
M. Eric CHARKALUK Directeur de recherche, Ecole Polytechnique	Examinateur
M. Petr SITTNER Directeur de recherche, Institute of Physics ASCR	Examinateur
M. Ziad MOUMNI Professeur, ENSTA ParisTech	Directeur de thèse

NNT : 2018SACLY004

THÈSE DE DOCTORAT
DE
L'UNIVERSITÉ PARIS-SACLAY
PRÉPARÉE À
L'ENSTA PARISTECH

ÉCOLE DOCTORALE N°579
Sciences mécaniques et énergétiques, matériaux et géosciences (SMEMaG)

Spécialité de doctorat : Mécanique des solides

Par

M. ZHANG Yahui

Low cycle fatigue of shape memory alloys

Thèse présentée et soutenue à Palaiseau, le 22 juin 2018

Composition du Jury :

M. Jean-Baptiste LEBLOND	Professeur, Université Pierre et Marie Curie	Président
M. Tarak BEN ZINEB	Professeur, Université de Lorraine	Rapporteur
M. Etienne PATOOR	Professeur, Georgia Tech-Lorraine	Rapporteur
M. Günay ANLAS	Professeur, Boğaziçi University	Examinateur
M. Eric CHARKALUK	Directeur de recherche, Ecole Polytechnique	Examinateur
M. Petr SITTNER	Directeur de recherche, Institute of Physics ASCR	Examinateur
M. Ziad MOUMNI,	Professeur, ENSTA ParisTech,	Directeur de thèse

Dedicated to my parents.

Acknowledgements

First of all, I would like to thank my supervisor Prof. Ziad Moumni who brought me to this extraordinary field. I have known him and worked with him for six years since I started my master degree at Northwestern Polytechnical University (NPU). During the past years, he provided me the support and freedom to do anything I was interested in. I appreciate him more than he knows.

I would like to thank Prof. Zhu Jihong and Prof. Zhang Weihong, who gave me constant support during my studies in NPU; I could never find the entrance into the academic career without them.

I would also like to thank the reviewers of my thesis Prof. Ben Zineb and Prof. Patoor, and the jury members Prof. Anlas, Prof. Charkaluk, Prof. Leblond, Prof. Sittner, for their great efforts devoted to my PhD work.

It is my honor to work with all the faculty, staff, PhD students and postdocs in UME. They are: Prof. Maitournamm, Yongjun He, Alain Van Herpen, Lahcène Cherfa, Kim Pham, Anne-Lise Gloanec, Zheng Lin, Josiane Nguejio Nguimatsia, Quentin Pierron, Moez Masmoudi, Nicolas Thurieau and Marine Bayard.

Many thanks to Gu Xiaojun and Wang Jun, the great partners of the research and playing basketball. Special thanks are given to Zhang Shaobin, one of my best friends over the past 14 years. We met each other when we entered the high school; then we went to the same university and now we are working in the same lab and sharing the same office. I cannot say more because everyone who first knows this will think too much of our relationship, except his wife, Bai Wenjun, who is also my friend and cooks very well.

As I wrote on the first page, this thesis is dedicated to my parents. They know nothing about solid mechanics or thermodynamics, but they devote their whole lives to making me who I am today.

Finally, I also wish to dedicate this thesis to my girlfriend, whoever that may be; she will love my story, including the part took place here.

Publications

Journals

Zhang, Y., Zhu, J., Moumni, Z., Herpen, A. V. & Zhang, W. (2016). Energy-based fatigue model for shape memory alloys including thermomechanical coupling. *Smart Materials and Structures*, 25, 035042.

Zhang, Y., You, Y., Moumni, Z., Anlas, G., Zhu, J. & Zhang, W. (2017). Experimental and theoretical investigation of the frequency effect on low cycle fatigue of shape memory alloys. *International Journal of Plasticity*, 90, 1 – 30.

Zhang, Y., Moumni, Z., Zhu, J. & Zhang, W. (2018). Effect of the amplitude of the training stress on the fatigue lifetime of niti shape memory alloys. *Scripta Materialia*, 149, 66 – 69.

Zhang, Y., Moumni, Z., You, Y, Zhang, W., Zhu, J. & Anlas, G. (2018). Multiscale TRIP-based investigation of low-cycle fatigue of shape memory alloys. Submitted to *Journal of the mechanics and physics of solids.*

Zhang, Y., You, Y., Moumni, Z., Anlas, G., Zhu, J. & Zhang, W. (2018). Stored-energy-based fatigue criterion for shape memory alloys. Submitted to *International Journal of Engineering Science.*

Zhang, Y., Moumni, Z., You, Y, Zhu, J. & Zhang, W. (2018). Energy-based analysis of temperature oscillation at the shakedown state in shape memory alloys. Submitted to *Continuum mechanics and thermodynamics.*

Proceedings

Zhang, Y., Moumni, Z., You, Y., & Zhang, W. (2016). Frequency effect on cyclic behavior and low-cycle fatigue of pseudoelastic shape memory alloys. In *European Congress on Computational Methods in Applied Sciences and Engineering*, Crete, Greece.

Zhang, Y., You, Y., Moumni, Z., Anlas, G., Zhu, J., & Zhang, W. (2017). A new thermomechanical low-cycle fatigue criterion for shape memory alloys. In *International Conference* *on Plasticity, Damage, and Fracture*, Puerto Vallarta, Mexico.

Abstract

The thesis proposes a multi-scale comprehensive analysis of low cycle fatigue of shape memory alloys (SMAs). First, low cycle fatigue of SMAs is experimentally investigated; comprehensive tensile-tensile fatigue tests under both stress and strain controlled loadings at different frequencies are carried out and results are discussed. Second, a new strain energy-based fatigue criterion is developed; it is shown that the use of total strain energy is a relevant parameter to predict fatigue lifetime of SMAs for different thermomechanical conditions and under different types (strain-control or stress-control) loadings. A physical interpretation of the mechanism related to the low-cycle fatigue of SMAs is then provided based on the conversion of hysteresis work into dissipation and stored energy. Third, fatigue crack initiation during cyclic stress-induced phase transformation is modeled based on transformation induced plasticity (TRIP); it is shown that the maximum temperature during the cyclic loading is a relevant indicator of the fatigue of SMA. Furthermore, the effect of the macroscopic mechanical load on the the fatigue lifetime is addressed as well as the spatial location of crack initiation. Finally, a mechanical training process that allows enhancing resistance to low cycle fatigue of SMAs is proposed.

Keywords: shape memory alloys, low cycle fatigue, thermomechanical coupling, fatigue criterion, stored energy, crack initiation.

Contents

List of Figures **xv**

Nomenclature **xxiii**

1 Introduction **1**

1.1 Introduction and motivation . . . 1

1.2 Overview of shape memory alloys . . . 3

1.2.1 Martensitic transformation . . . 3

1.2.2 Shape memory effect and pseudoelasticity . . . 4

1.2.3 Applications of shape memory alloys . . . 7

1.3 Objectives and outline . . . 8

2 Experimental investigations **11**

2.1 Introduction . . . 11

2.2 Experiments . . . 13

2.2.1 Material characterization . . . 13

2.2.2 Experimental setup . . . 14

2.2.3 Experiment procedure . . . 15

2.3 Experimental results . . . 15

2.3.1 Repeatability of the experiments . . . 15

2.3.2 Stabilization of thermal and mechanical responses . . . 17

2.3.3 Thermal and mechanical response in the stabilized cycle . . . 21

2.4 Discussion . . . 23

2.4.1 Temperature evolution . . . 23

2.4.2 Mechanical response . . . 26

2.4.3 Fatigue lifetime . . . 30

2.5 Conclusion . . . 32

3 Modeling of the fatigue 35
3.1 Introduction . . . 35
3.1.1 1D criteria . . . 35
3.1.2 3D criteria . . . 36
3.1.3 Criteria including thermomechanical coupling . . . 36
3.2 Hysteresis energy-based criterion . . . 37
3.3 Strain energy based criterion . . . 40
3.4 Experimental validation of the criterion . . . 42
3.5 Conclusion . . . 44

4 Energy-based analysis of the cyclic behavior and fatigue of SMAs 45
4.1 Introduction . . . 45
4.2 Energy analysis of the pseudoelastic process . . . 47
4.3 Characterization of the shakedown state . . . 51
4.3.1 The evolution of energy in one cycle . . . 51
4.3.2 Energy analysis at the shakedown state . . . 53
4.3.3 Temperature analysis at the shakedown state . . . 55
4.4 Fatigue analysis of SMAs . . . 62
4.4.1 The stored energy at stabilized cycles in SMAs . . . 63
4.4.2 Energy-based explanation of the thermomechanical coupling in the low cycle fatigue of SMAs . . . 66
4.4.3 Stored-energy-based criterion for low cycle fatigue of SMAs . . . 67
4.5 Conclusion . . . 75

5 Low cycle fatigue crack initiation in shape memory alloys 77
5.1 Introduction . . . 77
5.2 TRIP-based modeling of fatigue crack initiation . . . 79
5.2.1 Physical mechanism of fatigue crack initiation . . . 79
5.2.2 Theoretical modeling . . . 80
5.3 Experimental validation . . . 86
5.3.1 Experiment . . . 86
5.3.2 Dependence of TRIP on temperature . . . 86
5.3.3 Maximum temperature as fatigue indicator . . . 86
5.4 Discussions . . . 94
5.4.1 Response to question 1 . . . 95
5.4.2 Response to question 2: location of the fatigue cracks initiation . . . 97
5.5 Conclusions . . . 100

6 Effect of the training stress on fatigue lifetime of SMAs 103
6.1 Introduction 103
6.2 Experimental results and discussion 104
6.3 Conclusion 108

7 Conclusion and future work 109
7.1 Conclusion 109
7.1.1 Thermomechanical coupling in low cycle fatigue behaviors 109
7.1.2 Crack initiation 110
7.1.3 Fatigue criteria 110
7.1.4 Improvement of low cycle fatigue performance 111
7.2 Future work 111

Bibliography 113

List of Figures

1.1 Temperature-induced phase transformation. 3
1.2 Martensite orientation under applied stress. 4
1.3 Schematic diagram of phase transformation between self-accommodating martensite, oriented martensite and austenite. 4
1.4 Effects of SMAs: (a) one-way shape memory effect; (b) (assisted) two-way shape memory effect; (c) pseudoelasticity. 6

2.1 DSC results. 14
2.2 Experiment setup. 14
2.3 Reproducibility for different load levels: the stress strain curve (300th cycle) and the fatigue lifetime at fixed loading rate 0.64Hz (where Nf is the number of cycles to failure) 16
2.4 Reproducibility at different load rates: the stress strain curve (300th cycle) and the fatigue lifetime at fixed loading amplitude (maximum stress is 637.0MPa). 17
2.5 Material training cycles. 18
2.6 Temperature distribution during one complete cycle: stress controlled; maximum stress is 637.0 MPa; 0.64 Hz; 300th cycle. 18
2.7 Stabilization of the thermomechanical response during the fatigue loading: (a) strain controlled: 0 - 4.61%, 0.16 Hz; (b) stress controlled: 0 - 471.3MPa, 0.16 Hz; (c) stress controlled: 0 - 471.3MPa, 1 Hz. 19
2.8 The effect of fatigue during cyclic loading: stress controlled,0 - 471.3MPa, 0.16 Hz (the heat balance state holds for each cycle). 20
2.9 Mechanical and thermal responses in the stabilized cycle (cycle 300) for different loading frequencies under strain controlled loading with maximum strain = 2.63%. 22
2.10 Mechanical and thermal responses in the stabilized cycle (cycle 300) for different loading frequencies under strain controlled loading with maximum strain = 4.61%. 23

2.11 Mechanical and thermal responses in the stabilized cycle (cycle 300) for different loading frequencies under strain controlled loading with maximum strain = 6.58%. 24
2.12 Fatigue lifetime versus loading frequency under strain controlled loading (logarithmic-logarithmic scale). 24
2.13 Mechanical and thermal responses in the stabilized cycle (cycle 300) for different loading frequencies under stress controlled loading with maximum stress = 420.4 MPa. 25
2.14 Mechanical and thermal responses in the stabilized cycle (cycle 300) for different loading frequencies under stress controlled loading with maximum stress = 471.3 MPa. 26
2.15 Mechanical and thermal responses in the stabilized cycle (cycle 300) for different loading frequencies under stress controlled loading with maximum stress = 637.0 MPa. 27
2.16 Fatigue lifetime versus loading frequency under stress controlled loading (logarithmic-logarithmic scale). 27
2.17 Evolution of mean temperature with loading frequency. 28
2.18 Evolution of temperature amplitude with loading frequency. 28
2.19 Stress-temperature diagram of SMAs. 29
2.20 Mechanical response vs. frequency: (a) maximum stress vs. frequency: strain controlled loading; (b)total strain vs. frequency: stress controlled loading. . . 29
2.21 Schematic of the initiation of cracks during stress-induced phase transformation under cyclic loading. 30
2.22 The change in stress-strain curve caused by temperature effect: (a) under strain control with 6.58% maximum strain; (b) under stress control with a maximum stress=471.3MPa. 31

3.1 Predictions of hysteresis energy-based criterion ($D_{\text{cycle}} = mN_{\text{f}}^{n}$) for different loading frequencies (logarithmic-logarithmic scale). 38
3.2 Evolution of parameters m and n in hysteresis energy-based criterion with the loading frequency: (a) lg$m$ versus f; (b) n versus f. 39
3.3 Predictions of extended hysteresis energy-based criterion including thermomechanical coupling: stress control 0-637.0 MPa; 0.16-5Hz. 39
3.4 Number of cycles to failure versus strain energy ($N_{\text{f}} - e_0$). 42

3.5 Experiment results for different load ratios at 0.64 Hz: (a) strain control: 1.32%-6.58%; (b) strain control: 2.63%-6.58%; (c) strain control: 3.95%-6.58%; (d) stress control: 127.4 MPa-637.0 MPa; (e) stress control: 191.1 MPa-637.0 MPa; (f) stress control: 254.8 MPa-637.0 MPa. 43

3.6 Comparison of experimental vs. predicted lifetime for various experiments with different load ratios: all the points lie within half and twice lifetime (dotted lines). 44

4.1 After unloading: the energy is stored (i) in dislocations (the occurrence of dislocation slip can be found in any investigations of the cyclic behavior of pseudoelastic SMAs); (ii) in residual martensites (Brinson et al., 2004; Hamilton et al., 2005; Siredey et al., 2005; Kan and Kang, 2010; Sedmák et al., 2015; Chowdhury and Sehitoglu, 2017). 50

4.2 Heat transfer in a SMA wire. To avoid the influence of grips, heat conduction through the grips is characterized by a lumped convective coefficient (Yin et al., 2014), and the average temperature evaluated in a 10 mm region at the middle part of the wire is used for analysis. 52

4.3 Mechanical behavior of a pseudoelastic SMA: (a) a hypothetical ideal SMA; (b) a real SMA. 53

4.4 Stabilization of thermal response under stress controlled loading with $\sigma_{\max} = 471.3$MPa at 1Hz (heat exchange is calculated by $\frac{4}{d}\int_0^{t_p} h\,(T(t) - T_{\mathrm{ext}})\,\mathrm{d}t$, where h is taken to be as 85W/(m^2·K)). 54

4.5 Evolutions of dissipation D_{cycle}, stored energy $E_{\mathrm{st}}^{\mathrm{cycle}}$ and total hysteresis energy $\int_0^{t_p} \boldsymbol{\sigma} : \dot{\boldsymbol{\varepsilon}}\mathrm{d}t$ under stress controlled loading with $\sigma_{\max} = 471.3$ MPa at 1Hz. . 54

4.6 The synchronized temperature evolution during one stabilized cycle: strain controlled loading; maximum strain=6.58%; 0.01 Hz. 57

4.7 Stress and temperature evolutions during one stabilized cycle under strain controlled loading with 6.58% maximum strain, the blue curve corresponds to loading and the red one corresponds to unloading. 58

4.8 Stress and temperature evolution during one stabilized cycle under stress controlled loading with 471.3MPa maximum stress, the blue curve corresponds to loading and the red one corresponds to unloading. 59

4.9 Saturated temperature amplitude ΔT versus total strain ε under stress controlled loading with maximum stress=471.3 MPa (original experimental results are given in Figure 2.14). 61

4.10 Evolution of mean temperature with loading frequency: comparisons of the calculated results against the experimental data given in Figure 2.11, 2.14, 4.7 and 4.8 (h is taken to be as 85W/(m^2·K)). 61
4.11 Evolution of temperature amplitude with loading frequency: comparisons of the calculated results against the experimental data given in Figure 2.11, 2.14, and 4.7. 62
4.12 Schematic of the impact of the accumulated stored energy on macro response of SMAs. 64
4.13 Thermal and mechanical response for cycle 300 and cycle 500 under strain control loading $\Delta\varepsilon$=4.61% at (a) 0.64 Hz, (b) 2.5 Hz and (c) 5 Hz. 65
4.14 The evolutions of $\sum_{N=300}^{N=500} E_{\mathrm{st}}$ and the N_f on the mean temperature of the material based on the results given in Figure 4.13 66
4.15 Martensite in different configurations at same temperature condition: (a) a real SMA configuration Ω, the volume fraction of residual martensite reaches z_r after N cycles; (b) a hypothetical SMA configuration Ω^*, the volume fraction of residual martensite is assumed to reach z_0; (c) the hypothetical non-damaged SMA configuration Ω^*, the volume fraction of martensite after forward phase transformation reaches z_0. 68
4.16 Stress-strain curves during forward phase transformation up to z_0: $\sigma_0 - \varepsilon_0$ corresponds to the real damaged SMA and $\sigma^* - \varepsilon^*$ corresponds to the hypothetical undamaged SMA. 70
4.17 The analysis of the stabilized strain components. 72
4.18 The fatigue test results with the stabilized stress-strain response (cycle 300). For the strain controlled tests, the specimens are first subjected to stress controlled loading for 20 cycles (maximum stress 637.0 MPa, 0.04 Hz) to accommodate large residual strains. Small residual strains still accumulate upon strain controlled cyclic loading and lead to a slight compression (within -30 MPa); the accumulated residual strain at cycle 300 is measured at zero-stress state. . . . 73
4.19 (a) Fatigue lifetime vs. generalized stored energy E_{st}/ν; (b) error analysis. . . 74
4.20 The predictions of the fatigue lifetime given in Figure 4.18 by the strain energy-based model (3.15). 74

5.1 Schematic of TRIP deformation, $\boldsymbol{\Sigma}$ and $\boldsymbol{E}$ are global stress and strain, A and M represent austenite and martensite phases. 79
5.2 Schematic of stress peak in A-M interface initiating fatigue cracks through interactions between TRIP-SBs and grain boundary (GB), or other defects inside the material. 80

5.3 Local phase transformation and TRIP (π plane, where $\boldsymbol{\sigma}^*$ is the local stress in A-M interface that triggers TRIP and reaches the maximum $\boldsymbol{\sigma}^*_{\text{max}}$ when the stabilized state is reached): (a) during first cycle, high level local stress $\boldsymbol{\sigma}^*$ created by the unmatched deformation in A-M interface activates local plasticity (b) the plastic yield surface changes as a result of plastic hardening; when stabilized state is reached, local stress $\boldsymbol{\sigma}^*$ reaches its highest value and no new plasticity is triggered. 81

5.4 A schematic of phase transformation, $\boldsymbol{E}$, $\boldsymbol{E}_{\text{p}}$ and $\boldsymbol{E}_{\text{ori}}$ are global strains, $\boldsymbol{\varepsilon}_{\text{p}}$ and $\boldsymbol{\varepsilon}_{\text{ori}}$ are local strain components for TRIP and phase transformation. 82

5.5 Multi-scale analysis of the stress peak: macroscopic $\boldsymbol{\Sigma}$, $\boldsymbol{E}$ are defined at macro-scale and mesoscopic $\boldsymbol{\sigma}_i$, $\boldsymbol{\varepsilon}_i$ are defined at mesoscopic scale. Within the martensite band front, there are a number of grains undergoing phase transformation with different A-M interfaces. The local stress peak at each grain can be evaluated by the temperature at martensite band front (T_{front}), which can be regarded as a homogeneous state variable at mesoscopic scale and is very easy to be obtained at macro-scale. 84

5.6 Energy jump in A-M interface during forward phase transformation. 84

5.7 Experimental setup 87

5.8 The experimental evidence of the dependence of TRIP on temperature : the results of quasi-static tests of SMA wires at 40°C, 52°C, 65°C respectively, where the phase transformation is completed ($z = 1$), in this case according to Eq.(5.7), $\boldsymbol{\varepsilon}^{\text{p}} = \boldsymbol{E}^{\text{p}}$. 88

5.9 Infrared photos of a NiTi wire during one complete cycle: strain control 0-4.61%, 0.3Hz, where the temperature distribution is non-uniform because phase transformation always appears as a local phenomenon, i.e., Lüders-like transformation in SMAs. The temperature of the material reaches its maximum value at the end of the forward phase transformation 89

5.10 Stress-strain, fatigue lifetime and temperature evolutions under strain controlled loading: 0-4.61%. For the sake of a relevant comparison of the phase transformation plateaus, the relative strain of the stabilized cycle is used. N_{f} is the fatigue lifetime. The maximum temperature increases with the frequency and the fatigue lifetime decreases. 89

5.11 Stress-strain, fatigue lifetimes and temperature evolutions under strain-controlled loading: 0-6.58%. 90

5.12 Evolution of the maximum temperature and fatigue lifetime with loading frequency for different strain amplitudes: (a) 0-4.61%; (b) 0-6.58%. For both cases, the maximum temperature increases with the frequency and the fatigue lifetime decreases. 90
5.13 Number of cycles to failure versus maximum temperature under strain controlled loading. Fatigue lifetime is a quasi-linear decreasing function of the maximum temperature. 91
5.14 Stress-strain, fatigue lifetime and temperature evolutions under stress controlled loading (0-637.0 MPa). In the case of such high stress level, phase transformations are completed for all frequencies; as a result, a tendency similar to the case of strain-controlled loading is observed. 91
5.15 Evolution of the maximum temperature ($T_{\max}$) and number of cycles to failure (N_{f}) with loading frequency under stress controlled loading (0-637.0 MPa); a tendency similar to the case of strain-controlled loading is observed: with increasing the frequency, maximum temperature increases and fatigue lifetime reduces. 92
5.16 Number of cycles to failure (N_{f}) versus the maximum temperature ($T_{\max}$) under high-amplitude stress controlled loading (0-637 MPa). Fatigue lifetime is a quasi-linear decreasing function of the maximum temperature. 92
5.17 Stress-strain, fatigue lives and temperature evolutions under stress controlled loading (0-471.3 MPa). Since the maximum stress is fixed, phase transformation is reduced with increasing frequency at mid-stress level; less latent heat is released, and the temperature decreases.The maximum temperature of the material does not increase monotonically with the frequency. 93
5.18 Fatigue model: (a) number of cycles to failure versus maximum temperature; (b) error analysis. 94
5.19 Different loading paths for an ideal SMA under ideal isothermal conditions. . 95
5.20 The fatigue test results of polycrystalline NiTi shape memory alloys at quasi-static isothermal condition: strain controlled loading with the amplitudes 1.5%, 1.25%, 1% and 0.75% respectively (Zheng et al., 2016b). 96
5.21 The results obtained under different mechanical loads but with the same fatigue lifetime: (1) stress controlled loading, 0-471.3 MPa, 2.5 Hz; (2) strain controlled loading, 0-4.61%, 1 Hz; (3) stress controlled loading, 0-522.3 MPa, 0.16 Hz; (4) stress controlled loading, 0-637.0 MPa, 0.16 Hz. 97
5.22 The results obtained under fixed frequency 0.16 Hz: strain controlled loading with amplitudes (1) 0-2.63%; (2) 0-4.61%; (3)0-6.58%. 98

5.23 Isotherms in mechanical load amplitude-frequency diagram: all points belonging to the isotherm present the same fatigue lifetime; only when the frequency is fixed, the macroscopic mechanical response is directly correlated with the fatigue lifetime of SMAs. 98

5.24 Schematic of the fatigue fracture position: (a)-(d) the evolution of temperature distribution along the SMA wire during forward phase transformation; (e) the corresponding global stress-strain curve. At time t_4 (end of the forward phase transformation), the temperature of the SMA reaches its maximum level; fatigue crack initiates at (indicated by arrows) (f) one of the martensite fronts or (g) the interface in which two martensite fronts merge. 99

5.25 Fatigue test results of NiTi plates, obtained from Zheng et al. (2017): (a) in-situ optical observed results; (b) corresponding nominal stress-strain curves, where the arrow in each figure indicates the initiation position of the fatigue failure crack and all results correspond to the moment the forward phase transformation ends (i.e., the maximum temperature) at the stabilized state (50 cycles): 100

6.1 $N-\varepsilon$ curves, loading ratio = 0; $0 \leftrightarrow \varepsilon_{\text{max}}$. 105

6.2 The residual stress induced by dislocation slip can assist the phase transformation, where $\boldsymbol{\Sigma}$ and $\boldsymbol{E}$ are macro stress and strain; $\boldsymbol{\sigma}$ and $\boldsymbol{\varepsilon}$ are the corresponding local responses; $\boldsymbol{\sigma}_r^{\text{A}}$ and $\boldsymbol{\sigma}_r^{\text{B}}$ are local residual internal stresses in region A and region B respectively, f^0 is the yield surface of the virgin SMA and f_{A}^1 and f_{B}^1 are yield surfaces during a subsequent cycle corresponding to region A and region B respectively. 106

6.3 Schematic of the influence of the training stress on the stress required to trigger the same fraction of phase transformation during subsequent fatigue loadings, where $\boldsymbol{\sigma}_{r,\text{I}}^{\text{B}}$ and $\boldsymbol{\sigma}_{r,\text{II}}^{\text{B}}$ are the internal stresses after training in *Case* I and *Case* II respectively (both in region B); the cyclic stress responses versus time correspond the fatigue loading 0-2.5%: *Case* I in red and *Case* II in blue. 106

6.4 Stabilization of stress-strain curves during subsequent fatigue loadings, where N_f is the corresponding fatigue lifetime. The red circle indicates the residual strain due to the buckling of the wire; if this buckling can be avoided, the fatigue lifetime is expected to decrease because the SMA wires will be further tensioned. 107

Nomenclature

List of symbols

$M_s^0, M_f^0, A_s^0, A_f^0$	Phase transformation temperatures at zero stress
$M_s^\sigma, M_f^\sigma, A_s^\sigma, A_f^\sigma$	Phase transformation temperatures at stress level of σ
σ_s, σ_f	Detwinning start stress, detwinning finish stress
N_f	Fatigue lifetime
D	Mechanical dissipation
D_{cycle}	Total mechanical dissipation during one cycle
m, n	Material parameters for the hysteresis-energy-based fatigue criterion
m_1, m_2, n_1, n_2	Material parameters for extended hysteresis-energy-based fatigue criterion
$\mathcal{D}$	Damage variable
δ	$\delta = 1 - \mathcal{D}$
A_0, A_N	Effective bearing areas of the virgin/damaged materials in cycles 0 and N
K	Elastic modulus (1D)
z	Volume fraction of martensite
σ_0	Applied stress for the damaged material
σ_N^*	Effective Stress for the damaged material in cycle N
ε_0	The strain corresponding to σ_0
ε_N^*	The effective strain corresponding to σ_N^*

e_0	Total strain energy for the real damaged material
e_N^*	The equivalent strain energy corresponding to σ_N^* and ε_N^*
α, β	Material parameters for strain-energy-based criterion
$\boldsymbol{\sigma}, \boldsymbol{\varepsilon}$	Local stress and strain tensor
$\boldsymbol{\Sigma}, \boldsymbol{E}$	Global stress and strain tensor
$\boldsymbol{\varepsilon}, \boldsymbol{\varepsilon}^{\mathrm{e}}, \boldsymbol{\varepsilon}^{\mathrm{tr}}, \boldsymbol{\varepsilon}^{\mathrm{p}}$	Total strain, elastic strain, transformation strain, plastic strain
ξ	Plastic hardening variable
λ	Heat capacity per unit volume
T	Temperature of the material
T_{ext}	External temperature
t_p	Period of the cyclic loading
f	Frequency of the cyclic loading
s	Entropy
$\boldsymbol{q}$	heat flux
h	Lumped convective coefficient
W	Helmholtz free energy density
ψ	Function of the free energy W
Q^{e}	Heating due to thermoelastic effects
Q^{p}	Heating due to thermoplastic effects
Q^{z}	Heating due to phase transformation and martensite orientation
Q^{cycle}	Heat exchange during one cycle
d	Diameter of the SMA wire
T_{mean}^*	Mean temperature
ΔT	Temperature amplitude

ΔT_{h}	Variation of temperature during elastic deformation
ΔT_l, ΔT_{un}	Variation of temperature during loading/unloading
$\mathcal{H}$	Correction factor for calculation the total heat transfer during one cycle
a, b, κ	Material parameters for calculation of temperature amplitude
$C(z,T)$	Heat density associated with the phase change
l_0	Latent heat released during forward transformation
E_{st}^{z}, E_{st}^{ξ}	Stored energy related to transformation and plastic hardening
$E_{\mathrm{st}}^{\mathrm{cycle}}$	Total stored energy during one complete cycle
E_{st}	Accumulation of stored energy
e_N	Strain energy for real material in cycle N
σ^*, ε^*	Stress and strain for the hypothetical non-damaged material
e_0^*	Strain energy corresponding to σ^* and ε^*
$\boldsymbol{\varepsilon}^r$	Residual strain
z_r	Volume fraction of residual martensite
$\boldsymbol{\gamma}$	The maximum orientation strain
γ	The equivalent value of maximum orientation strain $\boldsymbol{\gamma}$
ω, k	Material parameters for the stored-energy-based fatigue criterion
$\mathbb{D}$	Pseudo-potential dissipation
$\mathcal{A}_x$	Thermodynamic force associated to the dissipative variable $\boldsymbol{x}$
$\boldsymbol{\sigma}_{\mathrm{max}}^*$	The maximum stress peak in austenite-martensite interface
$\boldsymbol{B}$	Back stress tensor
$\boldsymbol{H}$	Kinematic hardening modulus tensor
e_{M}	Energy jump in A-M interface
μ, η	Material parameters for the maximum temperature-based fatigue criterion

σ_r	Residual stress

List of abbreviations

A	austenite
GB	grain boundaries
M	martensite
$\mathrm{M^d}$	detwinned martensite
$\mathrm{M^t}$	self-accommodating martensite
PE	pseudoelasticity
PSB	persistent slip bands
RMV	residual martensite variants
RVE	representative volume element
SMAs	shape memory alloys
SME	shape memory effect
TRIP	transformation induced plasticity
TWSME	two-way shape memory effect
UTRIRS	unit transformation induced residual strain

Chapter 1

Introduction

1.1 Introduction and motivation

Shape memory alloys (SMAs) are a typical class of smart materials which have attracted much attention in both academia and engineering industry in the last few decades. These materials are famous due to their ability to recover (undergo) large inelastic deformation when they are subjected to thermal, mechanical or thermomechanical loadings, known as the two main properties named shape memory effect (SME) and pseudoelasticity (PE). The underlying physical mechanism for these abilities is a solid-solid diffusionless transformation between austenite and martensite phases. These unique properties promote their use in a large variety of applications including aerospace industries, biomedical field, actuators and civil engineering.

In many of these applications, SMAs are subjected to cyclic loading. As a consequence, they are serious candidates for fatigue and fracture. In this respect, two kinds of fatigue are generally distinguished:

- **Functional fatigue**. Functional fatigue is the degradation of shape memory effect upon thermal or thermomechanical cycling, appearing as the decrease in the ability of recovering inelastic deformation together with the modification of transformation temperatures (Eggeler et al., 2004; Schmidt et al., 2008), and sometimes the ultimate failure (Lagoudas et al., 2009; Calhoun et al., 2015).

- **Structure fatigue**. Structure fatigue, in particular, occurs in pseudoelastic domain, in which SMAs undergo cyclic stress-induced phase transformation. The phenomena associated with structure fatigue refer to the appearance of dislocations slips, the nucleation and propagation of cracks, ultimately resulting in the failure of the structure (Wagner et al., 2004; Moumni et al., 2005; Song et al., 2017).

Low cycle fatigue of SMAs mainly deals with structure fatigue that occurs within the range of pseudoelasticity and below the plastic yield. Although low cycle fatigue of SMAs was studied very early (Tobushi et al., 1998a; McKelvey and Ritchie, 1999, 2001; Eggeler et al., 2004; Wagner et al., 2004), this issue is still challenging because fatigue lifetime of SMAs is strongly dependent on factors related to phase transformation, such as loading types, pre-training and especially thermomechanical coupling, the most typical feature in martensitic transformation; furthermore, no 3D fatigue criterion including these effects has yet been developed.

This thesis aims at filling this gap by proposing a comprehensive investigation of low cycle fatigue of SMAs. To this end, systematical experiments on low cycle fatigue of SMAs are firstly required and the physical mechanisms behind the phenomena observed should be well clarified. The fatigue criterion including all major effects of phase transformation (such as thermomechanical coupling and loading mode dependence) must be defined using macroscopic responses which can be directly measured. Finally, based on all the findings, a method of improving the low cycle fatigue performance of SMAs is expected to be developed. These purposes are achieved in this thesis following three steps:

The first step is devoted to experimental investigations. In order to understand the effects of phase transformation on low cycle fatigue of SMAs, comprehensive tensile-tensile fatigue tests under both stress and strain controlled loadings at different frequencies are carried out and discussed.

The second step deals with theoretical investigations, including fatigue lifetime prediction, energy-based interpretation of fatigue behavior and the modelling of fatigue crack initiation. To this end, a new fatigue criterion including thermomechanical coupling is developed and experimentally validated. It is shown that the total strain energy is the relevant parameter to predict the fatigue of SMAs. The conversion of hysteresis work into dissipation and stored energy in SMAs is discussed in detail and the stored energy is utilized to provide a physical interpretation of low cycle fatigue behavior of pseudoelastic SMAs. The fatigue crack initiation during cyclic stress-induced phase transformation is theoretically modeled based on transformation induced plasticity (TRIP); using the developed model, a further discussions on low cycle fatigue of SMAs is provided, including the dependence of the macroscopic mechanical loads on the fatigue lifetime and the position of fatigue failure.

In the third step, a mechanical training process that allows enhancing resistance to low cycle fatigue of SMAs is proposed in the last step.

1.2 Overview of shape memory alloys

Shape memory alloys (SMAs) are a group of metallic alloys which exhibit interesting and unique properties: they can recover their shape by simple heating after being inelastically strained (shape memory effect, SME), or accommodate large recoverable inelastic strains (pseudoelasticity, PE). This behavior is explained by the solid-solid transformation between a higher symmetry austenite phase and a lower symmetry martensite phase (Otsuka and Wayman, 1999; Lagoudas, 2008). Shape memory effect was first discovered in Au-Cd alloys in the 1930's, however, the applications of this kind of alloy did not come until 1960's, when the Nickel-Titanium (NiTi) alloys were observed having shape memory effect and pseudoelasticity (Buehler et al., 1963). Since then, SMAs have been used in a large variety of applications ranging from biomedical field to aeronautics (Jani et al., 2014).

1.2.1 Martensitic transformation

The martensitic transformation is a first-order solid-solid phase change between cubic austenite (stable at high temperature and low stress) with high crystallographic symmetry to a low symmetry martensitic phase (metastable at low temperature and high stress). The lower symmetry of the martensitic phase enables the existence of several martensitic variants defined by the orientation of the habit plane. The martensitic variants may exist in two forms: self-accommodating martensite ($\mathrm{M^t}$) in which all the variants of martensite arrange themselves in a self-accommodating manner, and oriented (detwinned) martensite ($\mathrm{M^d}$) in which a specific variant is dominant.

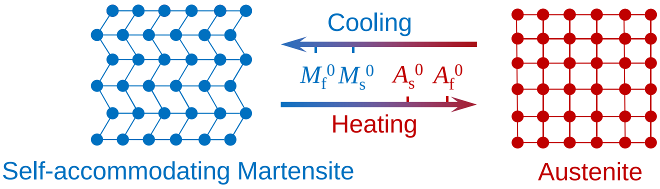
Cooling
M_f^0 M_s^0 A_s^0 A_f^0
Heating
Self-accommodating Martensite
Austenite

Figure 1.1 Temperature-induced phase transformation.

As shown in Figure 1.1, upon cooling in the absence of applied stress, austenite transforms to self-accommodating martensite, termed forward transformation. This temperature-induced phase transformation initiates at martensite start temperature M_s^0 and is completed at martensite finish temperature M_f^0. When the SMA is heated from the martensitic state, the self-accommodating martensite transforms back to austenite, and this transformation is called reverse transformation. Similarly, it is characterized by two temperatures: austenite start temperature A_s^0 and austenite finish temperature A_f^0. Since the martensitic variants are “self-accommodated”, neither forward nor reverse transformation between austenite and self-accommodating martensite can result observable macroscopic shape change.

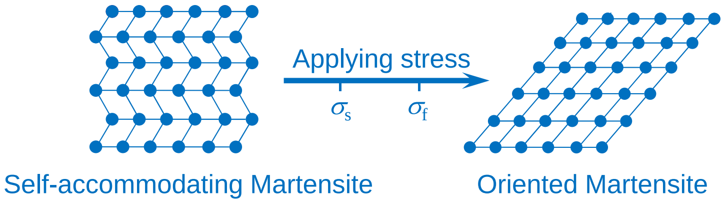
Applying stress
σ_s
σ_f
Self-accommodating Martensite
Oriented Martensite

Figure 1.2 Martensite orientation under applied stress.

If a mechanical load is applied to the self-accommodating martensite at low temperature, as shown in Figure 1.2, the martensitic variants will be reoriented (detwinned) in a certain direction depending on the applied stress, resulting in a large macroscopic inelastic strain. This inelastic strain is retained when the applied load is removed. Two critical stresses, σ_s and σ_f, represent the detwinning start stress and the detwinning finish stress, respectively.

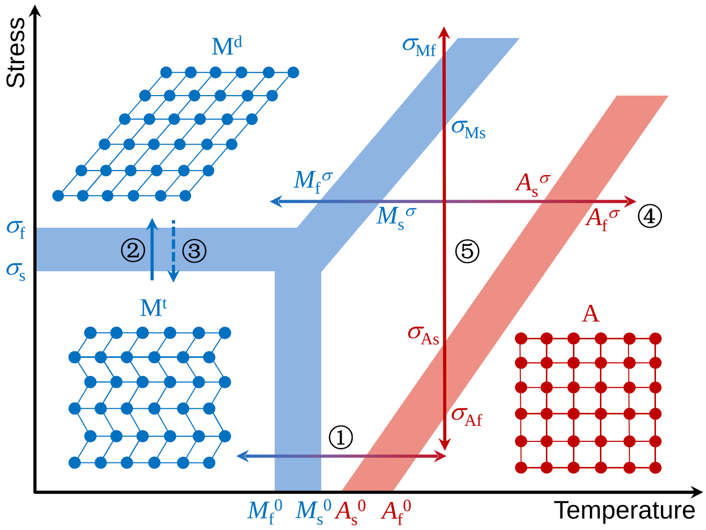
Stress
M^d
σ_{Mf}
σ_{Ms}
M_f^σ
A_s^σ
M_s^σ
A_f^σ
④
σ_f
σ_s
②
③
⑤
M^t
A
σ_{As}
σ_{Af}
①
M_f^0
M_s^0
A_s^0
A_f^0
Temperature

Figure 1.3 Schematic diagram of phase transformation between self-accommodating martensite, oriented martensite and austenite.

Figure 1.3 gives a stress-temperature diagram in which the martensitic transformation can take place in different ways. As it will be discussed below, the behavior of SMAs strongly depends on the thermomechanical loading path.

1.2.2 Shape memory effect and pseudoelasticity

This section introduces the different behaviors of SMAs depending on the loading path given in Figure 1.3, including one-way shape memory effect (OWSME), two-way shape memory effect

(TWSME) and pseudoelasticity.

One-way shape memory alloys

Shape memory effect is probably the most well-known property of SMAs. It is obtained by applying thermomechanical loading along the path 1 → 2 → 3 → 1 in the stress-temperature diagram shown in Figure 1.3: the stress-free material in austenite state is first cooled to get self-accommodating martensite without macroscopic strain (path 1, $\mathrm{A}\rightarrow\mathrm{M}^{\mathrm{t}}$). The SMA is then subjected to an applied stress and the self-accommodating martensite gets detwinned (path 2, $\mathrm{M}^{\mathrm{t}} \rightarrow \mathrm{M}^{\mathrm{d}}$), producing large inelastic strain, which remains after unloading (path 3, $\mathrm{M}^{\mathrm{d}} \rightarrow \mathrm{M}^{\mathrm{d}}$, the oriented martensite remains after removing the stress). Increasing the temperature of the material above A_{f}^{0}, the oriented martensite transforms back to austenite and the material's shape recovers to its original. The deformation curve of one-way shape memory effect is summarized in Figure 1.4a.

Two-way shape memory effect

When a SMA is cooled and heated under a constant applied stress greater than detwinning start stress σ_{s} (path 4 in Figure 1.3, $\mathrm{A} \leftrightarrow \mathrm{M}^{\mathrm{d}}$), the phase transformation between austenite A and oriented martensite M^{d} is directly induced, resulting in change and recovery of the material's shape. This is the so-called assisted two-way shape memory effect and the corresponding strain-temperature curve is given in Figure 1.4b. It should be noted that, the applied stress σ strongly affects the corresponding phase transformation temperatures, expressed as M_{s}^{σ}, M_{f}^{σ}, A_{s}^{σ} and A_{f}^{σ} respectively; all of them rise with increasing the applied stress.

Similarly, the transformation between austenite and oriented martensite ($\mathrm{A}\leftrightarrow\mathrm{M}^{\mathrm{d}}$) can be also achieved with the assistance of residual internal stress instead of applied stress. For a real SMA, dislocations are created during phase transformation and when the applied thermomechanical load is completely removed, dislocations remain and result in a residual internal stress field, which favors some martensitic variants and therefore can produce macroscopic inelastic strain. It is thus possible to transform the two shapes between low and high temperature states without any applied stress assistance. This residual internal stress can be introduced by cyclic training process.

Pseudoelasticity

Pseudoelasticity is associated with the stress-induced phase transformation between austenite and oriented martensite (path 5 in Figure 1.3, $\mathrm{A}\leftrightarrow\mathrm{M}^{\mathrm{d}}$) at temperature above A_{f}^{0}. The corresponding stress-strain curve is given in Figure 1.4c, which is featured with large reversible

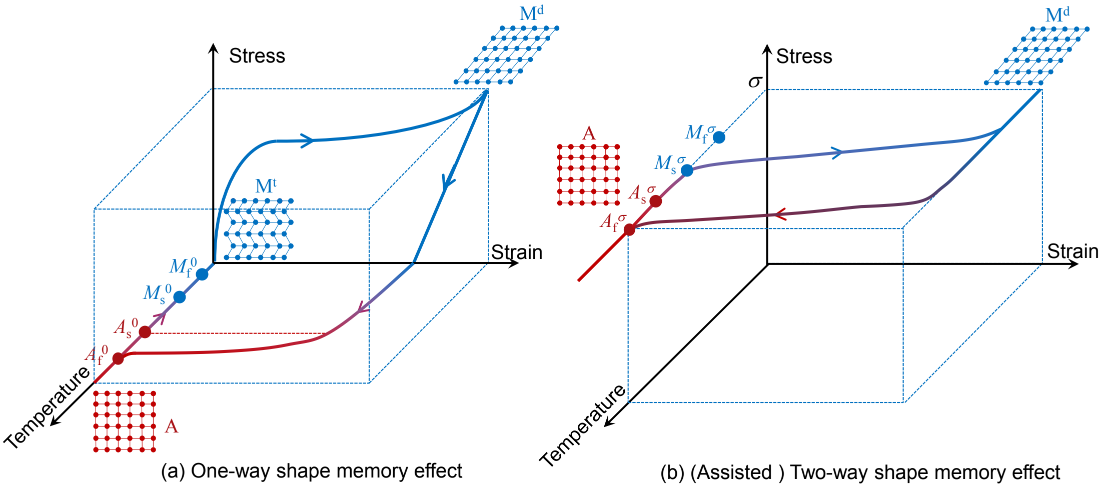
Stress
Strain
Temperature
M^d
M^t
M_f^0
M_s^0
A_s^0
A_f^0
A
Stress
σ
Strain
Temperature
M^d
A
M_f^σ
M_s^σ
A_s^σ
A_f^σ

(a) One-way shape memory effect

(b) (Assisted) Two-way shape memory effect

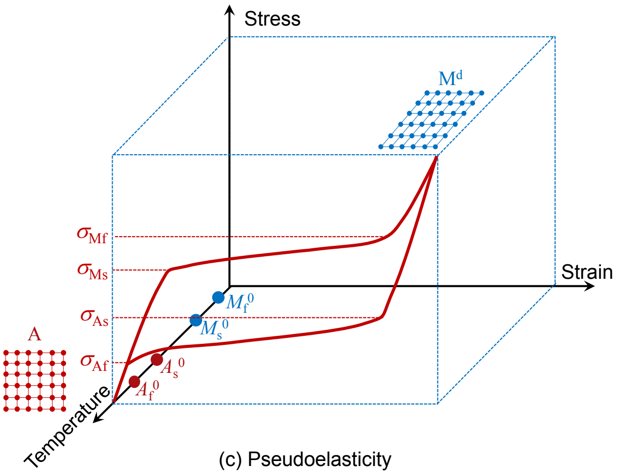
Stress
Strain
Temperature
M^d
A
σMf
σMs
σAs
σAf
M_f^0
M_s^0
A_s^0
A_f^0

(c) Pseudoelasticity

Figure 1.4 Effects of SMAs: (a) one-way shape memory effect; (b) (assisted) two-way shape memory effect; (c) pseudoelasticity.

inelastic strain and hysteresis loop. Four yield stresses can be usually identified: σ_{Ms}, σ_{Mf}, σ_{As} and σ_{Af} for martensite start stress, martensite finish stress, austenite start stress and austenite finish stress, respectively. During pseudoelastic transformation, the mechanical dissipation and the release/absorption of latent heat can result in a temperature variation which readily affects mechanical response of the material (when temperature rises, austenite becomes more stable and thus higher stress is required to drive phase transformation i.e., σ_{Ms}, σ_{Mf}, σ_{As} and σ_{Af} increase), known as temperature effect, a manifestation of thermomechanical coupling.

1.2.3 Applications of shape memory alloys

There are many kinds of SMAs, such as Fe-Mn-Si, Cu-Zn-Al and Cu-Al-Ni, among others, NiTi-based SMAs are the most important SMAs for commercial applications due to their superior thermomechanical performance. According to the above-described functional properties, the applications of SMAs can be classified into two categories: the shape memory effect is usually utilized for shape recovery and actuation (i.e., generate motion and/or force); pseudoelasticity is used in undergoing large reversible strains with high stress plateaus, and furthermore, the energy storage due to its large hysteresis. Several typical applications of SMAs in different fields are reviewed as follows:

Aerospace applications

SMAs have gathered great interest in aerospace application since 1970's. The first well-know examples is the hydraulic tube coupling used on the F-14 (Otsuka and Wayman, 1999), where the SMA sleeve is used to form a reliable connection between the two tubes are assembled. In recent years, morphing structures have attracted increasing attention in aerospace field, for which SMAs become serious candidates. Boeing designed a Variable Geometry Chevron (VGC) by using SMA actuators, and installed on a GE90-115B jet engine for the Boeing 777-300 ER commercial aircraft (Hartl et al., 2010a,b). This device has proven to be effective in reducing noise during take-off and landing. For small aircraft towards unmanned systems, morphing wing technologies are developed (Sofla et al., 2010). Another use of SMAs in morphing structure is to change the geometry of an F-15 engine inlet; through the use of SMA bundles, the generated force rotated the inlet cowl through 9° (Wax et al., 2003; Sanders et al., 2004).

Biomedical applications

Due to the biocompatibility and the advantages of recovering (undergoing) large strains, NiTi SMAs have shown their wide applicability in biomedical in the past decades, including, but not limited to, stents (Morgan, 2004), orthodontic wires and drills (Lagoudas, 2008), filters (Poletti et al., 1998), orthopedic staples (Laster et al., 2001) and so on.

Automotive applications

SMA sensors and actuators have been extensively used in modern automotive industry. SMA devices in such applications have great advantages in the scale, weight and cost of the automotive components due to their mechanical simplicity and compactness. A SMA actuation system is incorporated in the Shinkansen bullet train gearbox in which the temperature is monitored and an SMA spring actuates a value to adjust the oil level in the gearbox (Otsuka and Kakeshita, 2002). SMAs are also exploited as micro-actuators and artificial muscles in commercial robotic systems, such as jumper robots (Kheirikhah et al., 2011), walker robots (Carlo and Metin, 2006; Nishida et al., 2006), hexapod robot (Berry and Garcia, 2008), swimming robots (Tao et al., 2006; Cho et al., 2008; Wang et al., 2008), biomimetic robotic hand (Bundhoo et al., 2009), and so on.

Civil engineering

Thanks to the remarkable hysteresis during the pseudoelastic process, the SMAs' damping capacity promotes their applications for energy storage devices in wind-resistant and seismic designs (DesRoches and Delemont, 2002; Saadat et al., 2002).

1.3 Objectives and outline

In industrial applications introduced above, SMA structures are facing serious safety problems. Among others, low cycle fatigue is still an unsolved issue that limits the further applications of pseudoelastic SMAs. The objective of this thesis is to provide a comprehensive investigation of low cycle fatigue of SMAs, including following three aspects:

- the comprehensive understanding of the effects of phase transformation on low cycle fatigue of SMA;
- the development of a 3D fatigue criterion for SMAs to predict the fatigue lifetime including thermomechanical coupling;
- the development of a method that allows enhancing resistance to low cycle fatigue of SMAs.

To this aim, the thesis is organized as follows:

Chapter 2 is devoted to a comprehensive experimental investigation of the cyclic behavior and low cycle fatigue of pseudoelastic SMAs; the thermomechanical coupling is taken into account by studying the frequency dependence of cyclic thermomechanical response and the evolution of fatigue lifetime under both stress and strain controlled loadings. An infrared camera is used to measure the surface temperature of the specimen. Based on experimental observations, a theoretical explanation for the evolution of the mechanical response and fatigue lifetime with thermomechanical coupling is presented.

Chapter 3 deals with low cycle fatigue prediction in SMAs using the energy-based fatigue models. A hysteresis energy-based criterion, initially proposed by Moumni et al. (2005), is discussed and extended to take into account the thermomechanical coupling. Then a new strain energy based criterion is developed and experimentally validated. It is shown that the total strain energy is more suitable for low cycle fatigue predictions of SMAs than the hysteresis energy.

Chapter 4 presents an original energy-based analysis of the cyclic behavior and fatigue of SMAs. The conversion of hysteresis work into dissipation and stored energy in SMAs is discussed in detail. Then the stored energy is utilized to provide a physical insight into low cycle fatigue behavior of pseudoelastic SMAs. A stored-energy-based criterion is developed. The validation against experimental data show that the stored energy is the relevant parameter to predict the fatigue of SMAs.

In chapter 5, a theoretical model, based on transformation induced plasticity (TRIP), for fatigue crack initiation in shape memory alloys (SMAs) is developed. The physical mechanism of fatigue crack initiation during cyclic stress induced phase transformation is proposed and the theoretical model is established. To validate the TRIP-based model, both the experimental results of quasi-static tests and low cycle fatigue tests are utilized. The dependence of the macroscopic mechanical loads on the fatigue lifetime and the location of crack initiation (fatigue failure) are further discussed. Based on all these observations, a new criterion for low cycle fatigue of SMAs is proposed.

Chapter 6 presents a mechanical training process that allows enhancing resistance to low cycle fatigue of shape memory alloys. To this end, three training stresses were tested; for each case, NiTi wires were first subjected to the corresponding load during first 20 cycles, and then tested to failure under strain-controlled fatigue loading. Results show that specimens with higher training stresses present a better fatigue lifetime. Indeed, for sufficiently high training stress, fatigue lifetime can be 10 times extended.

Finally, conclusions of this work as well as several future directions are given in chapter 7.

Chapter 2

Experimental investigations

This chapter documents a comprehensive experimental investigation of the cyclic behavior and low cycle fatigue of pseudoelastic shape memory alloys (SMAs). To this end, strain and stress controlled tensile fatigue tests on NiTi wires are performed. The material is first trained for 20 cycles to stabilize the hysteresis loop and reach a stabilized state and then submitted to fatigue tests. An infrared camera is used to measure the surface temperature of the wire. Strain-controlled tests are performed at different total strain amplitudes, and stress-controlled ones are performed at different maximum stress values. Based on some considerations related to the thermomechanical coupling in SMAs, a theoretical explanation for the evolution of the mechanical response and fatigue lifetime with loading frequency is presented.

2.1 Introduction

The most important feature of SMAs' behavior in the pseudoelastic domain is strong thermomechanical coupling. However, most of the researches currently available for low cycle fatigue of SMAs do not account for thermomechanical coupling, even though it is a commonly accepted fact that the fatigue of SMAs is strongly affected by temperature and loading rate/frequency.

Thermomechanical coupling is generally interpreted by the thermo-elastic martensitic phase transformation: the forward phase transformation is exothermic while the reverse phase transformation is endothermic. During a stress-induced transformation, a temperature variation that is governed by release/absorption of latent heat, intrinsic dissipation and heat exchange with the surroundings occurs. Since the martensitic phase transformation is sensitive to temperature, the mechanical response is affected by the temperature variation (Tanaka et al., 1986; Shaw, 2000; Müller and Bruhns, 2006; Benafan et al., 2013; Yu et al., 2014). Consequently, one of the most important aspects of the mechanical behavior of pseudoelastic SMAs is the strong rate dependence as indicated by the experimental and analytical works reported in the literature

(Shaw and Kyriakides, 1995; Tobushi et al., 1998b; Entemeyer et al., 2000; Iadicola and Shaw, 2004; Zhu and Zhang, 2007; Grabe and Bruhns, 2008; He and Sun, 2010b, 2011; Morin et al., 2011a; Saleeb et al., 2011; Pieczyska et al., 2012; Yin et al., 2013). When a SMA is subjected to cyclic loading, its cyclic behavior reaches a stabilized state after dozens of cycles and strongly depends on the frequency of loading (Soul et al., 2010; Morin et al., 2011b; Yin et al., 2014; Yu et al., 2015b) as well as the loading mode [see the work done by Morin et al. (2011b); results under stress controlled loading are greatly different from those of Gall and Maier (2002); Soul et al. (2010) under strain controlled loading]. The local behavior (phase transformation patterns, induced local temperature and strain fields) also shows a strong frequency dependence Kan et al. (2016); Xie et al. (2016b,a).

The literature review on low cycle fatigue of SMAs can be classified below:

- Microscopic and mesoscopic scale. The creation and propagation of fatigue-cracks are investigated in grain size level; thus, microscopic observation methods such as Light Optical Microscope (LOM) (Cocco et al., 2014), Transmission Electron Microscope (TEM) (McKelvey and Ritchie, 2001; Frotscher et al., 2009; Pelton, 2011), Scanning Electron Microscope (SEM) (Eggeler et al., 2004; Predki et al., 2006; Nayan et al., 2008; Frotscher et al., 2009; Rahim et al., 2013; Koster et al., 2015) and X-ray diffraction (XRD) (Koster et al., 2015; Sedmák et al., 2015) are usually adopted. Martensitic transformation is clearly involved in the initiation of cracks, which would take place on the interfaces of martensite-austenite and the boundaries of martensitic variants (Hornbogen, 2004). The propagation of fatigue-crack was also found to be strongly affected by the stress induced micro-structural phase transformation and the grain size (Cocco et al., 2014; Yin et al., 2016).

- Macroscopic scale. These studies explain the fatigue behavior using macroscopic variables (e.g. macro stress, strain and energy, etc.). Both stress controlled and strain controlled tests were done to obtain the $S-N$ curve (Van Humbeeck, 1991; Moumni et al., 2005; Nayan et al., 2008; Koster et al., 2015) or the $\varepsilon-N$ curve (Tobushi et al., 1998a, 2000; Figueiredo et al., 2009; Runciman et al., 2011; Maletta et al., 2012, 2014), which was subsequently divided into plastic strain and phase transformation strain (Lagoudas et al., 2009). The work done by Song et al. (2015c) showed that the fatigue lifetimes of SMAs are path dependent, especially for non-proportional multiaxial loadings. To predict the fatigue lifetime, some macro fatigue criteria have been proposed in both 1-D (Maletta et al., 2012, 2014; Song et al., 2015a) and 3-D (Moumni et al., 2005; Runciman et al., 2011; Song et al., 2017).

Nearly all investigations on fatigue of SMAs that included thermomechanical coupling were based on bending-rotation tests, successfully showing that the fatigue lifetime is strongly influenced by the temperature evolution, the size of the specimen, the surroundings atmosphere (liquid or air) and the loading frequency (Tobushi et al., 2000; Eggeler et al., 2004; Matsui et al., 2004; Wagner et al., 2004). However, the exact evolution paths of stress and strain corresponding to fatigue are difficult to obtain from bending-rotation tests, which limit further explanation of fatigue lifetime evolution.

In summary: (i) from the mesoscale point of view, the interfaces and the boundaries developing as a result of martensitic phase transformation are always involved in the cracks initiation and propagation; (ii) detailed explanation of how the thermomechanical coupling influences the fatigue behavior of pseudoelastic SMAs is not clearly addressed.

The objective of the experimental study in this chapter is to understand the thermomechanical fatigue behavior of NiTi, by studying the frequency dependence of cyclic thermomechanical response and the evolution of fatigue lifetime under both stress and strain controlled loadings. This chapter is organized as following: section 2.2 describes the details of the experiments, including the material, the experimental setup and the experimental procedure. Section 2.3 gives the results of the experiments; the theoretical explanation is presented in section 2.4. Finally, summaries and conclusions are given in section 2.5.

2.2 Experiments

2.2.1 Material characterization

Pseudoelastic NiTi SMA wires with a diameter of 1 mm (50.8 at.% Ni) were obtained from Xi'an Saite Metal Materials Development Co. Ltd. The material parameters are provided by the producer and given in Table 2.1

Table 2.1 Material properties

Property	Symbol	Unit	Value
Specific heat capacity	λ_ρ	$J(KgK)^{-1}$	470
Density	ρ	Kgm^{-3}	6400
Heat capacity per unit volume	λ	$MJ(M^3K)^{-1}$	3.008

The transformation temperatures of the material are measured using a differential scanning calorimeter (DSC). The results are plotted in Figure 2.1. The phase transformation temperatures are determined as $M_s \approx$ -77 °C, $M_f \approx$ -110°C, $A_s \approx$ -31°C $A_f \approx$ -15°C.

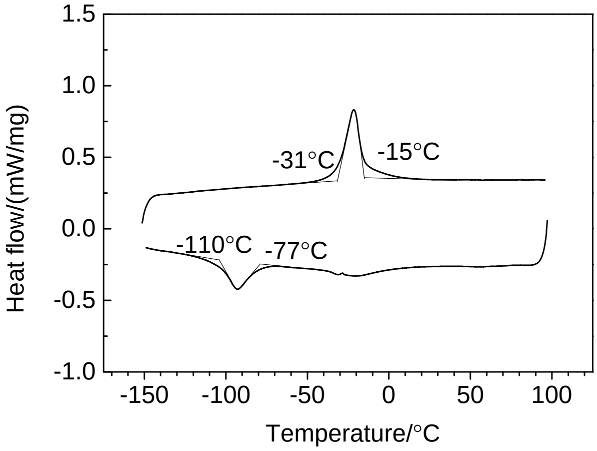

Figure 2.1 DSC results.

2.2.2 Experimental setup

The experiments were carried out using a Bose Electroforce 3510-AT fatigue test machine. As shown in Figure 2.2, two pairs of aided grips were used to hold the SMA wire in place so that the specimen does not break at the contact point under low cycle fatigue loading. The diameter of the wire is 1 mm and the gauge length of the specimen is 38 mm. Load and displacement signals were captured by Bose Wintest 7 software and processed by a PC. A Flir

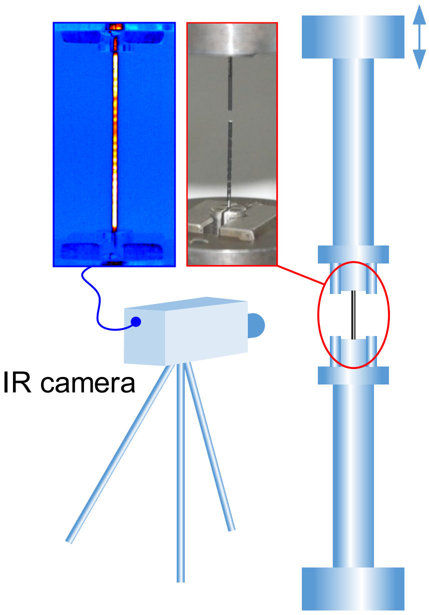

Figure 2.2 Experiment setup.

infrared camera X6540 was used to scan temperature oscillations on the surface of the wire and the calculated average in a region of 10 mm at the middle part of the wire was used for the analysis. For this purpose, all specimens were coated with a matte spray paint to maximize the emissivity.

2.2.3 Experiment procedure

Cyclic tensile fatigue tests were performed in air at room temperature (Text = 25.5 ± 0.5 °C). In order to study the effect of frequency, tests at different loading frequencies, from 0.16 Hz to 5 Hz were conducted under different loading amplitudes. Tests were conducted under both stress and strain controlled loading. Under strain control, the cycling was at a fixed strain range with maximum strains reaching 2.63%, 4.61%, 6.58% respectively. Under stress control, the maximum stresses were 420.4 MPa, 471.3 MPa and 637.0 MPa. The load ratios were fixed to zero ($\sigma_{\mathrm{min}} = 0$, $\varepsilon_{\mathrm{min}} = 0$). In order to stabilize pseudoelasticity, all specimens were first trained under stress controlled cyclic loading with a maximum force of 500N at 0.04 Hz for 20 cycles.

2.3 Experimental results

2.3.1 Repeatability of the experiments

Each test was repeated at least twice. Figure 2.3 shows that good reproducibility is obtained for different load levels: shapes and sizes of hysteresis loops, in other words, yield stresses, hysteresis areas, and maximum strains/stresses are consistent for the two tests. As shown in Figure 2.4, strong rate dependence occurs and can be also reproducible for different loading rates. The fatigue lifetime shows some deviations but is still consistent (the maximum relative deviation in Figure 2.3 and Figure 2.4 is 5.34%). Some differences occur however: the stress plateaus show slight upward movement (Figure 2.3a1, a2, b2) and the maximum strain (Figure 2.3b1, b2) and the residual strain (Figure 2.4a) shows minor deviations under stress control. In fact, considering the significant evolution of the hysteresis loop during the material training cycles (Figure 2.5), the maximum error of the residual strain occurring in Figure 2.4a is less than 10%, which is acceptable.

Overall, the thermomechanical responses are reproducible for all the loading conditions and the results can be used for the analysis of the thermomechanical behaviors of the pseudoelastic SMAs.

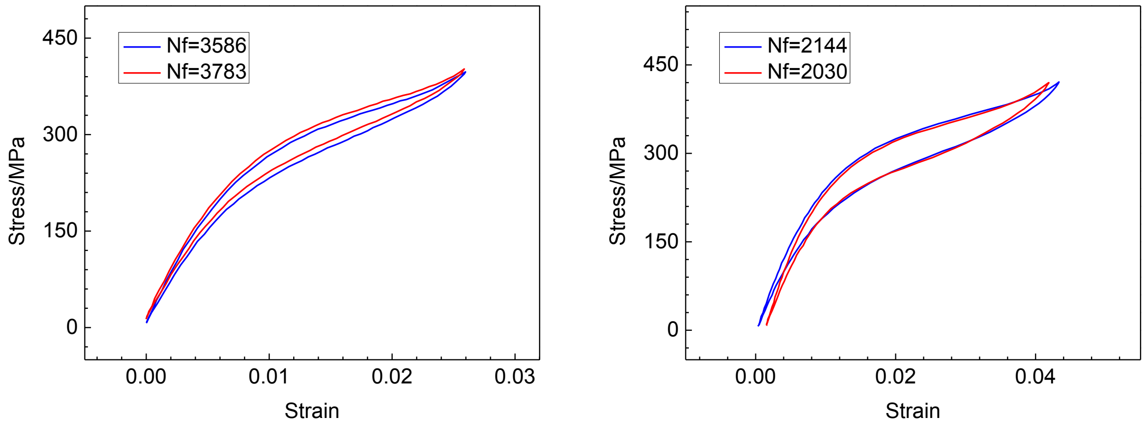

(a1) Strain control: 0-2.63%

(b1) Stress control: 0-420.4MPa

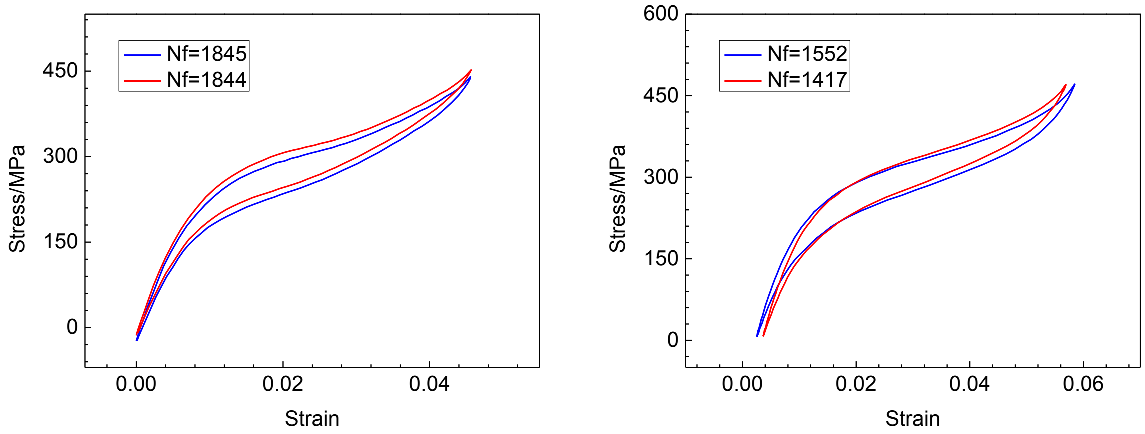

(a2) Strain control: 0-4.61%

(b2) Stress control: 0-471.3MPa

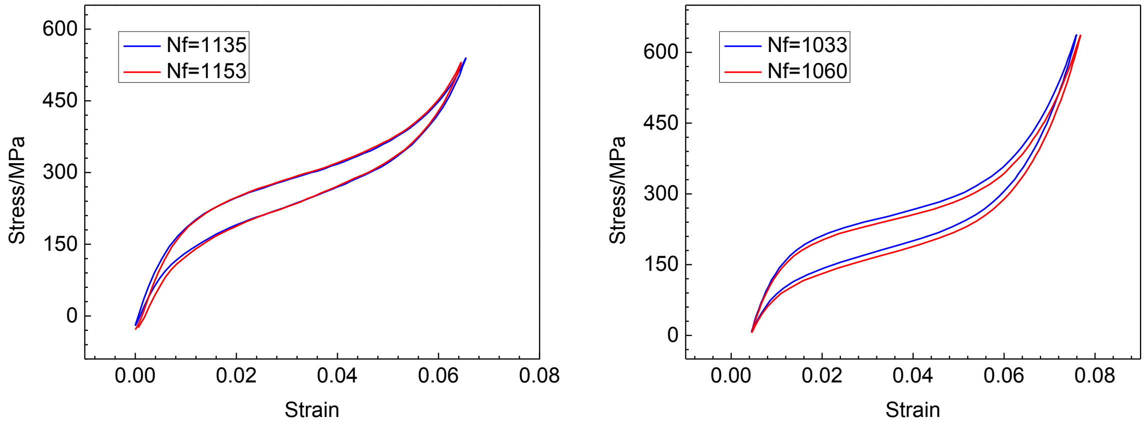

(a3) Strain control: 0-6.58%

(b3) Stress control: 0-637.0MPa

Figure 2.3 Reproducibility for different load levels: the stress strain curve (300th cycle) and the fatigue lifetime at fixed loading rate 0.64Hz (where Nf is the number of cycles to failure) .

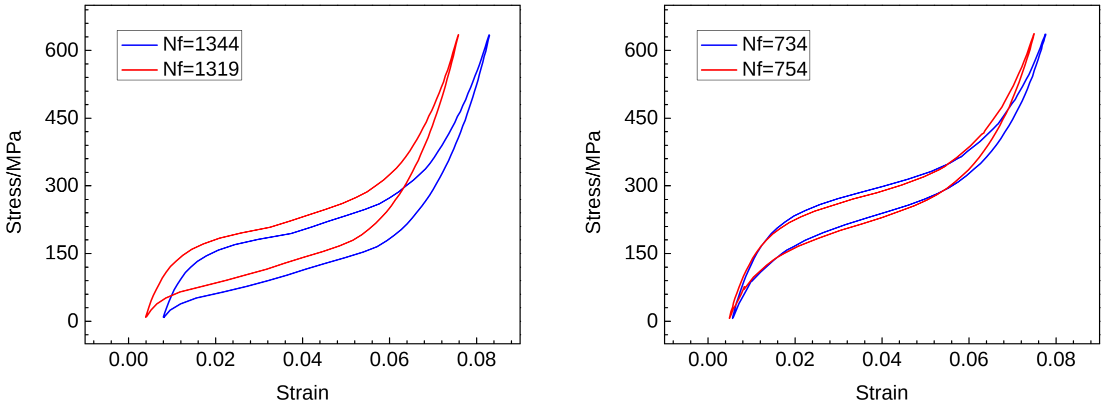

(a) 0.16Hz. (b) 1Hz.

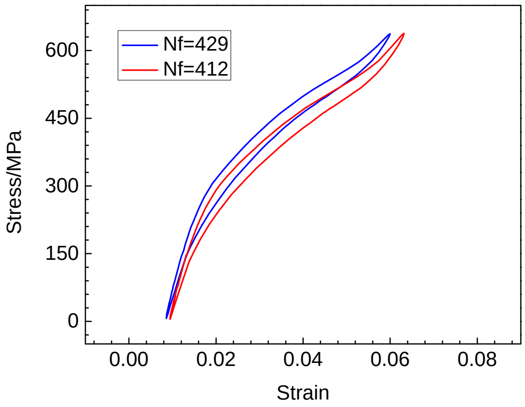

(c) 5Hz.

Figure 2.4 Reproducibility at different load rates: the stress strain curve (300th cycle) and the fatigue lifetime at fixed loading amplitude (maximum stress is 637.0MPa).

2.3.2 Stabilization of thermal and mechanical responses

Material training

In Figure 2.5, the evolution of the hysteresis loop during pseudoelastic training cycles is plotted. As a result of the accumulation of slip deformations, a residual strain occurs in each cycle and then tends to saturate. This is the so-called shakedown effect. In some papers in the literature the accumulation of the residual strain upon cycling is called ratcheting (Maletta et al., 2014; Song et al., 2015b; Yu et al., 2014). The incompatible slip deformation also induces an internal stress that can assist the formation of stress induced martensite; hence, forward phase change yield stress decreases with the number of cycles Miyazaki et al. (1986). All changes (residual strain, yield stresses, hysteresis area) of the hysteresis loop stated above tend to stabilize after a few cycles, i.e. a shakedown state is reached. These trained SMA wires with

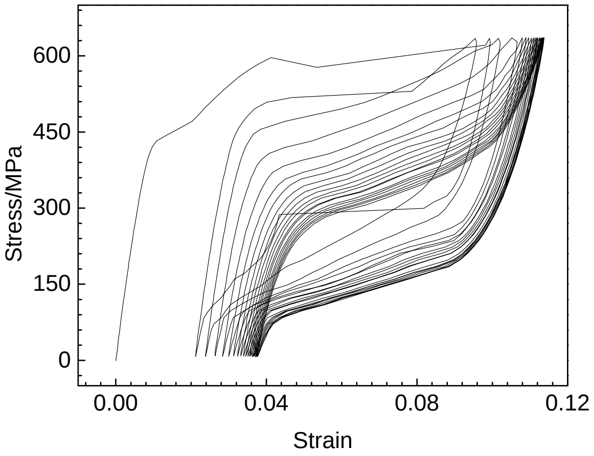

Figure 2.5 Material training cycles.

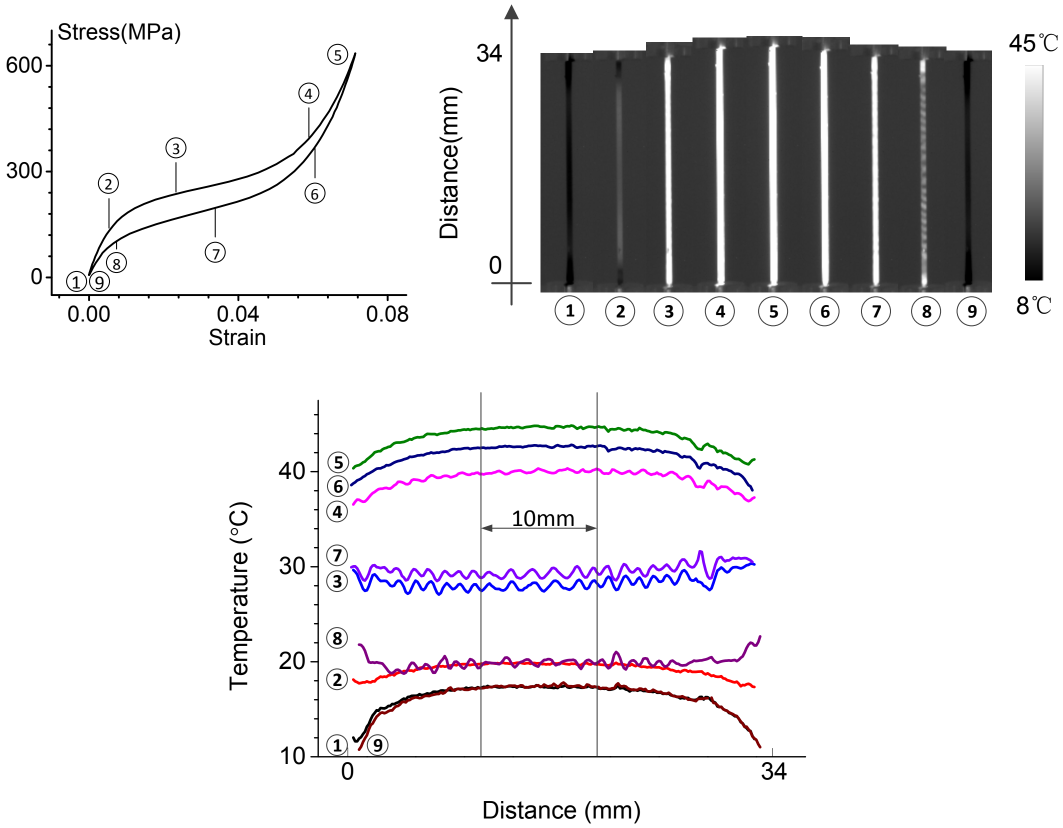

Figure 2.6 Temperature distribution during one complete cycle: stress controlled; maximum stress is 637.0 MPa; 0.64 Hz; 300th cycle.

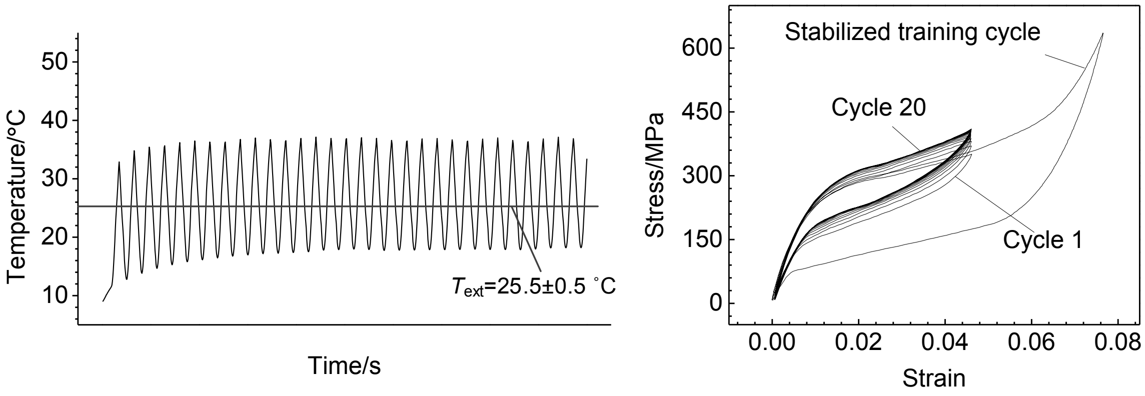

(a) Strain control: ε_{max}=4.61%, 0.16Hz

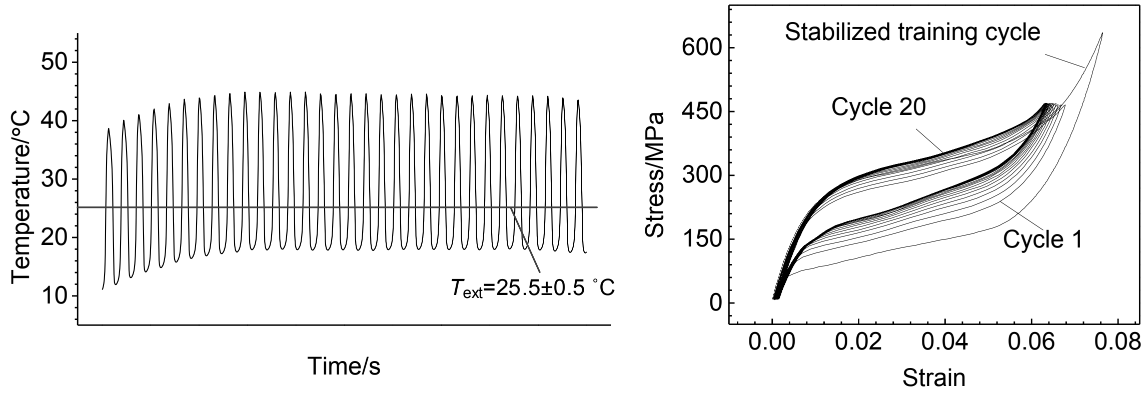

(b) Stress control: σ_{max}=471.3Mpa, 0.16Hz

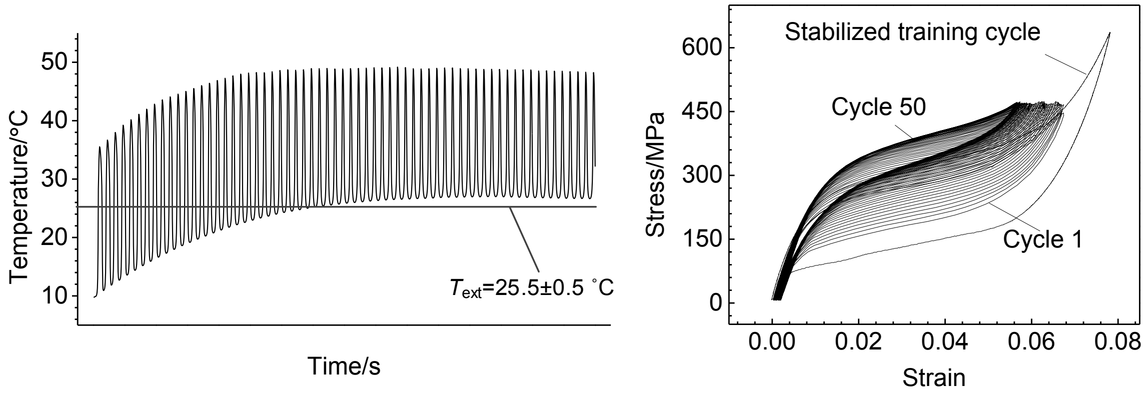

(c) Stress control: σ_{max}=471.3Mpa, 1Hz

Figure 2.7 Stabilization of the thermomechanical response during the fatigue loading: (a) strain controlled: 0 - 4.61%, 0.16 Hz; (b) stress controlled: 0 - 471.3MPa, 0.16 Hz; (c) stress controlled: 0 - 471.3MPa, 1 Hz.

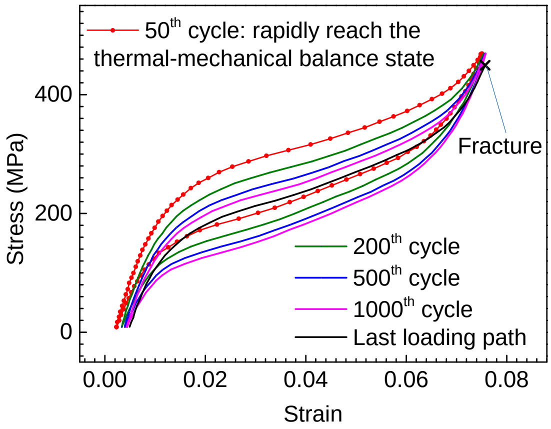

Figure 2.8 The effect of fatigue during cyclic loading: stress controlled,0 - 471.3MPa, 0.16 Hz (the heat balance state holds for each cycle).

a stable pseudoelastic behavior were used for the fatigue tests.

Evolution of the thermal and mechanical response during fatigue loading.

Figure 2.6 gives the temperature distribution of the specimen (stress controlled; maximum stress is 637.0 MPa; the frequency 0.64 Hz; 300th cycle). When the phase transformation takes place, the temperature distribution becomes non-uniform (see curve ③, ⑦ and ⑧ in Figure 2.6). As a result of heat conduction through the grips, the heat is transferred faster at the ends of the specimen; consequently, the temperature at the ends of the specimen is usually lower than at the middle part of the specimen. To avoid the effect of the ends, the average temperature is evaluated in a 10 mm region at the middle part of the wire. Besides, because the matte spray paint is not uniformly applied on the wire, there exists an error in temperature distribution (see curve ①, ⑤ and ⑨ in Figure 2.6). However, because we do not focus on the local behavior of SMAs (the phase transformation patterns), the average temperature is sufficient to analyze the thermomechanical coupling. The error caused by the matte spray paint can be calculated using the temperature distribution during the elastic deformation (curve ①, ⑤ and ⑨ in Figure 2.6) where the non-uniformity of the temperature distribution is caused only by the unevenness of the matte spray paint. In this case, the error is evaluated as the ratio of the temperature distribution perturbation during the elastic deformation and the maximum temperature amplitude. The maximum error caused by the matte spray paint is less than 3% of the total amplitude, which is acceptable.

Figure 2.7 gives the evolution of the thermal and mechanical response during the first dozen fatigue cycles (note that the temperature evolution does not start at ambient temperature, but at the minimum temperature of the last training cycle). The temperature and the mechanical response tend to stabilized rapidly and finally reach a steady-state. The mean temperature drifts up with the number of cycles until the steady-state is reached. It should be noted that, when the temperature oscillates from ambient temperature at low frequencies, the mean temperature would drift down (He and Sun, 2010b; Yin et al., 2014). Since the heat exchange with the surroundings becomes inefficient for high loading rate, more number of cycles needed to reach the steady state (see Figure 2.7 b and c, compared to 0.16Hz, more cycles are needed for 1Hz to reach the steady-state). When the steady state is reached, the dissipated energy and the heat transfer to the surroundings get balanced for one cycle and the mean temperature reaches an asymptotic value. After this stabilized state, this energy equilibrium holds for each subsequent cycle of the fatigue response. It is worthy noting that after hundreds cycles, the accumulation of the fatigue damage could impact the thermomechanical response slightly (see Figure 2.8, the 200th, 500th, 1000th cycles and the last loading curve before fracture, due to the accumulation of the fatigue damage, the stress-strain curve changes very slightly). In addition, changes caused by the fatigue damage during one cycle are negligible in comparison to the changes due to thermomechanical coupling. In this study, the minimum fatigue lifetime is 412 cycles, and for the tests under the frequency of 5 Hz, nearly 200 cycles are needed to reach a steady-state, as a consequence the 300th cycle is chosen to analyze the effect of frequency.

2.3.3 Thermal and mechanical response in the stabilized cycle

In this section, the thermal and mechanical responses as well as the evolution of fatigue lifetime under both strain control and stress control are presented.

Strain controlled tests

Three groups of the stress-strain curves under different strain amplitudes (maximum strain up to 2.63%, 4.61%, 6.58% respectively) for the stabilized cycle (cycle 300) at different loading frequencies are given in Figure 2.9 to Figure 2.11, as well as the corresponding evolution of the temperature oscillation (cycle 300 is included).

The fatigue lifetime at different loading frequencies are given in Figure 2.12. Following two aspects are observed:

- If the deformation is small, the influence of thermomechanical coupling is not obvious for low frequencies. (see Figure 2.9, the thermal and mechanical responses, as well as the fatigue lifetime for maximum strain 2.63% does not change significantly when the frequency is lower than 1Hz);

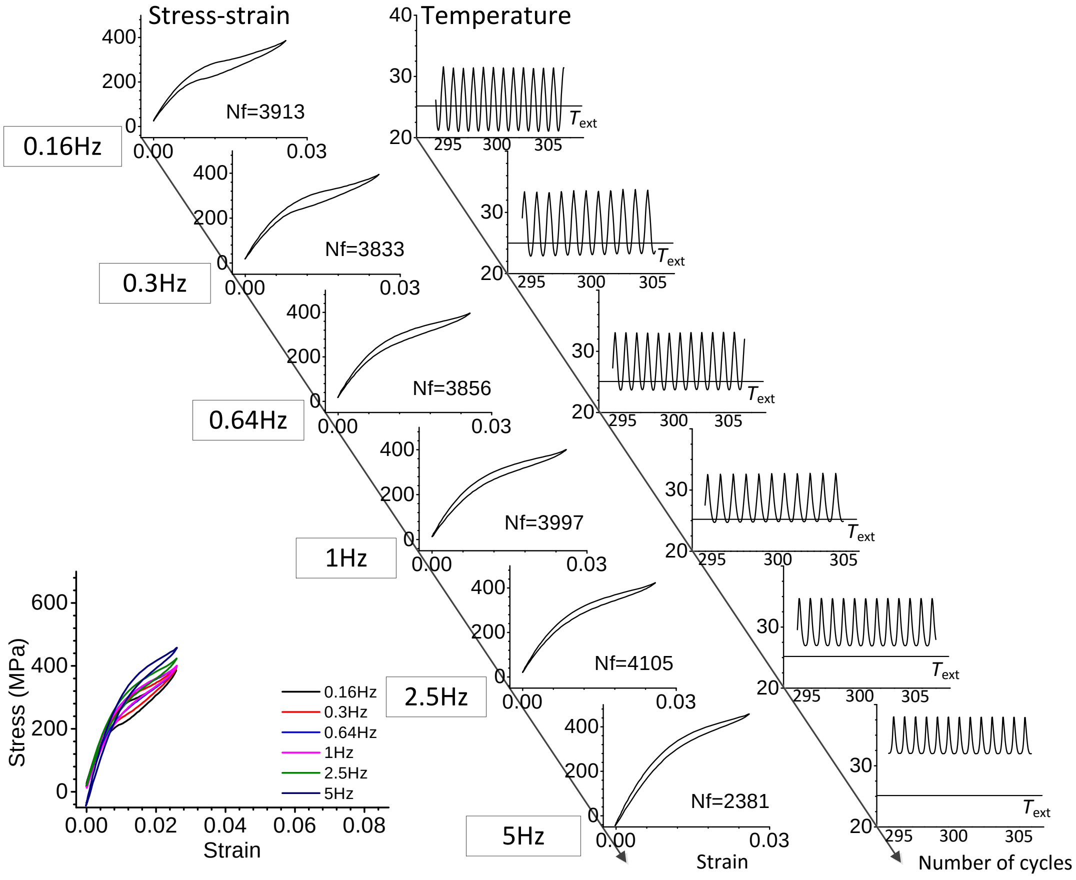

Figure 2.9 Mechanical and thermal responses in the stabilized cycle (cycle 300) for different loading frequencies under strain controlled loading with maximum strain = 2.63%.

- The fatigue lifetime shows a decreasing trend for all strain amplitudes with increasing the loading frequency.

Stress controlled tests

Similarly, the results of stress strain curves and temperature evolution under stress control are given in Figure 2.13 to Figure 2.15 (maximum stress up to 420.4MPa, 471.3MPa, 637.0MPa respectively). The results of fatigue lifetime are given in Figure 2.16 and it shows an obvious difference with the results under strain controlled loading and becomes much more complex:

- When the stress level is relatively low, first the fatigue lifetime remains constant at low loading frequency and then significantly increases with the frequency (see Figure 2.16, maximum stress = 420.4 MPa);

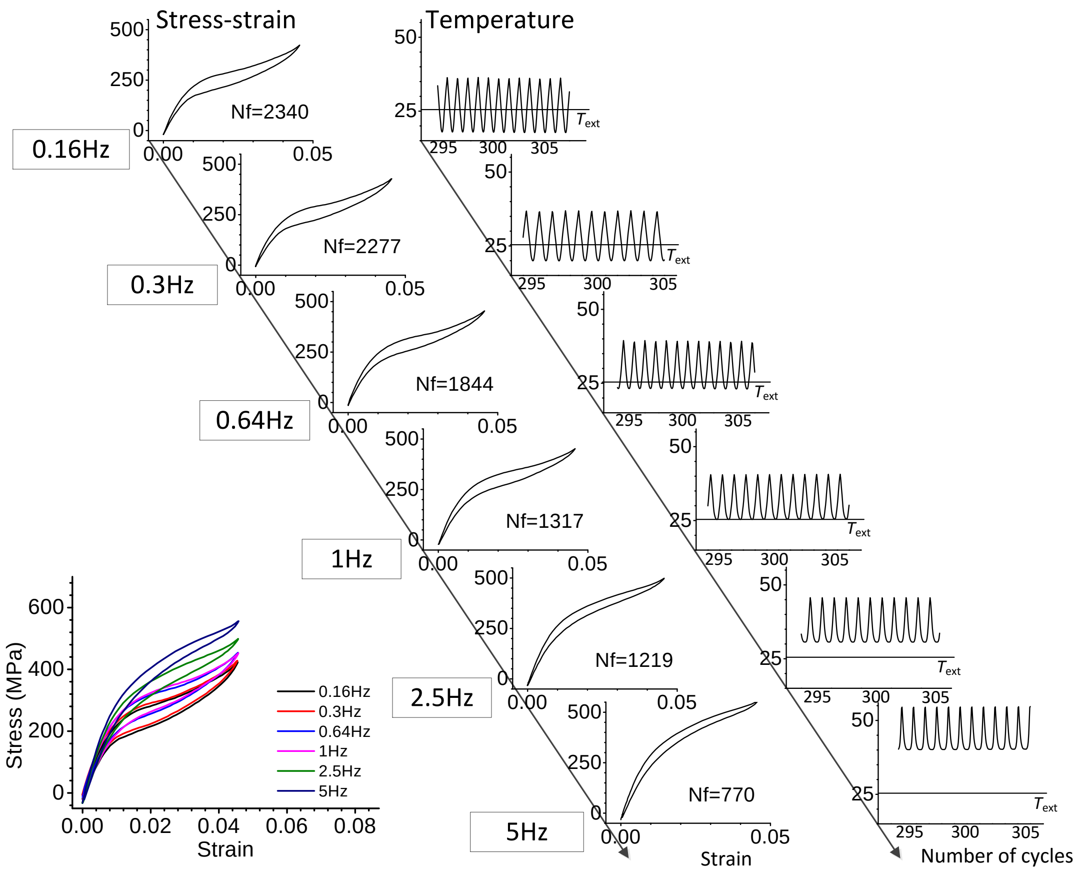

Figure 2.10 Mechanical and thermal responses in the stabilized cycle (cycle 300) for different loading frequencies under strain controlled loading with maximum strain = 4.61%.

- When increasing the stress level, there exists a critical load level for which the fatigue lifetime is insensitive to the loading frequency for all the tested frequencies (see Figure 2.16, maximum stress = 471.3 MPa);
- For high stress levels, an increase in the loading frequency results in a reduction in the fatigue lifetime (see Figure 2.16, maximum stress = 637.0 MPa).

2.4 Discussion

2.4.1 Temperature evolution

The evolution of mean temperature vs. loading frequency under both strain and stress controlled loadings are plotted in Figure 2.17a and b; mean temperature rises monotonically with the

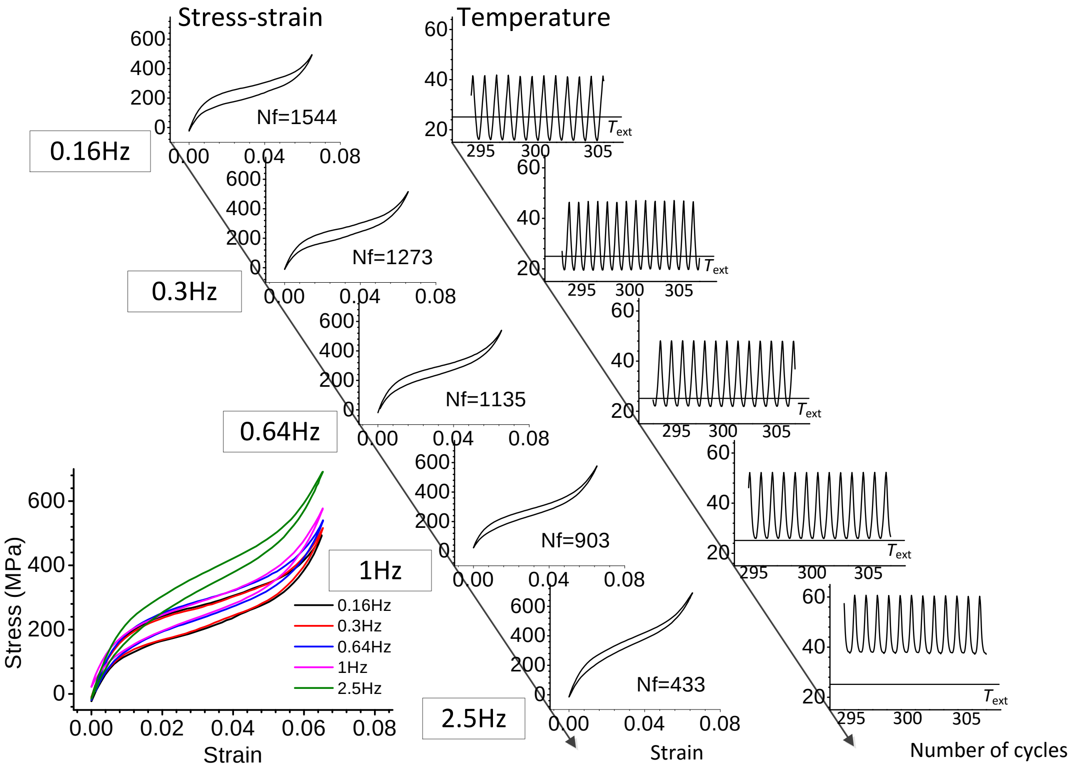

Figure 2.11 Mechanical and thermal responses in the stabilized cycle (cycle 300) for different loading frequencies under strain controlled loading with maximum strain = 6.58%.

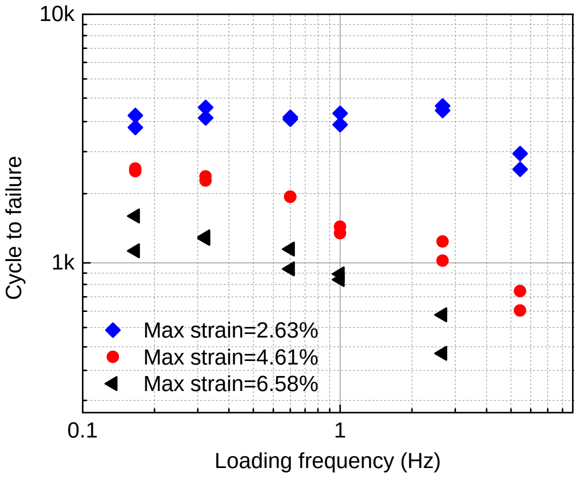

Figure 2.12 Fatigue lifetime versus loading frequency under strain controlled loading (logarithmic-logarithmic scale).

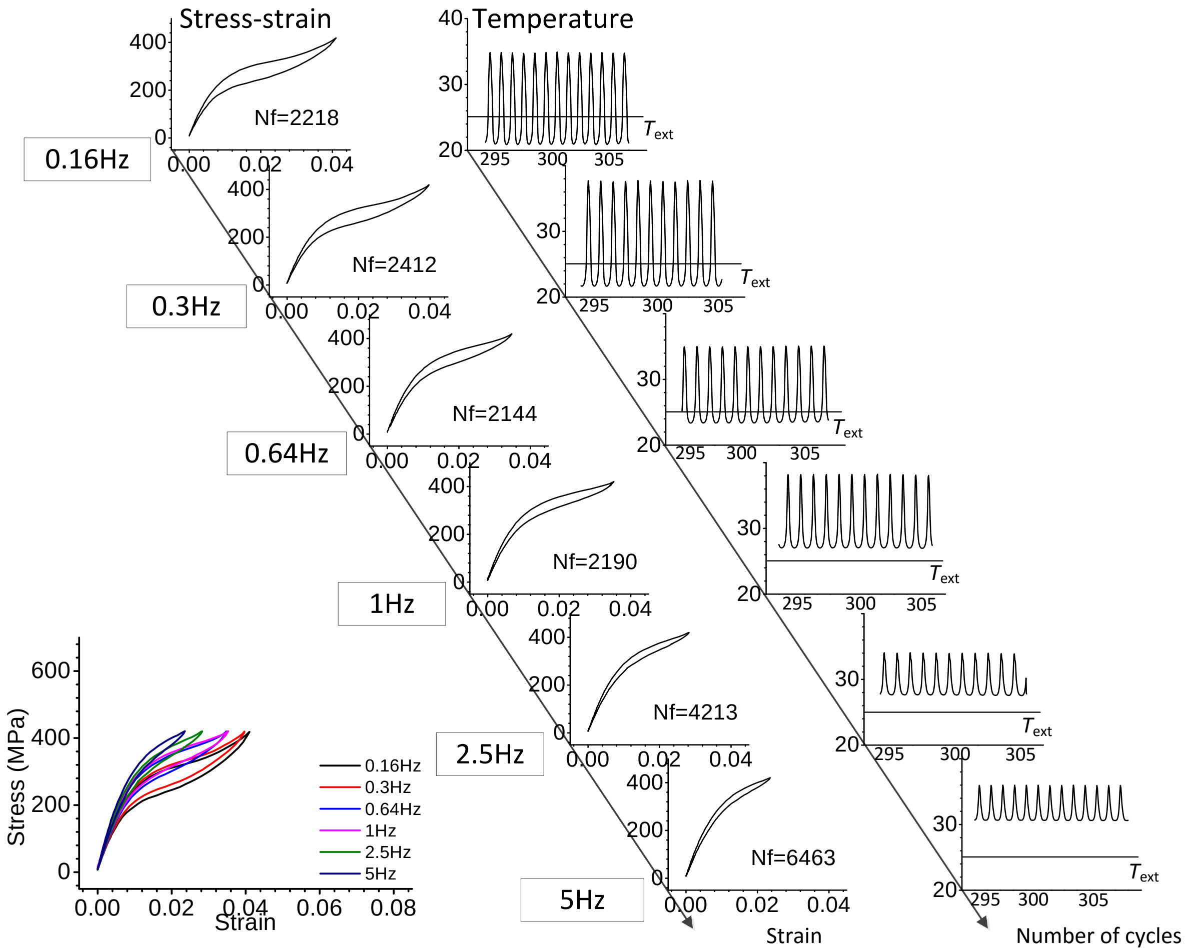

Figure 2.13 Mechanical and thermal responses in the stabilized cycle (cycle 300) for different loading frequencies under stress controlled loading with maximum stress = 420.4 MPa.

frequency. Figure 2.18 gives the evolution of temperature amplitude with loading frequency and shows that the temperature amplitude decreases. This is because higher temperatures result in a reduction in phase transformation. As shown in Figure 2.13-2.15, when compared to low loading frequencies, less phase transformations takes place at high loading frequencies in some cases, as a result of which strains decrease significantly with loading frequency (the details of the mechanism will be discussed next). A reduction in phase transformation means less latent heat release during loading (or absorption during unloading). As shown in Figure 2.9 to 2.11, the total strain is fixed; in some cases of strain controlled loading, an increase in loading frequency results in a slight increase in elastic strain (no latent heat is released or absorbed during elastic deformation). As a result, the amplitude of temperature shows a slight decrease and remains almost constant. However, for the case of stress controlled loading (Figure 2.13 to Figure 2.15), a noticeable reduction in the transformation strain occurs, and therefore results in

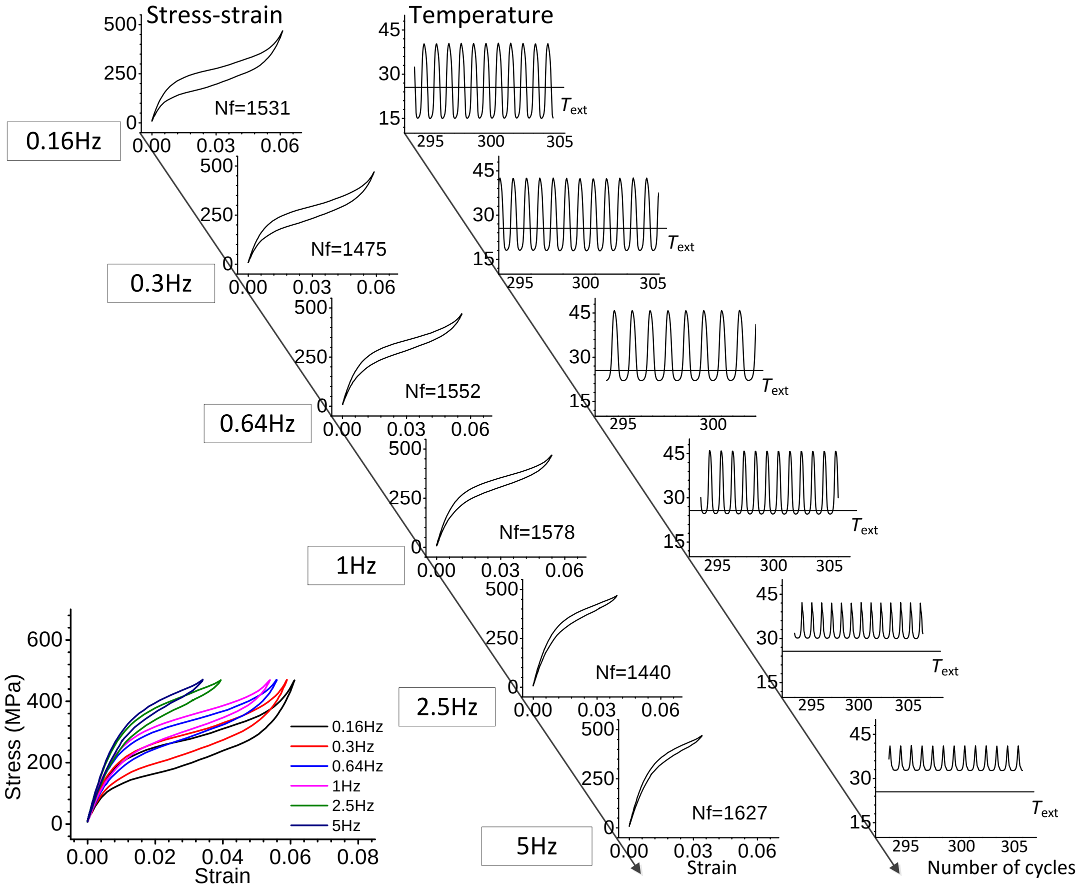

Figure 2.14 Mechanical and thermal responses in the stabilized cycle (cycle 300) for different loading frequencies under stress controlled loading with maximum stress = 471.3 MPa.

a reduction in temperature amplitude.

2.4.2 Mechanical response

A stress-temperature diagram for an SMA is given in Figure 2.19, where the effect of temperature can easily be seen. As discussed above, higher loading rates lead to higher temperature levels. As the temperature increases, stresses corresponding to martensite start and finish points increase as well, leading to a higher phase transformation plateau with a greater slope (see the loading path given in Figure 2.19). During unloading, the reverse phase transformation starts earlier for high loading frequencies, resulting in a similar behavior (see the unloading path in Figure 2.19). Consequently:

- Because the maximum deformation is fixed under strain control, stresses increase until

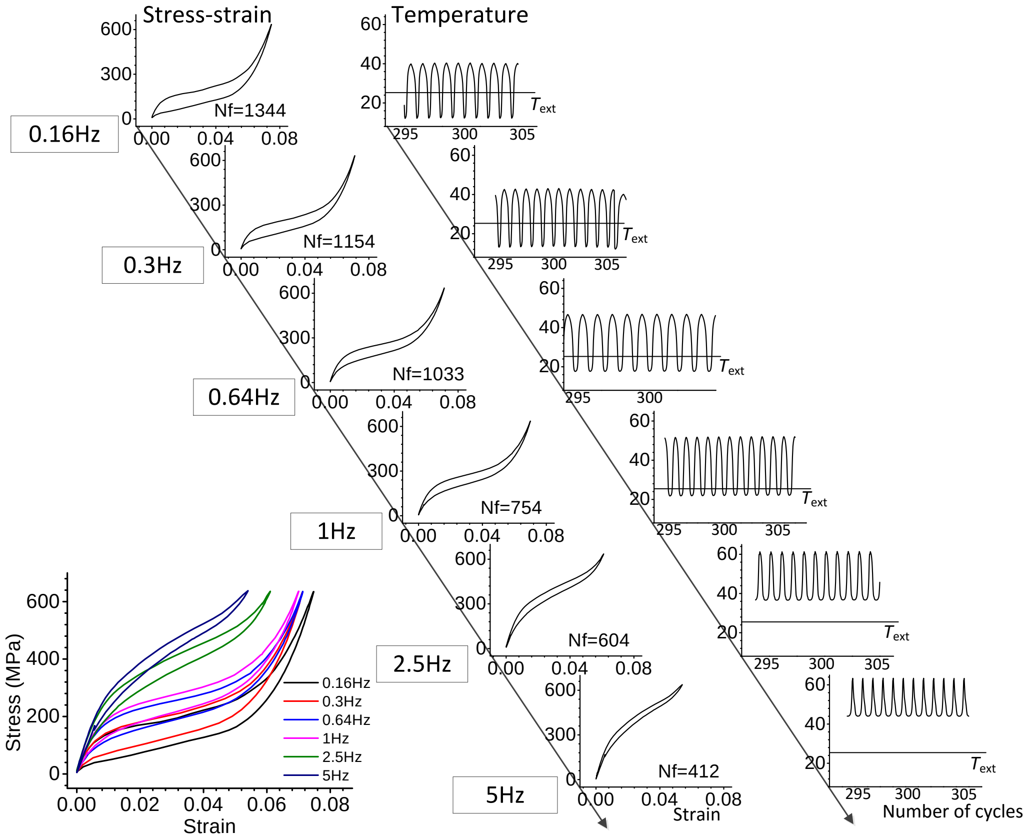

Figure 2.15 Mechanical and thermal responses in the stabilized cycle (cycle 300) for different loading frequencies under stress controlled loading with maximum stress = 637.0 MPa.

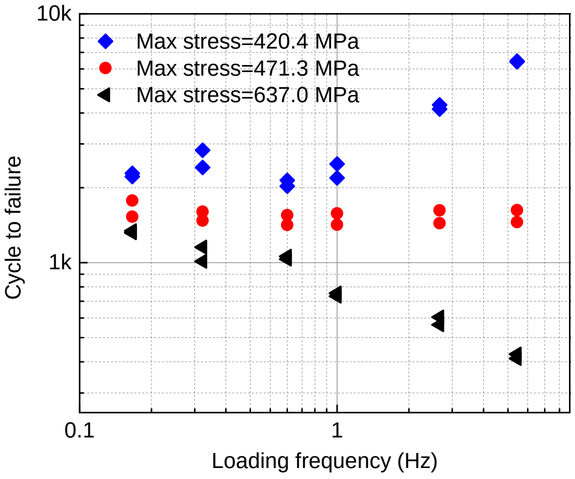

Figure 2.16 Fatigue lifetime versus loading frequency under stress controlled loading (logarithmic-logarithmic scale).

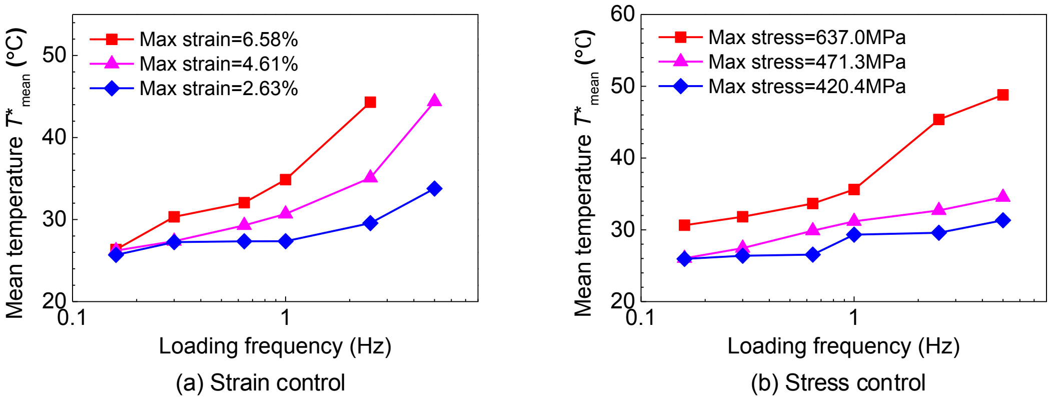

(a) Strain control (b) Stress control

Figure 2.17 Evolution of mean temperature with loading frequency.

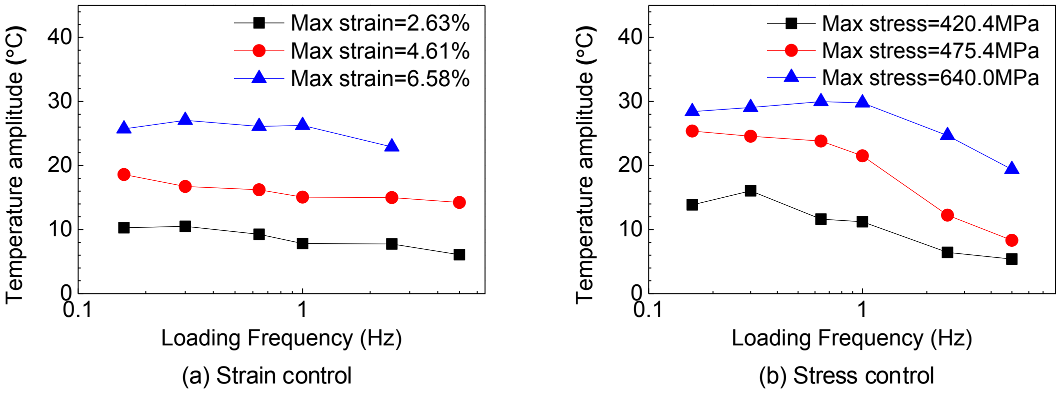

(a) Strain control (b) Stress control

Figure 2.18 Evolution of temperature amplitude with loading frequency.

the maximum deformation magnitude is reached. As shown in Figure 2.9 to Figure 2.11, and summarized in Figure 2.20a, the maximum stress significantly increases with increasing loading frequency. The increase of maximum stress for high strain level is larger than low strain level (see Figure 2.20a where the maximum stress for the case of 6.58% strain increases obviously more than the case of 2.63% strain). This is a result of higher hysteresis dissipation, where more energy is dissipated making the “temperature effect” more significant. In some cases, however, the deformation may not be large enough to complete the phase transformation. In such cases, the phase change starting stress increases and leads to a delay in phase transformation, as a result of which less phase transformation takes place (see arrow ① in the loading path under strain controlled loading in Figure 2.19). This change is not obvious since it is dominated by the elastic part.

- For stress controlled cases, the stress-strain plateau drifts up in high loading frequencies.

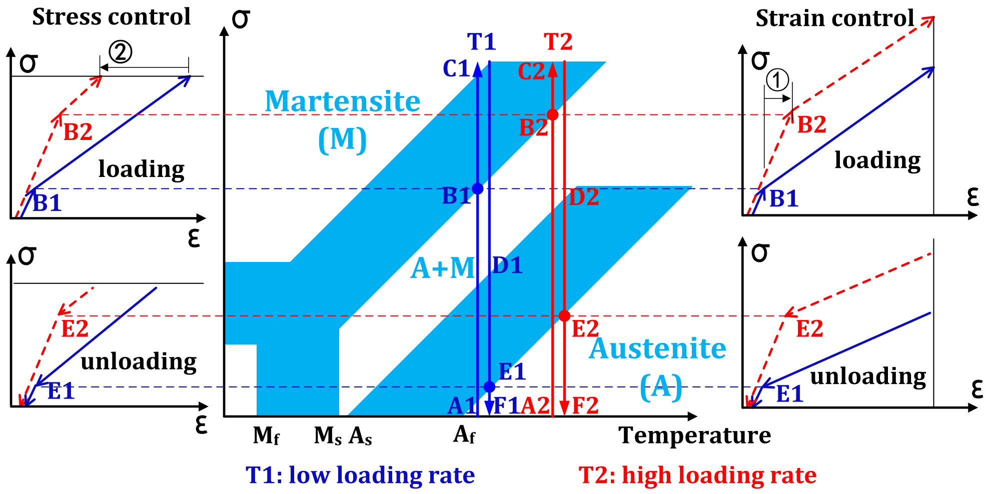
Stress control
σ
②
B2
loading
B1
ε
σ
E2
unloading
E1
ε
σ
T1
T2
C1
C2
Martensite
(M)
B2
B1
D2
A+M
D1
E2
Austenite
(A)
E1
A1
F1
A2
F2
Mf
Ms As
Af
Temperature
T1: low loading rate
T2: high loading rate
Strain control
σ
①
B2
loading
B1
ε
σ
E2
unloading
E1
ε

Figure 2.19 Stress-temperature diagram of SMAs.

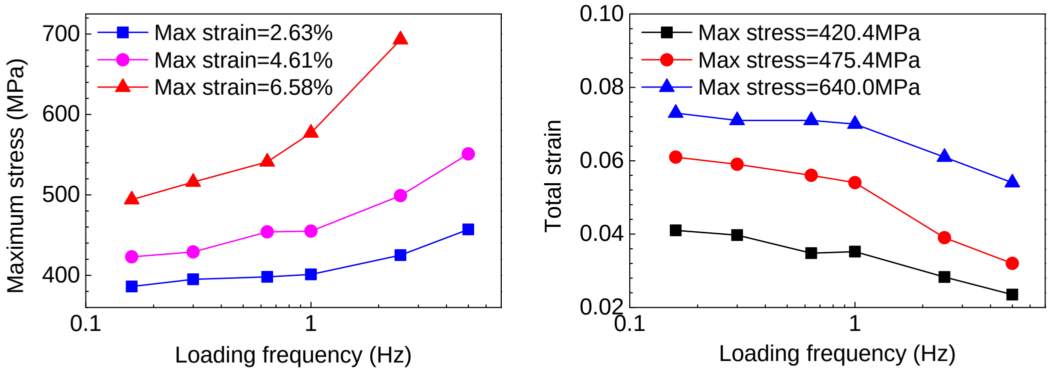

(a) Max. stress vs. frequency: strain control. (b) Total strain vs. frequency: tress control.

Figure 2.20 Mechanical response vs. frequency: (a) maximum stress vs. frequency: strain controlled loading; (b)total strain vs. frequency: stress controlled loading.

However, because the maximum stress is fixed, and if the stress is lower than the martensite finish stress $\sigma_{\rm MF}$, the increase of phase transformation plateau leads to a reduction in the amount of phase transformation (see arrow ② in the stress controlled loading path given in Figure 2.19). In some cases, the applied stress will be high enough to complete the phase transformation in low frequencies and insufficient to complete the phase transformation for high frequencies because the martensite finish stress $\sigma_{\rm MF}$ increases as the temperature rises (see the evolution of stress-strain curve with temperature given in Figure 2.14). Hence, as shown in Figure 2.13 to Figure 2.15, and summarized in Figure 2.20b, the strain decreases with increasing the loading frequency. Only in cases when the applied maximum stress is higher than the martensite finish stress $\sigma_{\rm MF}$, that the phase transformation will be completed, and the strain remains almost constant, as shown in Figure 2.15 and Figure 2.20b, for the case of maximum stress 637.0 MPa and the frequency lower than 1Hz.

2.4.3 Fatigue lifetime

The fatigue lifetime in the case of low cycle fatigue ($N_f < 10^4$) mainly depends on crack initiation. Fatigue cracks always initiate on grain boundaries (GB). For a classical ductile material under cyclic loading, some persistent slip bands (PSB) occur and interact with the GB, the results of which lead to dislocation pile-up, extrusions and stress concentration, and ultimately crack initiation (Dunne et al., 2007; Sangid et al., 2011; Anahid and Ghosh, 2013).

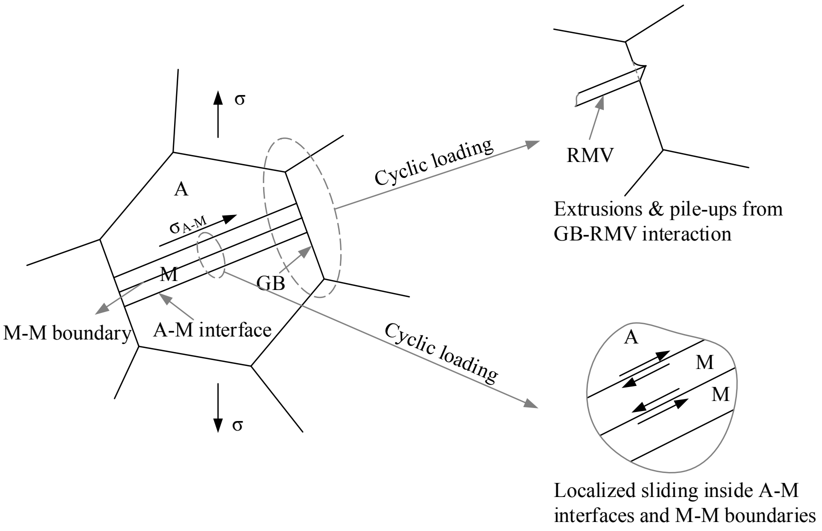
σ
A
$\sigma_{A\text{-}M}$
M
GB
M-M boundary
A-M interface
σ
Cyclic loading
Cyclic loading
RMV
Extrusions & pile-ups from GB-RMV interaction
A
M
M
Localized sliding inside A-M interfaces and M-M boundaries

Figure 2.21 Schematic of the initiation of cracks during stress-induced phase transformation under cyclic loading.

Figure 2.21 gives a schematic explanation for the initiation of cracks during stress-induced phase transformation of SMAs under cyclic loading (Hornbogen, 2004). Three types of phase interfaces exist during a typical pseudoelastic loading: austenite-austenite (A-A), austenite-martensite (A-M) and martensite-martensite (M-M). The localized sliding on A-M interfaces and on boundaries of M-M is often observed as a cause of crack formation (Hornbogen, 2004). In addition, during phase transformation, the growth of martensite variants is hindered by the GB (Benke and Mertinger, 2014); the reverse transformation from oriented martensite to austenite can be restrained by some defects, so residual martensite variants (RMV) occur (Siredey et al., 2005; Yu et al., 2014). Under cyclic loading, each cycle results in additional localized permanent deformation near the variants (Brinson et al., 2004). As a result of interaction of GB and RMV, extrusions and pile-ups occur, and finally extend to a fatigue cracks. The works proposed by (Zheng et al., 2016b, 2017) provide experimental evidence

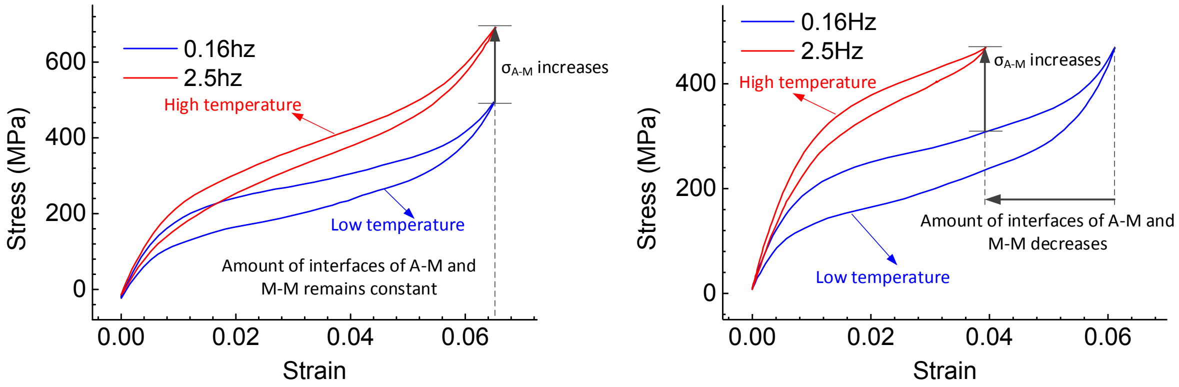

Figure 2.22 The change in stress-strain curve caused by temperature effect: (a) under strain control with 6.58% maximum strain; (b) under stress control with a maximum stress=471.3MPa.

showing that phase transformation always shorten the fatigue lifetime: (1) fatigue cracks always nucleate within the cyclic A-M zone, and not in pure austenite or pure martensite zones; (2) fatigue lifetime of M phase is shorter than A phase. This clearly confirms that the A-M interfaces and the M-M boundaries are relevant indicators for crack initiation and fatigue lifetime of SMAs. Furthermore, from an energetic point of view, the more phase transformation interfaces means more irreversible dissipated mechanisms by friction. As a consequence, A-M interfaces and M-M boundaries can be regarded as the potential crack sources. The martensite phase transformation is a temperature sensitive process; when temperature increases, the local stress associated with the A-M and M-M interfaces significantly increases and accelerates the initiation of the fatigue crack.

As a result, the evolution of fatigue lifetime of SMAs shown in Figure 2.12 and Figure 2.16 under strain and stress controlled loadings can be explained as follows:

Strain controlled loading

The maximum strain is fixed (Figure 2.22a), thus the phase transformation takes place almost to the same level in both loading frequencies (2.5Hz and 0.16Hz in Figure 2.22a); i.e. the amount of A-M and M-M interfaces that are potential crack sources changes little with the increasing of loading frequency. However, the stress associated with the A-M and M-M interfaces at high temperature is higher, hence, the crack initiation is accelerated and the fatigue lifetime decreases. When the strain amplitude is small, the temperature effect is weak to impact the mechanical response (see Figure 2.9 and Figure 2.12a, changes in stress-strain curve and fatigue lifetime only occur at very high loading frequencies).

Stress controlled loading

Stress controlled loading: The case of stress controlled loading is much more complex. As shown in Figure 2.22b, at high temperature, the plateau of phase transformation decreases, and the amount of A-M and M-M interfaces that are potential crack sources decreases. This increases fatigue lifetime. On the other hand, the stresses at A-M and M-M interfaces increase as a result of the temperature effect. The evolution of fatigue lifetime is therefore influenced by a combined effect of the reduction of the potential crack source, and the increase of the driving stress. In summary,

- For a relatively low load level (maximum stress = 420.4MPa), the phase transformation is limited and results in a little amount of A-M and M-M interfaces which continue to decrease with the frequency and tend to zero resulting in a pure austenite phase (see Figure 2.13). Consequently, the amount of A-A interfaces increases resulting in an increase in fatigue lifetime.

- For a higher load level (maximum stress = 637.0MPa), the temperature effect is much more significant, and the applied stress is high enough to complete the phase transformation. The amount of A-M and M-M interfaces remains almost constant or decreases a little (see Figure 2.15). On the other hand, a significant increase in the driving stress associated with the A-M and M-M interface dominates the evolution of fatigue lifetime; as a result, high loading rate leads to lower fatigue lifetime.

- Obviously, there exists a medium load level (here maximum stress = 471.3 MPa) for which the effect of reduction in potential crack sources and increase in driving stress on fatigue lifetime will balance each other. Therefore, one can say that in such case the fatigue lifetime under such a load level will be insensitive to the loading rate, and this is clearly seen in Figure 2.16b.

2.5 Conclusion

The thermomechanical low cycle fatigue behavior of NiTi SMAs was systematically investigated in this chapter. The mechanism of the effect of frequency on both thermomechanical behavior and fatigue lifetime is studied. The results show that the frequency dependence in SMAs is due to the temperature effect during the martensitic phase transformation. The oscillation of specimen's temperature is caused by the release/absorption of latent heat. When the amount of the heat transferred to the surroundings during loading equals the amount of the heat absorbed from the surroundings during unloading path, a steady state in temperature oscillation is reached. The amplitude of temperature oscillation is governed by the latent heat and the loading frequency. The accumulation of the hysteresis dissipation results in a monotonous increase of the mean temperature. In stabilized cycles, heat transferred out equals the hysteresis dissipation, meaning no further dissipated energy is accumulated inside the material.

Under strain controlled loading, almost equal amount of phase transformation for all the frequencies leads to an equal amount of austenite-martensite and martensite-martensite interfaces that are potential crack sources. In the other hand, an increase in temperature level makes the austenite more stable, and increases the stress associated with the A-M interfaces. Hence, the crack initiation is accelerated and the fatigue lifetime decreases.

Under stress control, the fatigue lifetime is influenced by a combined effect of reduction in the potential crack sources and an increase in the driving stress. For a relatively low stress level, fatigue lifetime is dominated by the reduction in the potential crack sources; for high stress level, the evolution of fatigue lifetime is controlled by the increase in the driving stress, and for intermediate stress level, the two effects can balance each other, as a consequence, the fatigue lifetime becomes frequency independent.

Chapter 3

Modeling of the fatigue

The experimental results obtained in chapter 2 clearly show that classical stress- or strain-based criteria are not sufficient to predict the fatigue lifetime of SMAs under non-isothermal loadings in the sense that the fatigue lifetime can be significantly changed by the frequency of cyclic loading while the stress (or strain) amplitude stays unchanged. Therefore, to take into account the effect of thermomechanical coupling, an energy-based criterion becomes a candidate. First, a traditional hysteresis-energy-based criterion (Moumni et al., 2005) is examined and extended to take into account the effect of thermomechanical coupling. Then a new strain energy based criterion is developed and experimentally validated. The comparison between new and existing models shows that the total strain energy is a reliable tool in predicting the fatigue lifetime of SMAs for different thermomechanical conditions.

3.1 Introduction

To predict the fatigue lifetime, some macro fatigue criteria have been proposed in both 1D and 3D. The 1D criteria are usually proposed through rotating-bending fatigue tests on wires, while the 3D ones are always established by using energy-based approach.

3.1.1 1D criteria

Tobushi et al. (1998a) proposed a Manson-Coffin law to model their rotating-bending fatigue results. It links the strain amplitude to the number of cycles to failure. They also showed that the value of the parameter of this criterion is different between air and water and this is explained by temperature effect on phase transformation.

Similarly, Maletta et al. (2012, 2014) proposed a modified Coffin–Manson approach for fatigue life estimation of SMAs; in this criterion, different strain mechanisms involved during repeated stress-induced martensitic transformations, the elastic and inelastic strains, are taken into account.

Song et al. (2015a) proposed a damage model, where a damage variable is defined as the ratio of accumulated dissipated energy after a prescribed number of cycles N, to that obtained at fatigue failure N_f; the fatigue criterion is established by setting the critical damage value to 1. The criterion can reasonably predict the fatigue lives of pseudoelastic SMAs in the load cases with various mean stresses, peak stresses and stress amplitudes.

Zheng et al. (2017) performed a series of experimental works on the fatigue behavior of pseudoelastic NiTi plates and their results showed that fatigue cracks initiate in the so-called active zone where SMAs undergoes locally cyclic phase transformation. The local residual strain, rather than the nominal residual strain is a good indicator on the SMAs' damage leading to the fatigue failure.

3.1.2 3D criteria

The Manson-Coffin criterion is extended by Runciman et al. (2011) where the alternating equivalent transformation strain is related to the number of cycles to failure. The improved criterion can predict the multiaxial fatigue life of SMAs and provide a satisfactory normalization for different testing modes, including torsion, tension/tension and bending.

Moumni et al. (2005) established an energy based fatigue model that predicts the fatigue lifetime using hysteresis energy at stabilized cycles. Since the SMA spends most of its lifetime at the stabilized state, this criterion links the stabilized hysteresis energy to the number of cycles to failure. Kan et al. (2012) modified it by replacing the power law equation by a logarithmic one.

Based on the new definitions of equivalent stress and non-proportionality for the non-proportional multiaxial cyclic deformation of super-elastic NiTi SMAs, Song et al. (2017) extended their previous damage fatigue model (Song et al., 2015a) to a 3D one so that it can be used for the prediction of multiaxial fatigue with various non-proportional multiaxial paths.

3.1.3 Criteria including thermomechanical coupling

The only two fatigue criteria for SMAs including thermomechanical coupling were proposed by Tobushi et al. (2000) and Matsui et al. (2004) based on Manson-Coffin criteria where the temperature and loading frequency are chosen as parameters respectively. They are both in 1D and proposed through the rotating-bending fatigue tests on SMA wires. In order to take into account all the effects observed in chapter 2, such as frequency dependence and loading mode dependence (stress or strain control), an energy-based approach should be more suitable to model the fatigue of SMAs in a unified way.

This chapter develops the energy-based criteria for low cycle fatigue of SMAs. To modeling the fatigue results obtained in chapter 2, the hysteresis energy-based criterion (Moumni et al., 2005) is first extended in section 3.2 to account for thermomechanical coupling. Then a new strain-energy-based criterion is developed and experimentally validated in section 3.3.

3.2 Hysteresis energy-based criterion

Hysteresis energy-based criterion for SMAs is developed by Moumni et al. (2005) from an energy point of view: the fatigue life evolution is driven by the hysteresis energy; lower hysteresis energy means lower energy source for the fatigue crack initiation; consequently, a longer fatigue lifetime is obtained. The criterion is defined as

$$D_{\text{cycle}} = mN_{\text{f}}^{n}, \tag{3.1}$$

where D_{cycle} is the hysteresis energy at the stabilized cycle, and m and n two material parameters. According to this criterion, the fatigue life is inversely correlated with the hysteresis irreversible energy (n is negative). However, this model is not able to explain the experimental results obtained under stress controlled loadings in chapter 2. As shown in Figures 2.13 - 2.16, with increasing the frequency, the hysteresis energy decreases (the hysteresis loop is reduced) while the fatigue lifetime evolves in different trends. This behavior is due to thermomechanical coupling which has not been taken into account.

Figure 3.1 displays the application of criterion (3.1) to the prediction of the fatigue lifetime of NiTi wires at different loading frequencies; results clearly show that criterion (3.1) works very well at a fixed loading frequency; however, when the loading frequency (heat transfer condition) is changed, the parameters of the criterion are no longer a material constants; in fact, they are affected by the thermomechanical coupling. In the case of low dissipated energy, the fatigue lifetime changes little for different loading frequencies because thermomechanical coupling is limited (there is no sufficient heat source generated inside the material). In the case of high dissipated energy, fatigue lifetime is obviously influenced by the frequency because thermomechanical coupling becomes stronger (larger heat is accumulated inside the material). In order to take into account the effect of thermomechanical coupling in criterion (3.1), m and n must be defined as a function of loading frequency. The value of criterion parameters m and n are plotted in Figure 3.2 with respect to the loading frequency; the good linear character of the curve fully supports that m and n can be expressed as functions of the frequency f and allows

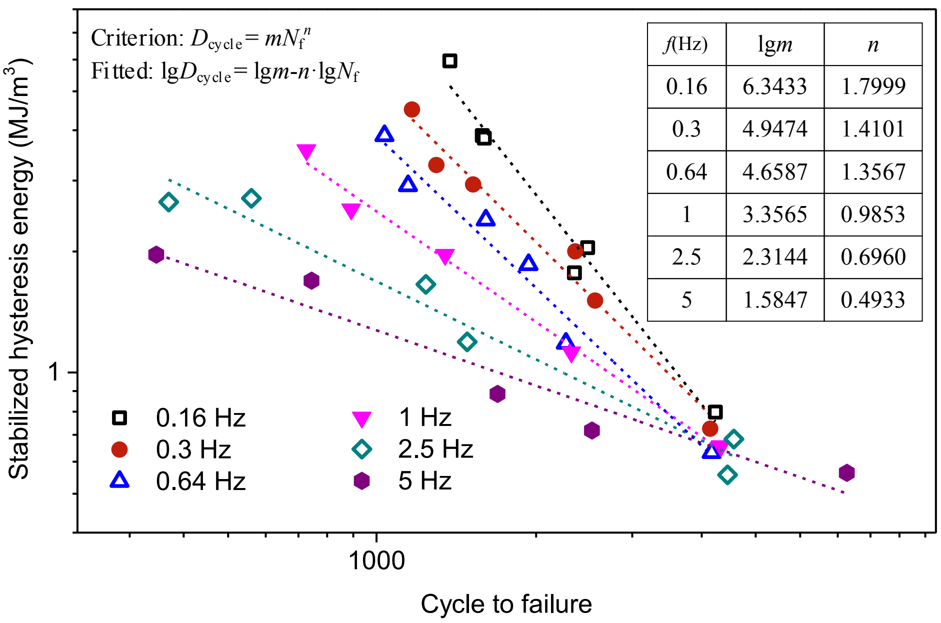

f(Hz)	lg$m$	n
0.16	6.3433	1.7999
0.3	4.9474	1.4101
0.64	4.6587	1.3567
1	3.3565	0.9853
2.5	2.3144	0.6960
5	1.5847	0.4933

Figure 3.1 Predictions of hysteresis energy-based criterion ($D_{\mathrm{cycle}} = mN_{\mathrm{f}}^{n}$) for different loading frequencies (logarithmic-logarithmic scale).

extending hysteresis-energy-based criterion (3.1) in the following form:

$$D_{\mathrm{cycle}} = m_1 f^{m_2} N_{\mathrm{f}}^{(n_1 \cdot \lg f + n_2)}, \tag{3.2}$$

where m_1, m_2, n_1 and n_2 are material parameters. For the studied material in this work, the identification of the model parameters leads to the following values: $m_1 = 3.65016$, $m_2 = -3.12729$, $n_1 = -0.86014$ and $n_2 = 1.06397$. Figure 3.3 depicts the predictions of fatigue lifetime of the stress controlled tests (0-637.0 MPa) with strong thermomechanical coupling (frequencies ranging from 0.16 Hz to 5 Hz) by using the extended criterion (3.2); the experimental results compare well with the predicted fatigue lifetime.

Criterion (3.2) illustrates that the stabilized hysteresis energy and the frequency of the cyclic loading must be used together to predict fatigue lifetime of SMAs in the case of thermomechanical coupling. However, this extended criterion is not convenient for applications: in order to identify the parameters, one must perform a great number of fatigue tests including all thermomechanical conditions (different load amplitudes and different frequencies). To overcome these drawbacks, a more relevant indicator of the fatigue of SMAs instead of hysteresis energy must be utilized. As it will be shown in next section, the total strain energy can be chosen as a unique indicator in predicting the fatigue lifetime of SMAs for all the thermomechanical conditions.

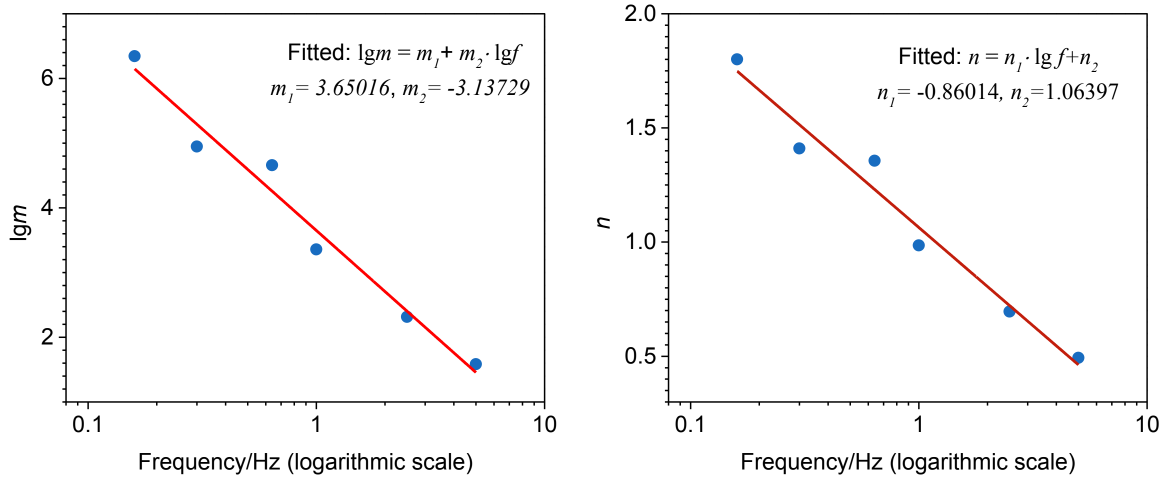

(a) lg$m$ versus f (b) n versus f

Figure 3.2 Evolution of parameters m and n in hysteresis energy-based criterion with the loading frequency: (a) lg$m$ versus f; (b) n versus f.

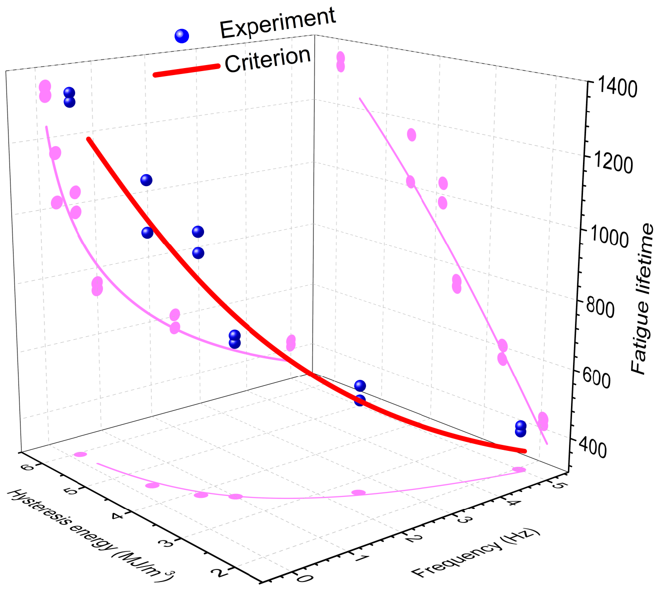

Figure 3.3 Predictions of extended hysteresis energy-based criterion including thermomechanical coupling: stress control 0-637.0 MPa; 0.16-5Hz.

3.3 Strain energy based criterion

The strain energy based criterion is proposed using continuum damage mechanics (CDM): after N cycles, localized damage in the form of micro-voids and micro-cracks initiate inside the material; a damage variable, $\mathcal{D}$, can be defined as follows:

$$\mathcal{D} = \frac{A_0 - A_N}{A_0}, \tag{3.3}$$

where A_0 and A_N are effective load bearing areas of the virgin and damaged materials in cycles 0 and N respectively. Apparently, for the virgin material, $\mathcal{D} = 0$. For the damaged material, an effective stress σ_N^* is defined as

$$\sigma_N^* = \frac{\sigma_0}{1-\delta}, \text{ with } \delta = 1 - \mathcal{D}, \tag{3.4}$$

where σ_0 is the applied stress obtained by dividing the load by the non damaged area. For SMAs, the following stress-strain relation can be used (Zaki and Moumni, 2007a; Moumni et al., 2008)

$$\sigma = K \cdot \varepsilon^{\mathrm{e}} = K \cdot (\varepsilon - z \cdot \gamma), \tag{3.5}$$

where z is volume fraction of martensite and γ is the maximum value of transformation strain, which is a material parameter. K is the equivalent elastic modulus of the SMA and can be defined as follows:

$$K_z = [(1-z)K_A^{-1} + zK_M^{-1}]^{-1} \tag{3.6}$$

where K_A and K_M are elastic moduli of austenite and martensite respectively. As stated by Simo and Ju (1987): *the strain associated with a damaged state under the applied stress is equivalent to the strain associated with its virgin state under the effective stress,*

$$\begin{aligned} \sigma_0 &= K\mid_{z^0} \cdot \varepsilon_0^{\mathrm{e}} = K\mid_{z^0} \cdot (\varepsilon_0 - z^0\gamma), \\ \sigma_N^* &= K\mid_{z^N} \cdot \varepsilon_N^{*,\mathrm{e}} = K\mid_{z^N} \cdot (\varepsilon_N^* - z^N\gamma), \end{aligned} \tag{3.7}$$

where $K\mid_{z^N}$ is the equivalent K for volume fraction z at cycle N, ε_0 is the strain that corresponds to the applied stress σ_0, and ε_N^* is the equivalent strain that corresponds to the effective stress σ_N^*. Then the equivalent strain ε_N^* at cycle N can be calculated as shown below:

$$\varepsilon_N^* = \frac{K\mid_{z^0}}{K\mid_{z^N}} \cdot \frac{\varepsilon_0 - z^0\gamma}{\delta} + z^N \cdot \gamma. \tag{3.8}$$

For a strain energy based criterion, z will be related to the strain energy e as follows:

$$\begin{aligned} z &= 0, \ e \leq e_{\mathrm{MS}}, \ \text{pure austenite;} \\ z &\in [0,1], \ e_{\mathrm{MS}} \leq e \leq e_{\mathrm{Mf}}, \ \text{phase transformation;} \\ z &= 1, \ e \geq e_{\mathrm{Mf}}, \ \text{pure martensite.} \end{aligned} \tag{3.9}$$

where e_{MS} and e_{Mf} are the strain energy corresponding to the starting and the end of martensitic phase transformation respectively. For a specified SMA, under specified thermomechanical conditions, the martensite fraction z can be represented as a function of the strain energy e:

$$z = z(e). \tag{3.10}$$

Eq. (3.8) can be rewritten as follows:

$$\varepsilon_N^* = \frac{K\mid_{z(e_0)}}{K\mid_{z(e_N^*)}} \cdot \frac{\varepsilon_0 - z(e_0)\cdot\gamma}{\delta} + z(e_N^*)\cdot\gamma. \tag{3.11}$$

where e_0 is the strain energy relative to the applied stress σ_0 and its corresponding strain ε_0 and given by $\int \sigma_0 \mathrm{d}\varepsilon_N^*$ (along the loading path); e_N^* is the total equivalent strain energy of the material at cycle N and is defined by:

$$\begin{aligned} e_N^* = \int \sigma_N^* \mathrm{d}\varepsilon_N^* &= \frac{K|_{z(e_0)}}{K|_{z(e_N^*)}}\left(\frac{1}{\delta^2}\int \sigma_0 \mathrm{d}\varepsilon_0 - \int \sigma_N^* \mathrm{d}\left(\frac{z(e_0)\cdot\gamma}{\delta}\right)\right) \\ &+ \int\left(\sigma_N^* \cdot \frac{\varepsilon_0}{\delta} - \sigma_N^* \frac{z(e_0)\cdot\gamma}{\delta}\right)\mathrm{d}\left(\frac{K|_{z(e_0)}}{K|_{z(e_N^*)}}\right) + \int \sigma_N^* \mathrm{d}[z(e_N^*)\cdot\gamma], \end{aligned} \tag{3.12}$$

where $\int\left(\sigma_N^* \cdot \frac{\varepsilon_0}{\delta} - \sigma_N^* \frac{z(e_0)\cdot\gamma}{\delta}\right)\mathrm{d}\left(\frac{K|_{z(e_0)}}{K|_{z(e_N^*)}}\right)$ represents the change of equivalent elastic energy caused by the change of equivalent elastic modulus, and can be neglected. Apparently, with the increasing number of loading cycles, damage accumulates and δ decreases gradually. As a result, the strain energy e_N^* increases with the number of cycles, until fracture occurs at cycle N_{f}. Here we redefine δ as a function of the number of cycles $\delta = \delta(N)$. At the critical cycle (N_{f}), the strain energy e_N^* reaches its critical limit value $e_N^* = e_{\mathrm{f}}$, causing the complete damage of the material. At the same time, the stress $\sigma_N^* = \sigma_0/\delta$ reaches a critical value, $\sigma_N^* = \sigma_0/\delta = \sigma_{\mathrm{f}}$, and the martensite fraction $z(e_N^*) = z_{\max}$. Consequently, Eq. (3.12) becomes:

$$e_{\mathrm{f}} - \int_0^{\substack{\text{fracture}\\\text{limit}}} \sigma_N^* \mathrm{d}[z(e_N^*)\cdot\gamma] = \frac{K\mid_{z(e_0)}}{K\mid_{z=z_{\max}}}\left(\frac{\int \sigma_0 \mathrm{d}\varepsilon_0}{\delta(N_{\mathrm{f}})^2} - \int_0^{\substack{\text{fracture}\\\text{limit}}} \sigma_N^* \mathrm{d}\left(\frac{z(e_0)\cdot\gamma}{\delta(N_{\mathrm{f}})}\right)\right) = \text{constant.} \tag{3.13}$$

The left hand $e_\mathrm{f} - \int_0^{\substack{\text{fracture}\\ \text{limit}}} \sigma_N^* \mathrm{d}[z(e_N^*) \cdot \gamma]$ represents the critical limit value of elastic strain energy when the fracture occurs; it is a material constant. Finally, Eq. (3.13) can be represented as

$$\Phi(e_0, N_\mathrm{f}) = \text{constant}. \tag{3.14}$$

Hence, the strain energy e_0 at the stabilized cycle can be used as an indicator for the fatigue crack initiation.

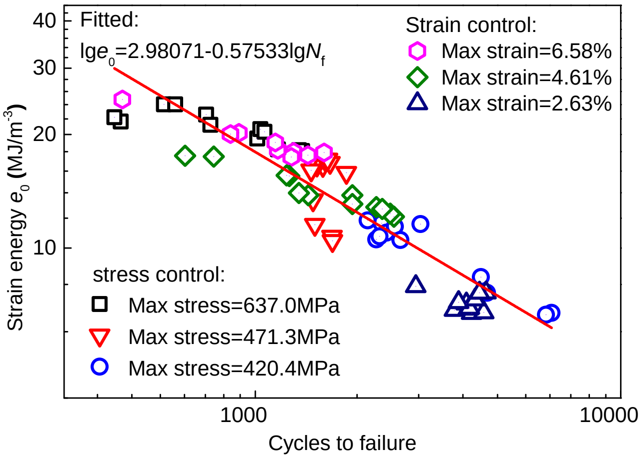

Figure 3.4 Number of cycles to failure versus strain energy ($N_\mathrm{f} - e_0$).

The value of e_0 and N_f for all tests done in this work (different load levels at different loading rates) are plotted using a logarithmic scale in Figure 3.4; the almost linear character of the curve allows to represent e_0 in the following form:

$$e_0 = \alpha N_\mathrm{f}^{\beta}, \tag{3.15}$$

where α and β are material parameters. For the material studied in this work, the model parameters have the following values: α=956.555 MJ/m^2, and β = -0.57533.

3.4 Experimental validation of the criterion

Eq. (3.15) is obtained from the experiments carried out with a fixed load ratio that is equal to zero ($\sigma_\mathrm{min} = 0$, $\varepsilon_\mathrm{min} = 0$). To validate the criterion, several groups of tests with different load ratios under both strain and stress controlled loading are performed. In Figure 3.5, mechanical responses are plotted with fatigue lifetime. As show in Figure 3.6, the experimental fatigue lifetime compares very well with the predictions of the criterion; all the points lie within half

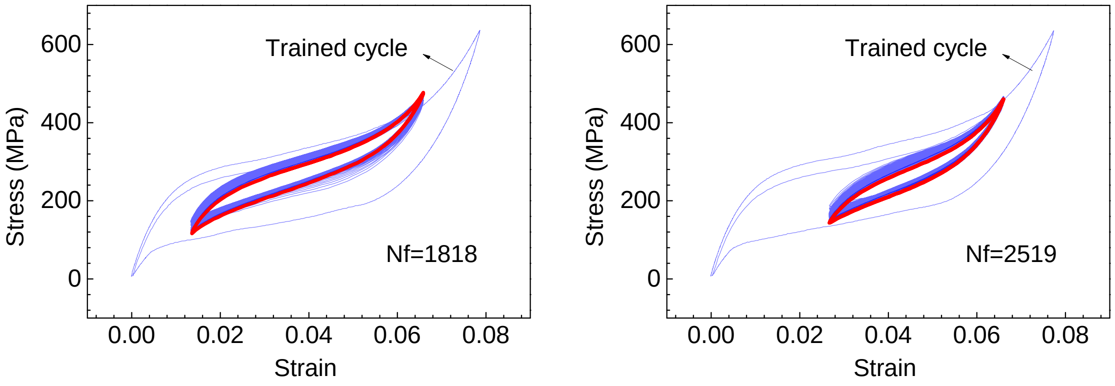

(a) Strain control: 1.32%-6.58%.

(b) Strain control: 2.63%-6.58%.

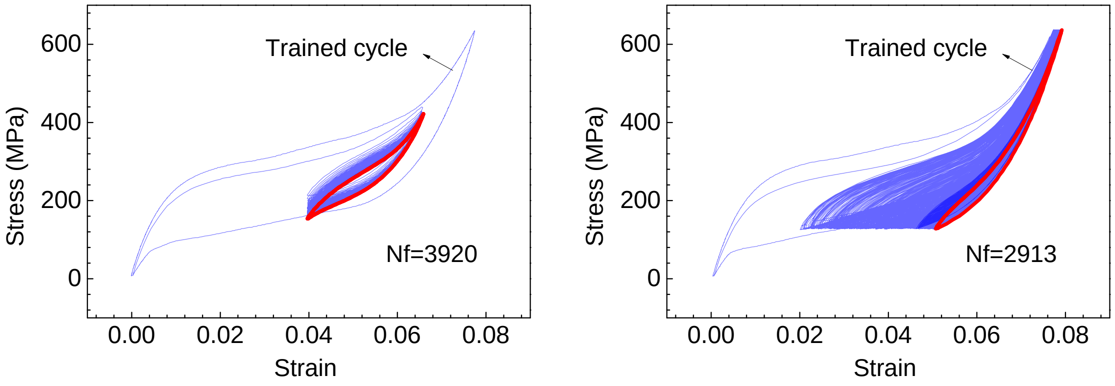

(c) Strain control: 3.95%-6.58%.

(d) Stress control: 127.4 MPa-637.0 MPa.

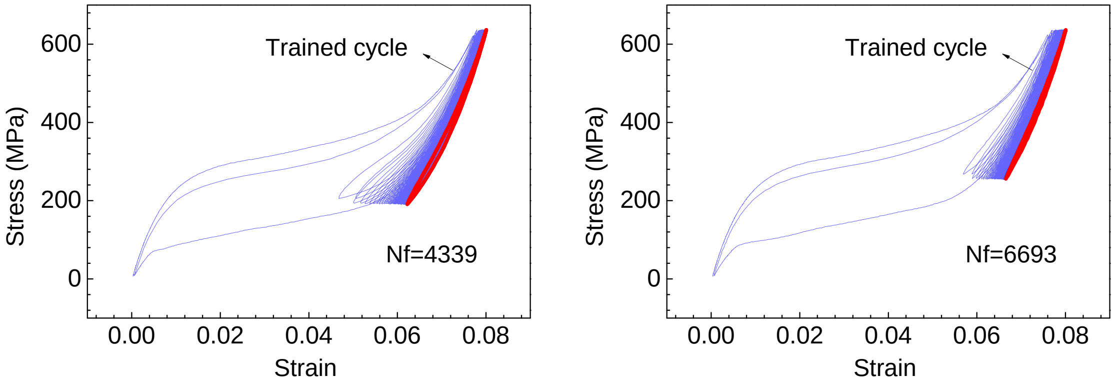

(e) Stress control: 191.1 MPa-637.0 MPa.

(f) Stress control: 254.8 MPa-637.0 MPa.

Figure 3.5 Experiment results for different load ratios at 0.64 Hz: (a) strain control: 1.32%-6.58%; (b) strain control: 2.63%-6.58%; (c) strain control: 3.95%-6.58%; (d) stress control: 127.4 MPa-637.0 MPa; (e) stress control: 191.1 MPa-637.0 MPa; (f) stress control: 254.8 MPa-637.0 MPa.

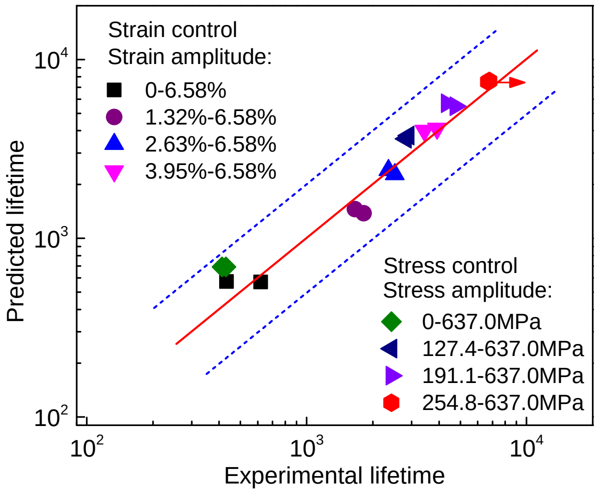

Figure 3.6 Comparison of experimental vs. predicted lifetime for various experiments with different load ratios: all the points lie within half and twice lifetime (dotted lines).

and twice lifetime (dotted lines). It must be noted that the arrows in Figure 3.6 correspond to fatigue failures occurring at the contact point of the grip. The observed fatigue lifetime could be a little longer if the stress concentration effect were avoided. The good predictivity of this criterion confirms that the use of total strain energy is a reliable tool and is convenient in predicting the fatigue lifetime of SMAs for different thermomechanical conditions (i.e. different frequencies, different loading control, (stress or strain), and different loading ratios).

3.5 Conclusion

In this chapter, energy-based approaches are adopted for the fatigue lifetime predictions. Hysteresis energy-based fatigue model is extended to take into account thermomechanical coupling. A new strain-energy-based criterion is proposed and experimentally validated. Results show that the strain energy is able to predict the fatigue lifetime of SMAs for different loads including thermomechanical coupling. In fact, the total strain energy contains the effect of temperature influenced by geometry and size of the specimen, heat exchange environment and loading frequency.

Chapter 4

Energy-based analysis of the cyclic behavior and fatigue of SMAs

This chapter aims at providing a physical insight into the cyclic behavior and low cycle fatigue of SMAs. The conversion of hysteresis work into dissipation and stored energy in SMAs is discussed in detail. The results show that during cyclic pseudoelastic process, part of the hysteresis work is dissipated into heat, and the remainder, the so-called stored energy, accumulates in dislocations and in residual martensite variants. At macro scale, during first few cycles, the stored energy is large and strongly influences the thermomechanical behavior of the SMA, it then gradually reduces and tends to zero per cycle at the shakedown state. At micro scale, however, the stored energy continues to accumulate in the micro-structure and when it reaches a critical value, fatigue cracks initiate and propagate. Finally, a stored-energy-based criterion is proposed. The validation against experimental data show that the stored energy is the relevant parameter to predict the fatigue of SMAs.

4.1 Introduction

In elastoplastic materials, the non-recoverable plastic work is partially converted into heating of the material, and the remainder, known as the stored energy, contributes to the creation and rearrangement of crystal imperfections, especially dislocations, but also point defects, stacking faults, etc., which lead to plastic hardening (Rosakis et al., 2000; Anand et al., 2015; Lubarda, 2016).

In the case of shape memory alloys (SMAs), during stress induced phase transformation, latent heat is released or absorbed; a mechanical dissipation is produced, heat is exchanged with the surroundings, the temperature field changes, and the phase transformation is affected by the temperature variation. As a result, the response of the SMA changes and the transformation region is altered. To describe the thermomechanical behavior from an energy point of view, following features must be considered:

- *Heat source: mechanical dissipation and latent heat.* During stress induced phase transformation in SMAs, a large inelastic strain occurs and can be recovered upon unloading. This process produces a large amount of mechanical dissipation and heats the material. In the literature (Moumni et al., 2005; Pieczyska et al., 2005; Soul et al., 2010; Pieczyska et al., 2012; Yin et al., 2014), the mechanical dissipation is calculated as the difference in energy between loading and unloading, in other words, the total hysteresis work (i.e. the area of the hysteresis loop) which is not correct as it will be shown later in this chapter. The forward phase transformation is exothermic while the reverse one is endothermic; the release/absorption of latent heat leads to a temperature oscillation. The temperature variation caused by mechanical dissipation and latent heat affects the mechanical response (Tokuda et al., 1999; Shaw, 2000; Sedlak et al., 2012; Benafan et al., 2013), and this is the so-called temperature effect or thermomechanical coupling.

- *Heat transfer.* The heat transfer determines whether the heat generated inside the material is sufficiently exchanged with the surroundings or not, and strongly depends on the size and geometry of the specimen, the surroundings (liquid or air) and the loading rate. Consequently, the mechanical behavior of SMAs is rate-dependent as indicated in many works reported in the literature (Shaw and Kyriakides, 1995; Entemeyer et al., 2000; Grabe and Bruhns, 2008; Morin et al., 2011a; He and Sun, 2011; Pieczyska et al., 2012; Yin et al., 2013; Yu et al., 2015b; Chatziathanasiou et al., 2016; Kan et al., 2016; Xie et al., 2016b). When a SMA is subjected to a cyclic loading, the frequency dependence (thermomechanical coupling) alters the cyclic thermomechanical behavior (Piedboeuf et al., 1998; Gandhi and Wolons, 1999; He and Sun, 2010b; Soul et al., 2010; Morin et al., 2011b; Wang et al., 2017), as well as the fatigue lifetime (Tobushi et al., 2000; Eggeler et al., 2004; Matsui et al., 2004; Wagner et al., 2004; Zhang et al., 2016).

- *Stored energy.* The so-called stored energy represents the storage of internal energy related to change in micro-structure of the material, such as the formation of crystal imperfections, point defects and stacking faults. One of the typical form of stored energy in classical elastoplastic material is the energy related to plastic hardening (especially due to the formation of dislocations), which has been widely and early investigated (Chrysochoos et al., 1989; Kamlah and Haupt, 1997; Hodowany et al., 2000; Rosakis et al., 2000; Mróz and Oliferuk, 2002; Benzerga et al., 2005; Rusinek and Klepaczko, 2009). Since the stored energy is related to the change in micro-structure of the material such as defects, it is always used as an indicator for fatigue in elastoplastic materials (Warren and Wei, 2010; Wan et al., 2014).

In the case of SMAs, however, the stored energy is not yet widely considered in the analysis of fatigue behavior, and this gap will be filled in this chapter. To this end, a comprehensive analysis of partitioning of total hysteresis work into dissipation and stored energy is provided. An energy analysis of SMAs' cyclic thermomechanical behavior during the whole process (the evolution during initial cycles and the shakedown state) and final fatigue failure is proposed with experimental validations. Section 4.2 presents some preliminary energetic issues using the first and the second laws of thermodynamics together with the Helmholtz free energy. The stored energy is defined and the relationship between the stored energy, dissipation and the total hysteresis work is given. Section 4.3 gives a formulation of the energy balance for the cyclic behavior of SMAs as well as the evolution of the dissipation and the stored energy toward the shakedown state. In section 4.4, a discussion of the stored energy at shakedown state is presented, and a stored-energy-based fatigue criterion is proposed and discussed. The results are summarized in section 4.5.

4.2 Energy analysis of the pseudoelastic process

For a SMA body, let Ω be the volume, and $\partial\Omega$ its boundary surface. The thermomechanical pseudoelastic process undergone by Ω can be described using the following variables:

- State variables: $\boldsymbol{\varepsilon}$ the total stain; and T the temperature.
- Internal variables: $\boldsymbol{\varepsilon}^{\mathrm{ori}}$ the transformation stain; z the volume fraction of martensite; $\boldsymbol{\varepsilon}^{\mathrm{p}}$ the plastic strain; and ξ the plastic hardening variable.

The total strain $\boldsymbol{\varepsilon}$ is:

$$\boldsymbol{\varepsilon} = \boldsymbol{\varepsilon}^{\mathrm{e}} + \boldsymbol{\varepsilon}^{\mathrm{ori}} + \boldsymbol{\varepsilon}^{\mathrm{p}}. \tag{4.1}$$

Based on the first and second laws of thermodynamics, for the solid given above the local heat balance equation can be written as follows:

$$T\dot{s} = D - \mathrm{div}\boldsymbol{q} + r, \tag{4.2}$$

with D the mechanical dissipation:

$$D = \boldsymbol{\sigma} : \dot{\boldsymbol{\varepsilon}} - \dot{W} - s\dot{T} \geq 0, \tag{4.3}$$

where s is the entropy, $\boldsymbol{q}$ is the heat flux , r is the heat generation (all per unit volume), and W is Helmholtz free energy density defined as follows:

$$\begin{aligned} W &= \psi\left(\boldsymbol{\varepsilon}^{\mathrm{e}}, z, \xi, T\right) \\ &= \psi\left(\boldsymbol{\varepsilon}-\boldsymbol{\varepsilon}^{\mathrm{ori}}-\boldsymbol{\varepsilon}^{\mathrm{p}}, z, \xi, T\right). \end{aligned} \tag{4.4}$$

and

$$\begin{aligned} \dot{W} &= \dot{\psi}\left(\boldsymbol{\varepsilon}^{\mathrm{e}}, z, \xi, T\right) \\ &= \psi_{\boldsymbol{\varepsilon}^{\mathrm{e}}} \cdot \dot{\boldsymbol{\varepsilon}}^{\mathrm{e}} + \psi_z \cdot \dot{z} + \psi_\xi \cdot \dot{\xi} + \psi_T \cdot \dot{T}, \end{aligned} \tag{4.5}$$

the subscripts denote partial differentiation. The state equations for $\boldsymbol{\sigma}$ and s are:

$$\boldsymbol{\sigma} = \psi_{\boldsymbol{\varepsilon}^{\mathrm{e}}}, \quad s = -\psi_T, \tag{4.6}$$

ψ_z and ψ_ξ represent the thermodynamic forces associated with z and ξ. Using Eqns. (4.3), (4.5) and (4.6), the mechanical dissipation can be rewritten as

$$\begin{aligned} D &= \boldsymbol{\sigma} : \dot{\boldsymbol{\varepsilon}} - \boldsymbol{\sigma} : \dot{\boldsymbol{\varepsilon}}^{\mathrm{e}} - \psi_z \cdot \dot{z} - \psi_\xi \cdot \dot{\xi} \\ &= \boldsymbol{\sigma} : \dot{\boldsymbol{\varepsilon}}^{\mathrm{ori}} + \boldsymbol{\sigma} : \dot{\boldsymbol{\varepsilon}}^{\mathrm{p}} - \psi_z \cdot \dot{z} - \psi_\xi \cdot \dot{\xi}. \end{aligned} \tag{4.7}$$

Substituting D into Eq. (4.2), one gets

$$\begin{aligned} & -T\psi_{T\boldsymbol{\varepsilon}^{\mathrm{e}}}\dot{\boldsymbol{\varepsilon}}^{\mathrm{e}} - T\psi_{Tz}\dot{z} - T\psi_{T\xi}\dot{\xi} - T\psi_{TT}\dot{T} = \boldsymbol{\sigma} : \dot{\boldsymbol{\varepsilon}}^{\mathrm{ori}} + \boldsymbol{\sigma} : \dot{\boldsymbol{\varepsilon}}^{\mathrm{p}} \\ & -\psi_z \cdot \dot{z} - \psi_\xi \cdot \dot{\xi} - \operatorname{div}\boldsymbol{q} + r. \end{aligned} \tag{4.8}$$

Rearranging the expressions in Eq. (4.8), the following equation that governs the temperature evolution in time is obtained:

$$\lambda\dot{T} = r - \operatorname{div}\boldsymbol{q} + Q^{\mathrm{e}} + Q^{\mathrm{P}} + Q^{z}, \tag{4.9}$$

where

$$\lambda = -T\psi_{TT}, \tag{4.10}$$

$$Q^{\mathrm{e}} = T\psi_{T\boldsymbol{\varepsilon}^{\mathrm{e}}}\dot{\boldsymbol{\varepsilon}}^{\mathrm{e}}, \tag{4.11}$$

$$Q^{\mathrm{P}} = \boldsymbol{\sigma} : \dot{\boldsymbol{\varepsilon}}^{\mathrm{p}} - (\psi_\xi \cdot \dot{\xi} - T\psi_{T\xi}\dot{\xi}), \tag{4.12}$$

$$Q^{z} = \boldsymbol{\sigma} : \dot{\boldsymbol{\varepsilon}}^{\mathrm{ori}} - (\psi_z \cdot \dot{z} - T\psi_{Tz}\dot{z}). \tag{4.13}$$

$-T\psi_{TT}$ accounts for the specific heat capacity per unit volume and is denoted λ for simplicity. Q^{e} is the heating due to thermoelastic effects and is zero here. Q^{P} is the heating due to thermoplastic effects and Q^z is the heating due to phase transformation and martensite orientation.

Equation (4.12) shows that the total plastic work ($\boldsymbol{\sigma} : \dot{\boldsymbol{\varepsilon}}^{\mathrm{p}}$) is equal to heat ($Q^{\mathrm{P}}$) plus the energy stored via plastic hardening($\psi_{\xi} \cdot \dot{\xi} - T\psi_{T\xi}\dot{\xi}$) , as stated by Rosakis et al. (2000). The stored energy related to plastic hardening can be written as:

$$E_{\mathrm{st}}^{\xi} = \psi_{\xi} \cdot \dot{\xi} - T\psi_{T\xi}\dot{\xi}, \tag{4.14}$$

where $T\psi_{\xi T}\dot{\xi}$ represents the heating associated with hardening.

Similarly, the hysteresis work induced by phase transformation ($\boldsymbol{\sigma} : \dot{\boldsymbol{\varepsilon}}^{\mathrm{ori}}$) in Eqn. (4.13) is equal to heat (Q^z) plus the stored energy, E_{st}^{z}, which is:

$$E_{\mathrm{st}}^{z} = \psi_{z} \cdot \dot{z} - T\psi_{Tz}\dot{z}, \tag{4.15}$$

where $T\psi_{zT}\dot{z}$ is the latent heat. In the case of forward phase transformation, the increase in free energy caused by phase transformation ($\psi_z \cdot \dot{z}$), consists of the latent heat ($T\psi_{zT}\dot{z}$) and the stored energy (E_{st}^{z}). Therefore, one can say that the total hysteresis work ($\boldsymbol{\sigma} : \dot{\boldsymbol{\varepsilon}}^{\mathrm{p}} + \boldsymbol{\sigma} : \dot{\boldsymbol{\varepsilon}}^{\mathrm{ori}}$) is converted into stored energy ($E_{\mathrm{st}}^{z} + E_{\mathrm{st}}^{\xi}$) and heating ($Q^{\mathrm{p}} + Q^{z}$).

Hence, the equation governing the temperature evolution (4.9) can be rewritten as follows[1]:

$$\lambda\dot{T} = r - \mathrm{div}\boldsymbol{q} + \boldsymbol{\sigma} : \dot{\boldsymbol{\varepsilon}} - \boldsymbol{\sigma} : \dot{\boldsymbol{\varepsilon}}^{\mathrm{e}} - E_{\mathrm{st}}^{z} - E_{\mathrm{st}}^{\xi}. \tag{4.16}$$

Integrating Eqn. (4.16) over one complete cycle and considering that the elastic strain energy is recoverable (i.e $\int_{\mathrm{cycle}} \boldsymbol{\sigma} : \dot{\boldsymbol{\varepsilon}}^{\mathrm{e}}\mathrm{d}t = 0$) and the heat generation r is zero, the following equation is obtained:

$$\lambda\Delta T = \int_{\mathrm{cycle}} \boldsymbol{\sigma} : \dot{\boldsymbol{\varepsilon}}\mathrm{d}t - \int_{\mathrm{cycle}} E_{\mathrm{st}}^{z}\mathrm{d}t - \int_{\mathrm{cycle}} E_{\mathrm{st}}^{\xi}\mathrm{d}t - Q^{\mathrm{cycle}}, \tag{4.17}$$

where ΔT is the temperature change and $Q^{\mathrm{cycle}} = \int_{\mathrm{cycle}}(\mathrm{div}\boldsymbol{q})\mathrm{d}t$ is the heat exchange. Figure 4.1 gives a schematic explanation of how the energy is stored inside a SMA after total unloading (Chowdhury and Sehitoglu, 2017): $\int_{\mathrm{cycle}} E_{\mathrm{st}}^{\xi}\mathrm{d}t$ is stored in dislocations; most of the energy stored through forward phase transformation is recovered. However, because of internal stresses due to existing dislocations and strain incompatibilities between neighboring grains, some material points remain in martensitic state after unloading, resulting in $\int_{\mathrm{cycle}} E_{\mathrm{st}}^{z}\mathrm{d}t$ (Brinson et al., 2004; Hamilton et al., 2005; Siredey et al., 2005; Kan and Kang, 2010; Sedmák et al., 2015; Chowdhury and Sehitoglu, 2017).

Similarly, integrating the equation of mechanical dissipation D, Eq. (4.7), over one complete

---

[1] The thermoelastic effect Q^{e} is taken zero

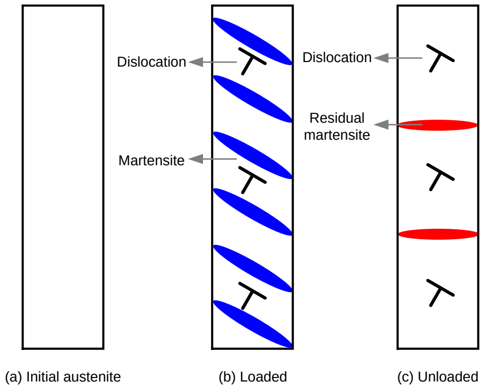

Figure 4.1 After unloading: the energy is stored (i) in dislocations (the occurrence of dislocation slip can be found in any investigations of the cyclic behavior of pseudoelastic SMAs); (ii) in residual martensites (Brinson et al., 2004; Hamilton et al., 2005; Siredey et al., 2005; Kan and Kang, 2010; Sedmák et al., 2015; Chowdhury and Sehitoglu, 2017).

cycle, gives

$$\begin{aligned}\int_{\text{cycle}} D\mathrm{d}t = \int_{\text{cycle}} \boldsymbol{\sigma} : \dot{\boldsymbol{\varepsilon}}\mathrm{d}t - \int_{\text{cycle}} \boldsymbol{\sigma} : \dot{\boldsymbol{\varepsilon}}^{\mathrm{e}}\mathrm{d}t - \int_{\text{cycle}} E_{\mathrm{st}}^{z}\mathrm{d}t - \int_{\text{cycle}} T\psi_{Tz}\dot{z}\mathrm{d}t \\ - \int_{\text{cycle}} E_{\mathrm{st}}^{\xi}\mathrm{d}t - \int_{\text{cycle}} T\psi_{T\xi}\dot{\xi}\mathrm{d}t.\end{aligned} \tag{4.18}$$

Here again $\int_{\text{cycle}} \boldsymbol{\sigma} : \dot{\boldsymbol{\varepsilon}}^{\mathrm{e}}\mathrm{d}t = 0$; the heating related the plastic hardening, $\int_{\text{cycle}} T\psi_{T\xi}\dot{\xi}\mathrm{d}t$, is negligible. Because the latent heat is released during forward phase transformation and absorbed during the reverse one, the variation of latent heat during one complete cycle should be zero. However, when residual martensite variants exist as explained in the previous paragraph, the latent heats released during forward phase transformation and absorbed during the reverse will no longer balance each other, resulting in a positive energy difference, defined as $l_r = \int_{\text{cycle}} T\psi_{Tz}\dot{z}\mathrm{d}t$. As a result, the integral for D simplifies to

$$\int_{\text{cycle}} D\mathrm{d}t = \int_{\text{cycle}} \boldsymbol{\sigma} : \dot{\boldsymbol{\varepsilon}}\mathrm{d}t - \int_{\text{cycle}} E_{\mathrm{st}}^{z}\mathrm{d}t - \int_{\text{cycle}} E_{\mathrm{st}}^{\xi}\mathrm{d}t - l_r. \tag{4.19}$$

if we define

$$E_{\mathrm{st}}^{\text{cycle}} = \int_{\text{cycle}} E_{\mathrm{st}}^{z}\mathrm{d}t + \int_{\text{cycle}} E_{\mathrm{st}}^{\xi}\mathrm{d}t \tag{4.20}$$

as the total energy stored during on complete cycle, and using Eqns. (4.17) and (4.19) one can obtain

$$\begin{aligned} &\lambda \Delta T = \int_{\text{cycle}} D\mathrm{d}t + l_r - Q^{\text{cycle}}, \\ &\text{with} \int_{\text{cycle}} D\mathrm{d}t + l_r = \int_{\text{cycle}} \boldsymbol{\sigma} : \dot{\boldsymbol{\varepsilon}}\mathrm{d}t - E_{\text{st}}^{\text{cycle}}. \end{aligned} \tag{4.21}$$

The heat sources during one complete cycle are the mechanical dissipation (due to the thermo-plastic effect and the martensite orientation and reorientation) and l_r, the positive difference of the latent heat between the forward and reverse phase transformation (when residual martensite variants remain). In fact, because l_r can be regarded as a heat source itself, $\int_{\text{cycle}} D\mathrm{d}t + l_r$ may be replaced by a generalized dissipation term D_{cycle} (hereinafter referred as the dissipation), and Eqn. (4.21)can be rewritten as

$$\begin{aligned} &\lambda \Delta T = D_{\text{cycle}} - Q^{\text{cycle}} \\ &\text{with } D_{\text{cycle}} = \int_{\text{cycle}} \boldsymbol{\sigma} : \dot{\boldsymbol{\varepsilon}}\mathrm{d}t - E_{\text{st}}^{\text{cycle}}, \end{aligned} \tag{4.22}$$

which means that, *the total hysteresis work during one complete cycle is equal to the sum of the dissipation and the stored energy.*

4.3 Characterization of the shakedown state

During pseudoelastic cyclic loading, SMAs undergo a transient phase in which different physical processes are triggered; namely forward and reverse transformations, martensite orientation and reorientation, plastic slip deformation and plastic hardening. After a few number of cycles the evolution of these dissipative mechanisms stabilize and reach a shakedown state in a way comparable to plastic shakedown in “classical” metals. It is well known that this shakedown state plays an important role in the prediction of fatigue lifetime (Moumni et al., 2005). In this section, a precise characterization of the shakedown state in SMAs will be given.

4.3.1 The evolution of energy in one cycle

Consider the SMA wire shown in Figure 4.2. The most of the heat is transferred from the specimen to the surroundings through convection; a small amount of heat is conducted through the grips. These two forms of heat transfer can be represented by an overall lumped convective coefficient h (Yin et al., 2014) which leads, on the circumferential surface, to the following

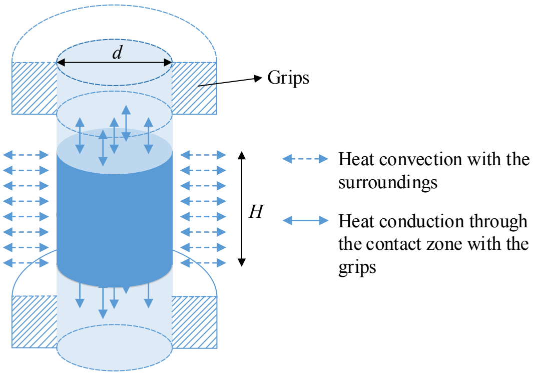
d
Grips
H
Heat convection with the surroundings
Heat conduction through the contact zone with the grips

Figure 4.2 Heat transfer in a SMA wire. To avoid the influence of grips, heat conduction through the grips is characterized by a lumped convective coefficient (Yin et al., 2014), and the average temperature evaluated in a 10 mm region at the middle part of the wire is used for analysis.

equation:

$$\boldsymbol{q} \cdot \boldsymbol{n} = h\,[T(t) - T_{\text{ext}}], \tag{4.23}$$

where T_{ext} is the external temperature. Using Eq. (4.23) and the specimen geometry given in Figure 4.2, Eq. (4.22) can be rewritten as follows:

$$\begin{aligned} &\lambda \cdot \Delta T_N = D_{\text{cycle}} - \frac{4}{d}\int_0^{t_p} h\,[T(t) - T_{\text{ext}}]\,\mathrm{d}t, \\ &\text{with} \quad D_{\text{cycle}} = \int_0^{t_p} \boldsymbol{\sigma} : \dot{\boldsymbol{\varepsilon}}\mathrm{d}t - E_{\text{st}}^{\text{cycle}}, \end{aligned} \tag{4.24}$$

where d is the diameter of the wire and t_p is the period of the cyclic loading. When the heat transfer to the surroundings is not sufficient to balance dissipation, an increase in temperature (ΔT_N) occurs and affects the mechanical behavior of the SMA.

For a hypothetical ideal SMA under isothermal condition, no defects nor plastic deformations take place during the pseudoelastic deformation. As a consequence, no energy is accumulated in dislocations nor in residual martensite variants; there is no heating of the material (the temperature remains constant, $\Delta T_N = 0$, see Figure 4.3a). Consequently, the dissipation is equal to the hysteresis work and is completely transferred to the surroundings:

$$\begin{aligned} &E_{\text{st}}^{\text{cycle}} = 0, \\ &D_{\text{cycle}} = \int_{\text{cycle}} \boldsymbol{\sigma} : \dot{\boldsymbol{\varepsilon}}\mathrm{d}t = \frac{4}{d}\int_0^{t_p} h\,[T(t) - T_{\text{ext}}]\,\mathrm{d}t, \end{aligned} \tag{4.25}$$

In the case of a real SMA, plastic deformations are triggered and energy is stored in

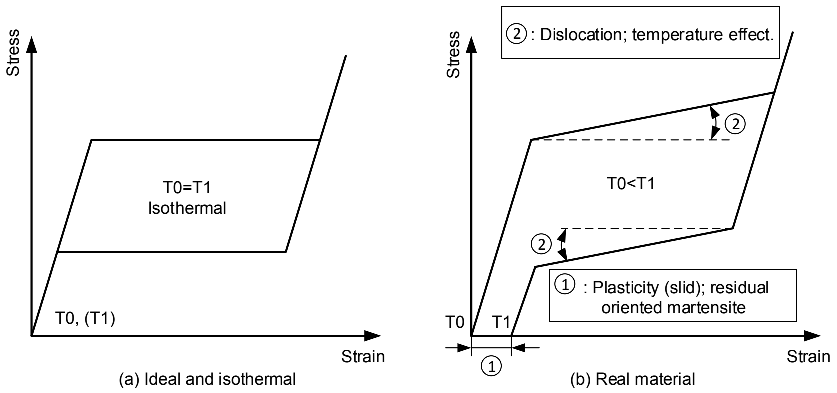

Figure 4.3 Mechanical behavior of a pseudoelastic SMA: (a) a hypothetical ideal SMA; (b) a real SMA.

dislocations. Simultaneously, residual oriented martensite variants occur, themselves storing some energy as well (see Figure 4.3b). If the heat transferred to the surroundings is less than the dissipation, the temperature increases from T_0 to T_1. As a result, the following balance equation holds for any complete cycle:

$$
\begin{aligned}
&E_{\mathrm{st}}^{\mathrm{cycle}} \neq 0, \\
&D_{\mathrm{cycle}} = \int_{\mathrm{cycle}} \boldsymbol{\sigma} : \dot{\boldsymbol{\varepsilon}} \mathrm{d}t - E_{\mathrm{st}}^{\mathrm{cycle}} = \lambda \cdot \Delta T_N + \frac{4}{d} \int_0^{t_p} h \left[T(t) - T_{\mathrm{ext}} \right] \mathrm{d}t.
\end{aligned}
\tag{4.26}
$$

4.3.2 Energy analysis at the shakedown state

When submitted to a mechanical cyclic loading, SMA undergo a thermomechanical coupling due to phase transformation. Hence, the mechanical loading induces a temperature variation. The experiment results of the evolution of thermal and mechanical responses until the shakedown state is reached in the case of cyclic loading of an SMA wire have been given in chapter 2.3, Figure 2.7. The temperature variation ΔT_N and the magnitude of heat transfer $\frac{4}{d} \int_0^{t_p} h \left[T(t) - T_{\mathrm{ext}} \right] \mathrm{d}t$ corresponding to Figure 2.7 are plotted in Figure 4.4 where the value of lumped convective coefficient h is taken to be 85 W/(m^2·K); this agrees with the average value of h used by Yin et al. (2014). In fact, h is not a constant, it changes with the variation of temperature between the specimen and the surroundings. Still, a constant h has been used knowing that although the heat transfer during one cycle calculated by $\frac{4}{d} \int_0^{t_p} h \left[T(t) - T_{\mathrm{ext}} \right] \mathrm{d}t$ is not precise, it will reflect the evolution of heat transfer from cycle to cycle. As the temperature oscillation tends toward stabilization, the cyclic heat transfer to the surroundings also reaches a constant value; the temperature change ΔT_N tends to zero, meaning that no further energy will go into heating of the material to increase the mean temperature. The total hysteresis work

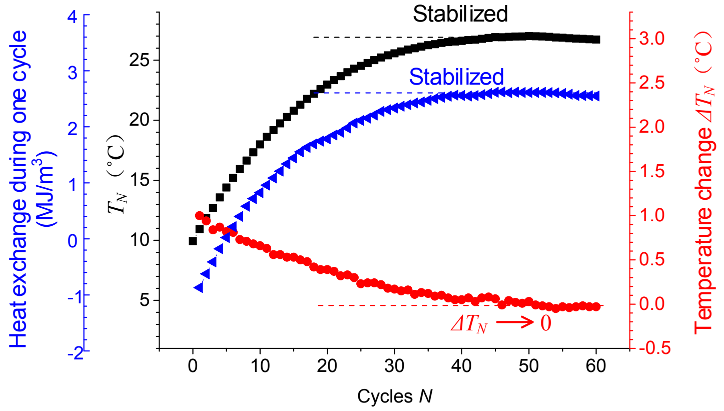

Figure 4.4 Stabilization of thermal response under stress controlled loading with $\sigma_{\max}$ = 471.3MPa at 1Hz (heat exchange is calculated by $\frac{4}{d}\int_0^{t_p} h\,(T(t) - T_{\mathrm{ext}})\,\mathrm{d}t$, where h is taken to be as 85W/(m^2·K)).

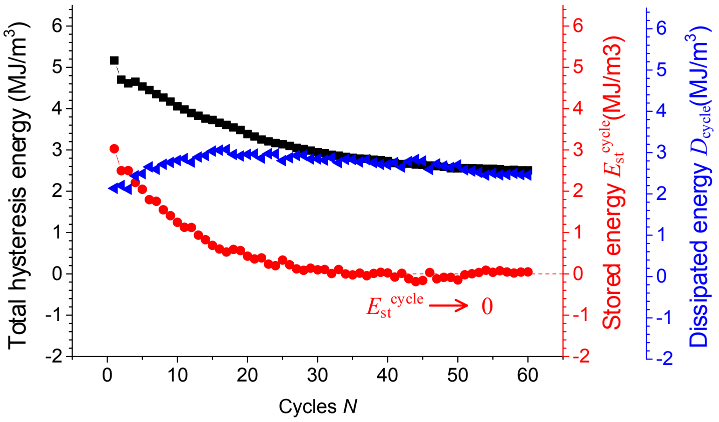

Figure 4.5 Evolutions of dissipation D_{cycle}, stored energy $E_{\mathrm{st}}^{\mathrm{cycle}}$ and total hysteresis energy $\int_0^{t_p} \boldsymbol{\sigma} : \dot{\boldsymbol{\varepsilon}}\mathrm{d}t$ under stress controlled loading with $\sigma_{\max}$ = 471.3 MPa at 1Hz.

$\int_{\mathrm{cycle}} \boldsymbol{\sigma} : \dot{\boldsymbol{\varepsilon}}\mathrm{d}t$ and the heating $\lambda \cdot \Delta T_N$ can directly be evaluated from experimental results. As a consequence, the dissipation D_{cycle} and the stored energy $E_{\mathrm{st}}^{\mathrm{cycle}}$ can be obtained using Eq. (4.26) and are plotted in Figure 4.5. The results show that the dissipation and the total hysteresis energy gradually stabilize. Synchronously, the stored energy tends to zero, $E_{\mathrm{st}}^{\mathrm{cycle}} \longrightarrow 0$, and no further energy is accumulated as a result of plastic hardening and phase transformation because the dislocations (measured by ξ) and the residual martensite variants get saturated. It is worth noting that, for a real SMA, the stored energy $E_{\mathrm{st}}^{\mathrm{cycle}}$ is never equal to zero. Even when the shakedown state is reached at the macro scale, there is still evolution of dissipative mechanisms at the micro scale where avalanches of dislocations and micro defects occur within the material. However, compared to the hysteresis work and the heat transfer to the surroundings at macro-scale, the stored energy is small. Consequently, when the shakedown state is reached, Eq. (4.26) becomes

$$D_{\text{cycle}} = \int_0^{t_p} \boldsymbol{\sigma} : \dot{\boldsymbol{\varepsilon}} \mathrm{d}t = \frac{4}{d} \int_0^{t_p} h \left[T(t) - T_{\text{ext}} \right] \mathrm{d}t, \tag{4.27}$$

which means that *all the dissipation at the shakedown state, which can be now regarded as the total hysteresis energy at macro-scale, will completely be released to the surroundings.*

4.3.3 Temperature analysis at the shakedown state

Heat balance equation (4.27) allows the evaluation of the temperature level of the SMA at the shakedown state. If a mean temperature T^*_{mean} is defined as:

$$h \cdot [T^*_{\text{mean}} - T_{\text{ext}}] \cdot t_p = \int_0^{t_p} h \cdot [T(t) - T_{\text{ext}}] \mathrm{d}t, \tag{4.28}$$

Then Eq. (4.27) becomes

$$D_{\text{cycle}} = \int_0^{t_p} \boldsymbol{\sigma} : \dot{\boldsymbol{\varepsilon}} \mathrm{d}t = \frac{4h}{d} \cdot [T^*_{\text{mean}} - T_{\text{ext}}] \cdot t_p. \tag{4.29}$$

Here the following mean temperature is defined:

$$T^*_{\text{mean}} = T_{\text{ext}} + \frac{d}{4h \cdot t_p} \cdot \int_0^{t_p} \boldsymbol{\sigma} : \dot{\boldsymbol{\varepsilon}} \mathrm{d}t, \tag{4.30}$$

Note that T^*_{mean} is different from $T_{\text{mean}} = (T_{\max} + T_{\min})/2$. It represents a state of balanced energy at which the heat transferred out equals the hysteresis dissipation, meaning no further dissipated energy is accumulated inside the material, and the mean temperature, T^*_{mean}, does not increase further. Its value is determined only by the hysteresis dissipation, frequency and the heat exchange condition (geometry size, heat exchange coefficient, etc.). In fact, as shown in Figures 2.9-2.11 and Figures 2.13-2.15, the waveforms of temperature oscillations become asymmetric and sharp for high frequencies where a mean temperature, $T_{\text{mean}} = (T_{\max} + T_{\min})/2$ has no physical meaning.

Integrating Eq. (4.16) over the loading path (time: $0 \longrightarrow t_p/2$) gives:

$$\begin{aligned} \int_0^{t_p/2} \lambda \dot{T} \mathrm{d}t = & \int_0^{t_p/2} \boldsymbol{\sigma} : \dot{\boldsymbol{\varepsilon}} \mathrm{d}t - \int_0^{t_p/2} \boldsymbol{\sigma} : \dot{\boldsymbol{\varepsilon}}^{\mathrm{e}} \mathrm{d}t - \int_0^{t_p/2} E^{\xi}_{st} \mathrm{d}t - \int_0^{t_p/2} E^{z}_{st} \mathrm{d}t \\ & - \frac{4}{d} \int_0^{t_p/2} h \left[T(t) - T_{\text{ext}} \right] \mathrm{d}t. \end{aligned} \tag{4.31}$$

As discussed in chapter 4.3, when the shakedown state is reached, the plastic deformation reaches saturation, and the stored energy related to plastic hardening per cycle tends to zero. The situation associated with phase transformation is however different: the phase transformation is a reversible process which undergoes a large variation in recoverable free energy. Hence, the stored energy, tends to zero after one complete cycle ($E_{\mathrm{st}}^{\mathrm{cycle}} \to 0$), but during forward phase transformation, it increases to a much larger value than zero, $E_{\mathrm{st}}^{\mathrm{loading}} \gg 0$, because of an increase in recoverable free energy. Neglecting the stored energy related to plastic hardening and replacing E_{st}^{z} with its detailed definition as used in Eq. (4.15) gives:

$$\begin{aligned}\int_0^{t_p/2} \lambda \dot{T} \mathrm{d}t = \int_0^{t_p/2} (\boldsymbol{\sigma} : \dot{\boldsymbol{\varepsilon}} - \boldsymbol{\sigma} : \dot{\boldsymbol{\varepsilon}}^{\mathrm{e}} - \frac{\partial \psi}{\partial z} \cdot \dot{z}) \mathrm{d}t - \int_0^{t_p/2} -T \frac{\partial^2 \psi}{\partial T \partial z} \dot{z} \mathrm{d}t \\ -\frac{4}{d} \int_0^{t_p/2} h \left[T(t) - T_{\mathrm{ext}}\right] \mathrm{d}t.\end{aligned} \tag{4.32}$$

The first term on the RHS is the mechanical dissipation generated during forward phase transformation [Eq. (4.7), when the plastic deformation is saturated]. If we define $l_0 = \int_0^{t_p/2} T \frac{\partial^2 \psi}{\partial T \partial z} \dot{z} \mathrm{d}t$ as the magnitude of the latent heat released during forward phase transformation (loading), then we have

$$\int_0^{t_p/2} \lambda \dot{T} \mathrm{d}t = \int_0^{t_p/2} D \mathrm{d}t - l_0 - \frac{4}{d} \int_0^{t_p/2} h \left[T(t) - T_{\mathrm{ext}}\right] \mathrm{d}t. \tag{4.33}$$

Considering Eq. (4.29), and the assumption that the dissipation during forward and reverse phase transformation is identical (He and Sun, 2010b), we have

$$\int_0^{t_p/2} D \mathrm{d}t = \frac{4h}{d} \cdot (T_{\mathrm{mean}}^{*} - T_{\mathrm{ext}}) \cdot \frac{t_p}{2} = \int_0^{t_p/2} \frac{4h}{d} (T_{\mathrm{mean}}^{*} - T_{\mathrm{ext}}) \mathrm{d}t. \tag{4.34}$$

Substituting into Eq. (4.33), we have

$$l_0 = \lambda \cdot \Delta T_l + \frac{4h}{d} \int_0^{t_p/2} [T(t) - T_{\mathrm{mean}}^{*}] \mathrm{d}t. \tag{4.35}$$

where ΔT_l is the temperature increase during loading. As shown in Figure 4.6. This equation states that during loading, one part of the latent heat l_0 released is absorbed by the material and causes a rise in temperature; the remainder on the other hand is released to the surrounding through heat exchange.

Eq. (4.35) allows us to simplify the analysis by taking the dissipated energy in the mean temperature T_{mean}^{*}, as a constant “environment” temperature; it illustrates that, during loading, the latent heat is released with one part going into heating of the material and thus causing an

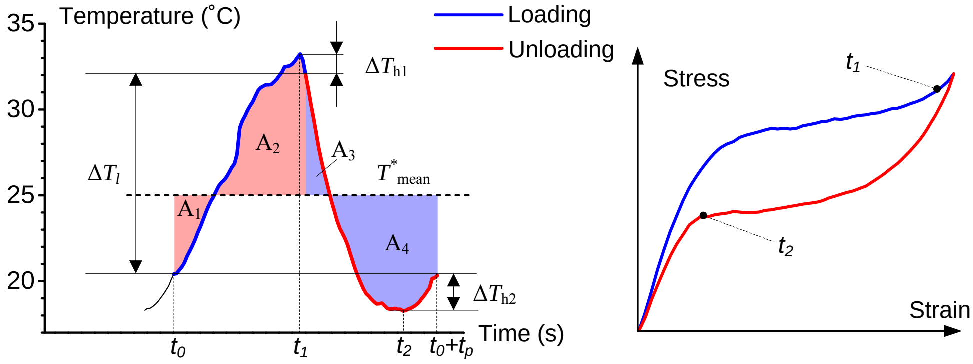

Figure 4.6 The synchronized temperature evolution during one stabilized cycle: strain controlled loading; maximum strain=6.58%; 0.01 Hz.

increase in temperature, ΔT_l; the other part being released to the "surroundings" (corresponding to the mean temperature T^*_{mean}).

Similarly, during unloading,

$$l_0 = \lambda \cdot (-\Delta T_{\text{un}}) - \frac{4h}{d} \int_{t_p/2}^{t_p} [T(t) - T^*_{\text{mean}}] \mathrm{d}t. \tag{4.36}$$

where ΔT_{un} is the total temperature decrease during unloading. Apparently, for the stabilized cycle, $\Delta T_l = \Delta T_{\text{un}}$, we have

$$\left| \frac{4h}{d} \int_0^{t_p/2} [T(t) - T^*_{\text{mean}}] \mathrm{d}t \right| = \left| \frac{4h}{d} \int_{t_p/2}^{t_p} [T(t) - T^*_{\text{mean}}] \mathrm{d}t \right|. \tag{4.37}$$

When a balance state is reached, the amount of the heat released to the "surroundings" during loading (see Figure 4.6, $\frac{4h}{d}$ times the difference of area A_2 and A_1) equals the amount of the heat absorbed from the "surroundings" during unloading ($\frac{4h}{d}$ times the difference of area A_4 and A_3).

Particularly, from $t_1 \longrightarrow t_p/2$, and $t_2 \longrightarrow t_p$, the deformations are elastic, and no latent heat is released nor absorbed. We have:

$$\lambda \cdot (-\Delta T_{\text{h1}}) = -\frac{4h}{d} \int_{t_1}^{t_p/2} [T(t) - T^*_{\text{mean}}] \mathrm{d}t, \tag{4.38}$$

$$\lambda \cdot \Delta T_{\text{h2}} = -\frac{4h}{d} \int_{t_2}^{t_p} [T(t) - T^*_{\text{mean}}] \mathrm{d}t. \tag{4.39}$$

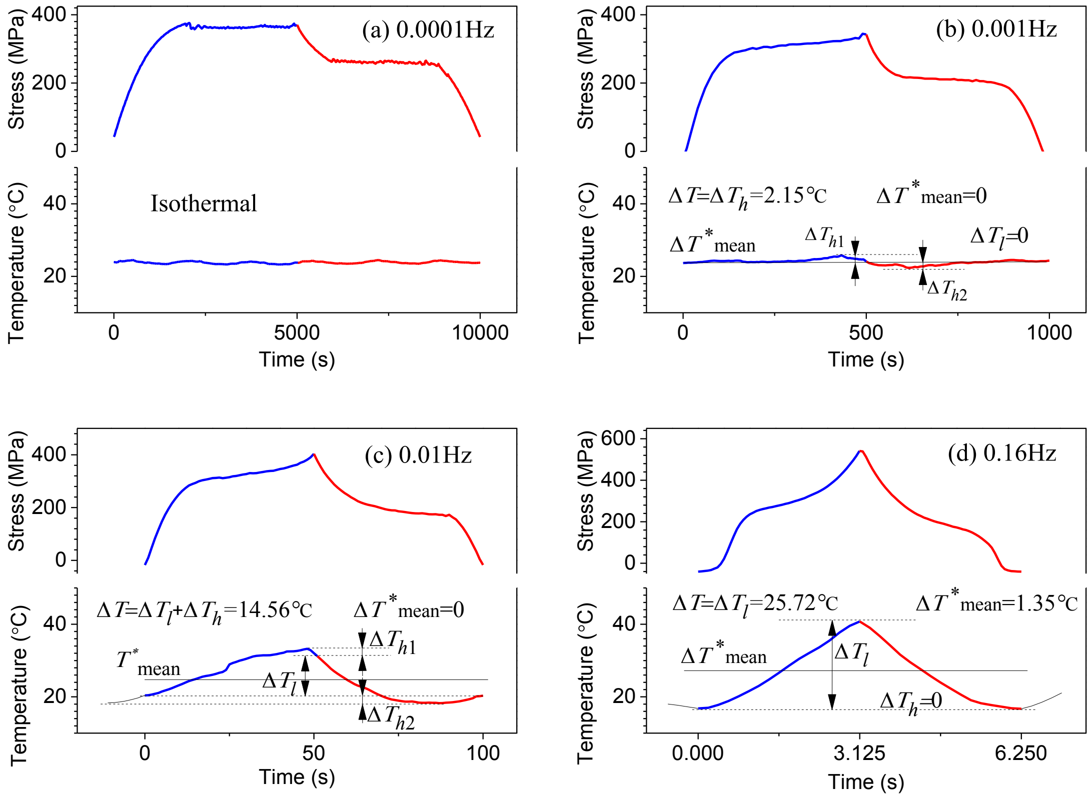

Figure 4.7 Stress and temperature evolutions during one stabilized cycle under strain controlled loading with 6.58% maximum strain, the blue curve corresponds to loading and the red one corresponds to unloading.

The total temperature amplitude is

$$\Delta T = \Delta T_l + \Delta T_\mathrm{h}, \text{ with } \Delta T_\mathrm{h} = \Delta T_\mathrm{h1} + \Delta T_\mathrm{h2}. \tag{4.40}$$

Obviously, because the equation above depends on the period of the cyclic loading, ΔT strongly depends on the loading frequency:

- When the loading frequency is very low, the heat transfer capacity is almost infinite ($\rightarrow \infty$), hence, the temperature remains constant during the loading path (see Figure 4.7a);

- When the frequency increases, the heat exchange is less significant but still efficient to release all the latent heat before unloading. In this case, the temperature increases slightly and then decreases to meet the ambient temperature, ($\Delta T_l = 0$, see Figure 4.7b, Figure 4.8a,b), which means that the heat transfer is sufficient to release all the latent heat to the surroundings during loading (or absorb from surroundings during unloading).

Particularly, by comparing Figure 4.7a and 4.8a, one can conclude that when the stress controlled loading is used, it is quite difficult to obtain isothermal condition by decreasing the frequency because when the stress reaches σ_{Ms}, the phase transformation will start instantaneously and the real heat release rate will be much higher than that of the strain controlled test at the same frequency;

- When the frequency increases further, the heat transfer during elastic deformation will tend to zero. Thus, ΔT_h decreases (see Figures 4.7c and 4.8c) and tends to zero as well (see Figure 4.7d and 4.8d), ΔT being equal to ΔT_l.

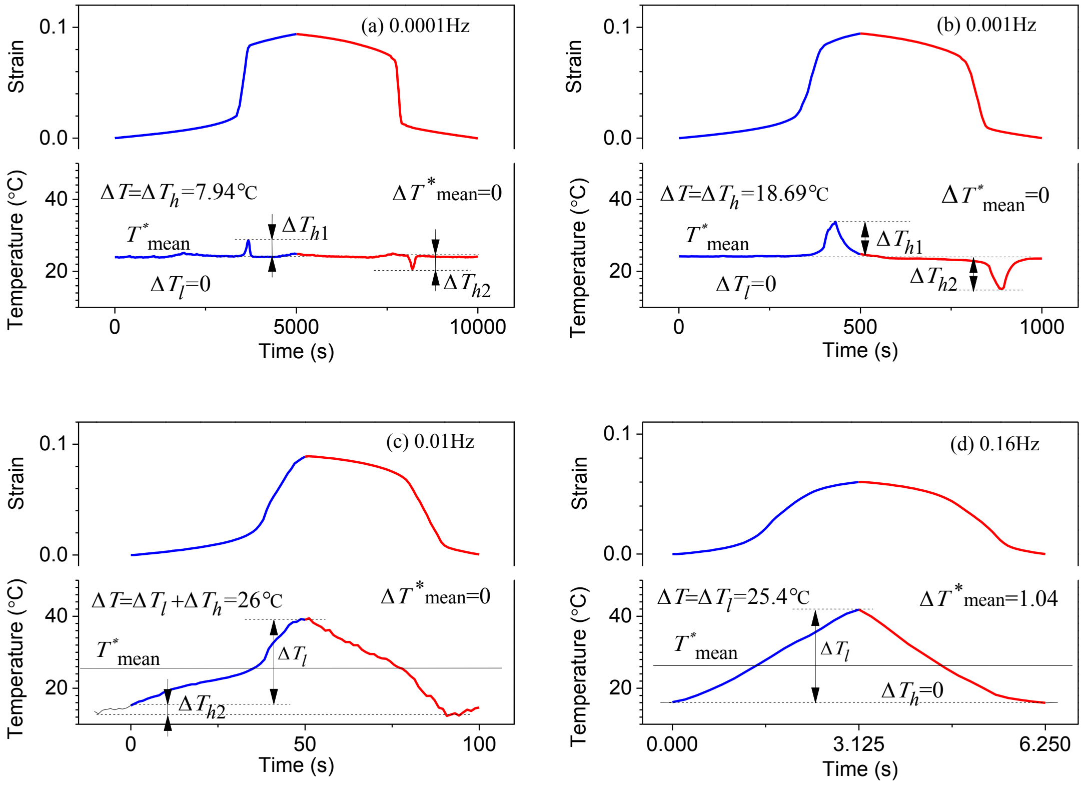

Figure 4.8 Stress and temperature evolution during one stabilized cycle under stress controlled loading with 471.3MPa maximum stress, the blue curve corresponds to loading and the red one corresponds to unloading.

The general form of total amplitude ΔT can therefore be written as

$$\Delta T = \frac{1}{\lambda}\left[l_0 - \frac{4h}{d}\left(\int_0^{t_p/2}[T(t) - T^*_{\text{mean}}]\mathrm{d}t - \int_{t_1}^{t_p/2}[T(t) - T^*_{\text{mean}}]\mathrm{d}t + \int_{t_2}^{t_p}[T(t) - T^*_{\text{mean}}]\mathrm{d}t\right)\right], \tag{4.41}$$

or simplifying

$$\Delta T = \frac{1}{\lambda}\left[l_0 - Q\right], \text{ with } Q = \frac{4h}{d}\int_{t|_{T=T_{\min}}}^{t|_{T=T_{\max}}}[T(t) - T^*_{\text{mean}}]\mathrm{d}t. \tag{4.42}$$

The calculation of Q requires a detailed evolution of temperature during one cycle. A simple equation as a function of temperature amplitude ΔT and the loading period t_p is proposed for the calculation of Q as follows:

$$Q = \mathcal{H} \cdot \Delta T \cdot t_p, \tag{4.43}$$

where $\mathcal{H}$ is the correction factor. An increase in frequency (decrease in t_p) leads to a decrease in Q, and when the frequency is fixed, increasing ΔT will increase the magnitude of Q; the heat convection coefficient h is included in the correction factor $\mathcal{H}$. Finally, ΔT can be written as

$$\Delta T = \frac{1}{1 + \frac{\mathcal{H}}{\lambda} \cdot t_p} \cdot \frac{l_0}{\lambda}. \tag{4.44}$$

Noting that the latent heat can be linked linearly to the phase transformation strain and assuming that the plastic deformation is saturated, the following formula for the temperature amplitude can be written:

$$\Delta T = \frac{1}{1 + \frac{\mathcal{H}}{\lambda} \cdot t_p} \cdot \frac{\zeta}{\lambda} \cdot (\varepsilon - \varepsilon^e). \tag{4.45}$$

where ζ is a material parameter. Neglecting the slight variation in elastic strain, the temperature amplitude can be represented as follows:

$$\Delta T = \frac{1}{1 + \kappa \cdot t_p} \cdot (a\varepsilon - b), \text{ with } \kappa = \frac{\mathcal{H}}{\lambda}, a = \frac{\zeta}{\lambda}, b = \frac{\varepsilon_e \cdot \zeta}{\lambda}. \tag{4.46}$$

Obviously, when the frequency is sufficiently high to reach an adiabatic state, the amplitude ΔT reaches a saturated value:

$$\Delta T|_{t_p \to 0} = \frac{l_0}{\lambda} = a\varepsilon - b. \tag{4.47}$$

As has been shown in chapter 2, a significant reduction in temperature amplitude occurs in stress controlled tests when the frequency is continuously increased; this is because the increase in the temperature level makes the phase transformation more difficult and the the applied stress is no longer capable to drive the same fraction of phase transformation as at low frequencies. The relationship between saturated temperature amplitude and the total strain under stress controlled tests given in Figure 2.14 is plotted in Figure 4.9. The result confirms a linear relation between ΔT and ε and identifies the parameters in Eq. (4.47) as $a = 513.35$ °C and $b = 6.81$ °C. Using non-saturated temperature amplitude data given in Figure 4.7 (all the

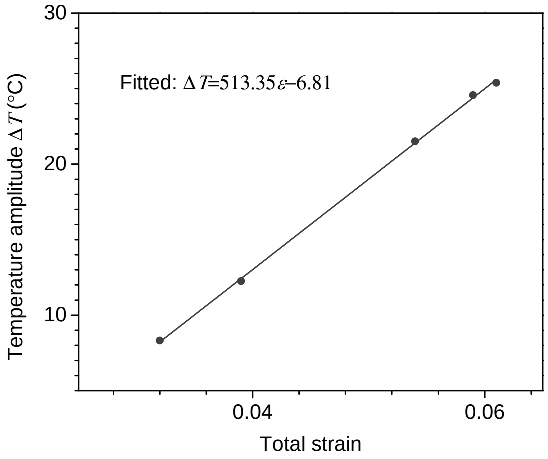

Figure 4.9 Saturated temperature amplitude ΔT versus total strain ε under stress controlled loading with maximum stress=471.3 MPa (original experimental results are given in Figure 2.14).

temperature amplitudes here are at shakedown state; "non-saturated" means that the amplitudes could increase further with the frequency), the identification of κ gives 0.0085 s^{-1}.

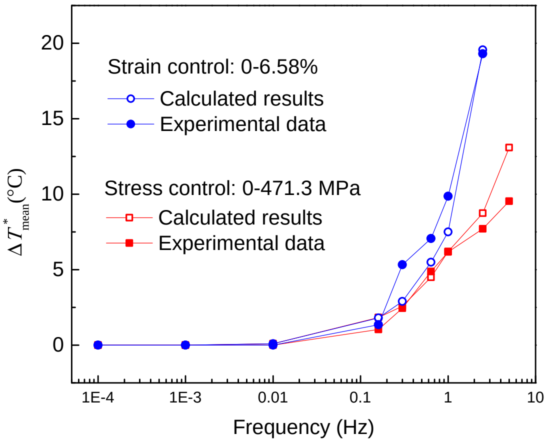

Figure 4.10 Evolution of mean temperature with loading frequency: comparisons of the calculated results against the experimental data given in Figure 2.11, 2.14, 4.7 and 4.8 (h is taken to be as 85W/(m^2·K)).

Finally, the temperature oscillation at the shakedown state can be calculated: Eq. (4.30) for mean temperature and Eq. (4.46) for temperature amplitude. The results are plotted in Figure 4.10 and 4.11 respectively (corresponding to the experimental results given in Figure 2.11 and 4.7 for strain control, and Figure 2.14 and 4.8 for stress control). The calculated results and the experimental ones agree very well. It is important to note that, non-saturated temperature

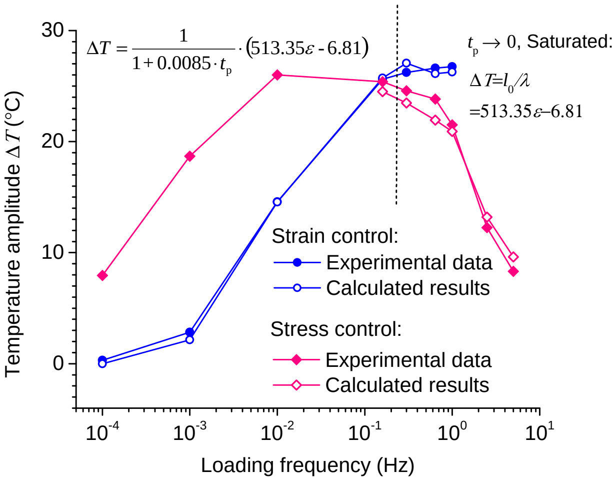

Figure 4.11 Evolution of temperature amplitude with loading frequency: comparisons of the calculated results against the experimental data given in Figure 2.11, 2.14, and 4.7.

amplitudes obtained under stress controlled loading (Figure 4.8) cannot be calculated using Eq. (4.46) because the real phase transformation rate cannot be controlled.

4.4 Fatigue analysis of SMAs

During the shakedown state, changes in the micro-structure were neglected and the macro-scale value of the stored energy, $E_{\text{st}}^{\text{cycle}}$ was taken to be zero. At micro-scale, however, the stored energy is not zero and still accumulates cycle after cycle; when its level reaches a critical value, fatigue cracks initiate and propagate, leading to an instantaneous release of energy. This discrete process in micro-scale is repeated with cyclic loading until the failure, although the macro-scale response remains approximately stable. This has been demonstrated by Dunand-Châtellet and Moumni (2012) using the framework of Self Organized Criticality (SOC); in their paper, fatigue failure precursors are identified with the crossover between the two scale free, dislocation based and micro-cracking based regimes. It is shown that the degradation of the steady shakedown state matches with the switch from the dislocation dominated mechanism to a micro-cracking dominated regime. This micro-cracking mechanism is followed by coalescence of micro-cracks and by the formation of a macro-crack that will cause the failure. In this section, we will show that the degradation of the steady shakedown state matches with the critical value of the stored energy which continues to accumulate with cyclic loading. Hence, the stored energy is the key factor to predict initiation and propagation of fatigue cracks in SMAs and its value is an adequate indicator for fatigue.

4.4.1 The stored energy at stabilized cycles in SMAs

As discussed in section 2, the total stored energy is due to phase transformation and plastic hardening. To further analyze the stored energy, the free energy ψ will be inserted into the equations; the free energy consists of the following three parts (Yu et al., 2014):

$$\psi = \psi^{\mathrm{e}} + \psi^{\mathrm{ori}} + \psi^{\mathrm{p}}, \tag{4.48}$$

where ψ^{e} is the elastic energy, ψ^{ori} is the energy related to phase transformation and the martensite orientation and reorientation, and ψ^{p} is the energy related to plastic deformation. The free energy related to the phase transformation can be written as follows (Zaki and Moumni, 2007a; Moumni et al., 2008):

$$\psi^{\mathrm{ori}} = C(z,T) + \psi^{\mathrm{A\text{-}M}} + \psi^{\mathrm{M\text{-}M}}, \tag{4.49}$$

where $C(z,T)$ is the heat density associated with the phase change, $\psi^{\mathrm{A\text{-}M}}$ represents part of the free energy associated with transformation from austenite to martensite, and $\psi^{\mathrm{M\text{-}M}}$ accounts for interaction energy due to orientation of martensite and orientation-independent interaction among martensite variants.

Using Eqn.(4.15); $E^{z}_{\mathrm{st}} = \psi_z \cdot \dot{z} - T\psi_{Tz} \cdot \dot{z}$, the stored energy related to phase transformation can be written as follows:

$$E^{z}_{\mathrm{st}} = \frac{\partial C(z,T)}{\partial z} \cdot \dot{z} + \frac{\partial \psi^{\mathrm{A\text{-}M}}}{\partial z} \cdot \dot{z} + \frac{\partial \psi^{\mathrm{M\text{-}M}}}{\partial z} \cdot \dot{z} - T\psi_{Tz} \cdot \dot{z}. \tag{4.50}$$

The first term $\frac{\partial C(z,T)}{\partial z} \cdot \dot{z}$ represents the heat change due to phase transformation (latent heat) and it is canceled by the last term $T\psi_{Tz} \cdot \dot{z}$. Consequently, during one complete cycle, we have:

$$E^{z,\mathrm{cycle}}_{\mathrm{st}} = \int_{\mathrm{cycle}} \frac{\partial \psi^{\mathrm{A\text{-}M}}}{\partial z} \cdot \dot{z}\mathrm{d}t + \int_{\mathrm{cycle}} \frac{\partial \psi^{\mathrm{M\text{-}M}}}{\partial z} \cdot \dot{z}\mathrm{d}t, \tag{4.51}$$

where $\frac{\partial \psi^{\mathrm{A\text{-}M}}}{\partial z}$ is the driving force for austenite A to transform into martensite M and $\frac{\partial \psi^{\mathrm{M\text{-}M}}}{\partial z}$ is the driving force for martensite orientation and the orientation-independent interactions. To make Eq. (4.51) more clear, it can be written as:

$$\begin{aligned} E^{z,\mathrm{cycle}}_{\mathrm{st}} &= (\psi^{\mathrm{A\text{-}M}}_{N} - \psi^{\mathrm{A\text{-}M}}_{N-1}) + (\psi^{\mathrm{M\text{-}M}}_{N} - \psi^{\mathrm{M\text{-}M}}_{N-1}) \\ &= \Delta\psi^{\mathrm{A,M}}_{N}. \end{aligned} \tag{4.52}$$

$\Delta\psi^{\mathrm{A,M}}_{N}$ is the total variation in mechanical free energy related to phase transformation from cycle $N \longrightarrow N + 1$. Similarly, the stored energy in dislocations, $E_{\mathrm{st}}^{\xi,\mathrm{cycle}}$, equals the variation in mechanical free energy related to plastic hardening from cycle $N \longrightarrow N + 1$, and the total stored energy is equal to the variation of the total mechanical energy. From an energy point of view, since the amount of mechanical energy required to transform a given fixed phase proportion of austenite into martensite under the same temperature condition is constant, more mechanical energy is stored during cycle N, less mechanical energy needs to be applied during cycle $N + 1$, as given by

$$E_{\mathrm{st}}^{\mathrm{cycle}N} = \Delta\psi_N^{\mathrm{mechanical}} = e_N - e_{N+1}, \tag{4.53}$$

where $E_{\mathrm{st}}^{\mathrm{cycle}N}$ is the energy stored inside the material during cycle N; $\Delta\psi_N^{\mathrm{mechanical}}$ is the variation of the total mechanical free energy during cycle N; e_N and e_{N+1} are the applied energy that drives the forward phase transformation (up to same martensite fraction) during cycle N and $N + 1$ respectively . For an ideal SMA in isothermal condition, the micro-structure of the material does not change after one complete cycle; the mechanical free energy totally recovers to its original value and no energy is stored (all hysteresis energy is transferred as heat to the surroundings). However, in the case of a real SMA, due to the existence of defects, the micro-structure cannot recover to its original state; some energy is stored through accumulation of dislocations and growth of residual martensite variants.

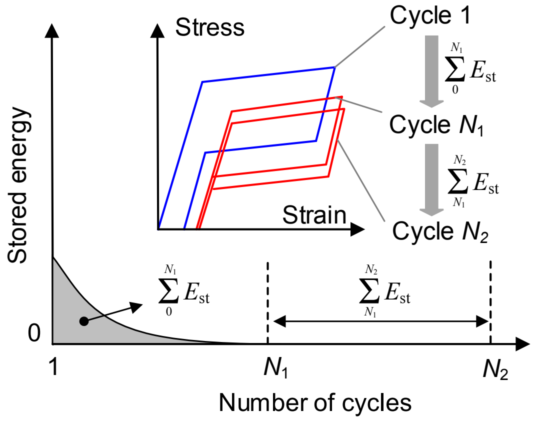
Stress
Strain
Cycle 1
$\sum_{0}^{N_1} E_{\mathrm{st}}$
Cycle N_1
$\sum_{N_1}^{N_2} E_{\mathrm{st}}$
Cycle N_2
Stored energy
0
$\sum_{0}^{N_1} E_{\mathrm{st}}$
$\sum_{N_1}^{N_2} E_{\mathrm{st}}$
1
N_1
N_2
Number of cycles

Figure 4.12 Schematic of the impact of the accumulated stored energy on macro response of SMAs.

As has indicated in section 3, the stored energy during one complete cycle at shakedown state is too small to be measured by conventional experimental methods (it tends to zero at macro scale). However, although the changes in micro-structure of material is negligible in each cycle at shakedown state, the accumulation of the micro changes from cycle to cycle can still make a difference in the macro-scale response (Zhang et al., 2017). As shown in Figure 4.12, from cycle 1 to N_1, the macro response of the SMA is stabilized, and stored energy per cycle tends to zero; from cycle N_1 to N_2, however, the macro response is still changing. According to

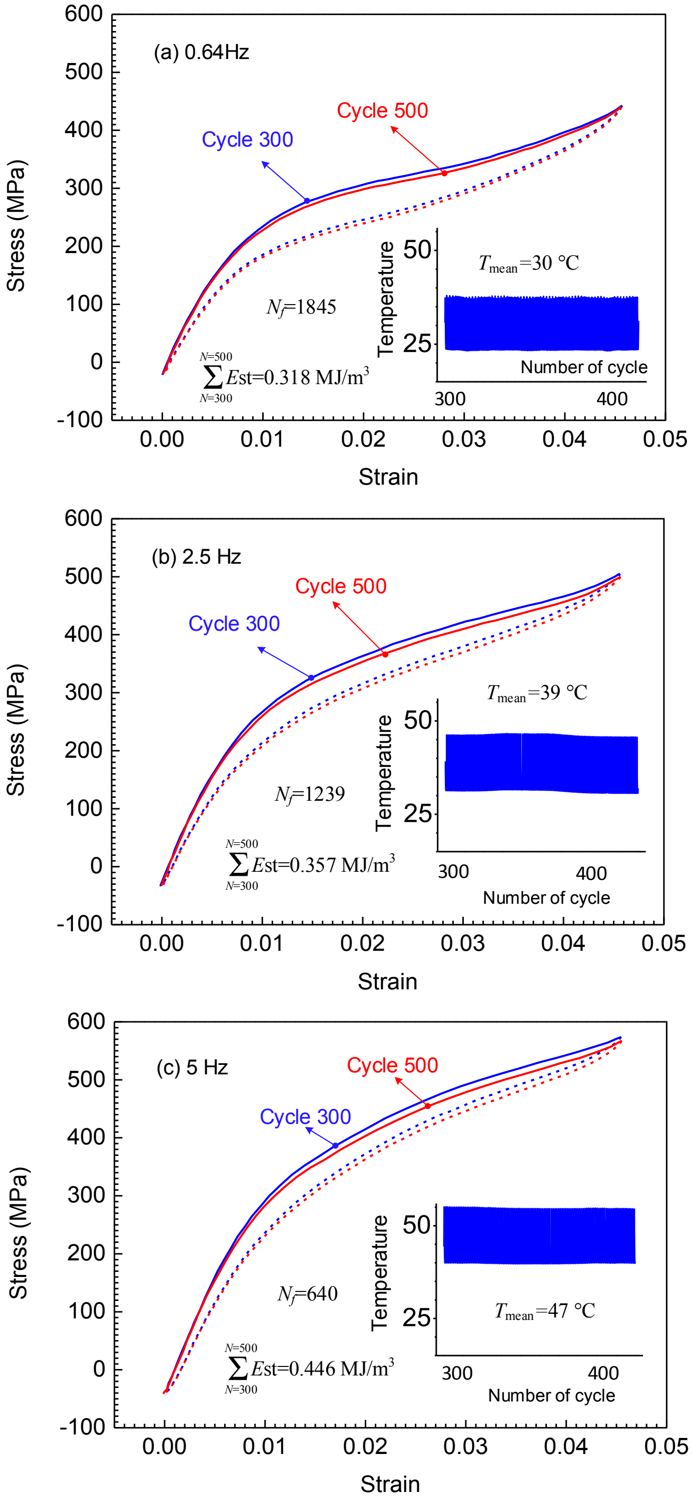

Figure 4.13 Thermal and mechanical response for cycle 300 and cycle 500 under strain control loading $\Delta\varepsilon$=4.61% at (a) 0.64 Hz, (b) 2.5 Hz and (c) 5 Hz.

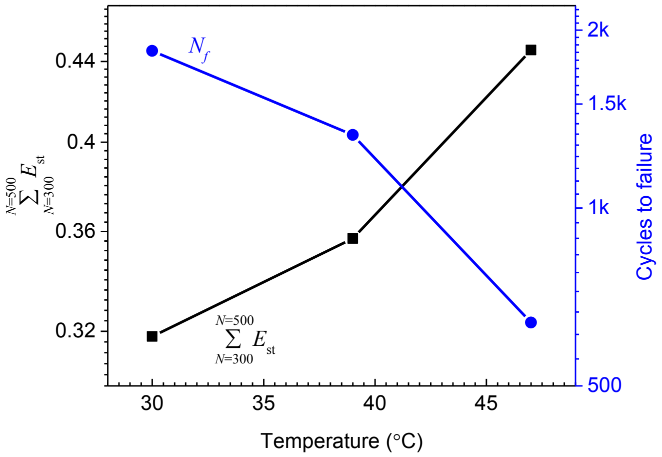

Figure 4.14 The evolutions of $\sum_{N=300}^{N=500} E_{\mathrm{st}}$ and the N_f on the mean temperature of the material based on the results given in Figure 4.13 .

Eq. (4.53), the difference of applied energy that drives forward phase transformation between cycle N_1 and N_2 (expressed as e_{N_1} and e_{N_2} respectively) is the stored energy accumulated from cycle N_1 to N_2:

$$\sum_{N_1}^{N_2} E_{\mathrm{st}} = e_{N_1} - e_{N_2}. \tag{4.54}$$

The thermal and mechanical response of cycle 300 and cycle 500 for the strain controlled tests (the phase transformation reaches the same level) with the strain amplitude $\Delta\varepsilon = 4.61\%$ are given in Figure 4.13 and then summarized in Figure 4.14; the results clearly show that with the increase of frequency, the temperature of the material rises and causes an increase in the accumulation of the stored energy and a reduction in fatigue lifetime. This can be easily explained: the martensitic phase transformation is sensitive to temperature; when temperature increases, the austenite becomes more stable and therefore higher energy is needed to keep the material points stay in martensite state.

4.4.2 Energy-based explanation of the thermomechanical coupling in the low cycle fatigue of SMAs

It is well known that the thermomechanical coupling has a strong influence of low cycle fatigue of SMAs (Zhang et al., 2017); fatigue lifetime under strain controlled loading decreases for all strain amplitudes with increasing the loading frequency, while for stress control, the fatigue lifetime shows a maximum stress-dependent trend: for different maximum stresses, the trend in variation of fatigue lifetime with frequency is different. This can be explained by the stored energy based on the theoretical and experimental results presented in section 4.1: (i) for strain controlled loading, the phase transformation is triggered up to the same level for all the frequencies because the deformation amplitude is fixed; higher loading frequencies weaken the heat transfer and cause an increase in temperature. As a result, the stored energy increases and shorten the fatigue lifetime; (ii) for stress controlled loading, an increase in mean temperature of the material sometimes cause a reduction in phase transformation (because the maximum stress is fixed, and if the stress is lower than the martensite finish stress σ_{Mf}, the increase of phase transformation plateau can lead to a reduction in the amount of phase transformation), accompanied with a reduction of the temperature amplitude (less latent heat released/absorbed) as well as the potential source of dislocations or residual martensite. Consequently, for the loading which is sufficient high to complete the phase transformation, the situation is similar to the strain controlled loading: the amount of phase transformation is fixed (completed); higher frequency shorten the fatigue lifetime; if the applied loading is not enough to complete the phase transformation for high frequencies, the reduction in the maximum temperature of the material and the reduction in the potential source of dislocations or residual martensite can reduce the stored energy. This is why the fatigue lifetime shows a maximum stress-dependent trend under the stress controlled loading.

4.4.3 Stored-energy-based criterion for low cycle fatigue of SMAs

The stored energy can be used as an indicator to predict the fatigue lifetime (it has been used and validated for the fatigue of elastoplastic materials (Warren and Wei, 2010; Wan et al., 2014; Chen et al., 2017)), however, calculating the accumulation of the stored energy by using Eq. (4.54) is not suitable for the low cycle fatigue prediction because one need to record hundreds cycles after the shakedown state, which is not convenient for a practical use of the criterion. To overcome these drawbacks, as it will be shown below, the stored energy can be correlated to the stabilized strain energy.

Stored-energy-based criterion

The correlation of the stored energy with the total strain energy can be explained as follows: along cycling, dislocation avalanches are triggered causing incompatible inelastic deformations that induce local internal residual stresses (Cuniberti and Romero, 2004). Even when macroscopic stresses are below the transformation stresses, these local residual internal stresses are sufficiently high to induce local martensitic transformations that result in residual martensite variants; in other words, the material points in these residual martensite regions undergo pseudoelastic deformation under the internal stress even when the applied stress is suppressed.

Now let's focus on the metallurgical-mechanical state of a real SMA configuration Ω (Figure 4.15a) and assume that after N cycles the martensite fraction reaches z_0 during forward phase transformation, and after total unloading, the residual martensite fraction remaining is z_r. Then the stored energy in these residual martensite variants, denoted as $E_{\mathrm{st}}^{z_r}$, is the accumulation of $\int_{\mathrm{cycle}} E_{\mathrm{st}}^{z} \mathrm{d}t$ during all the previous cycles:

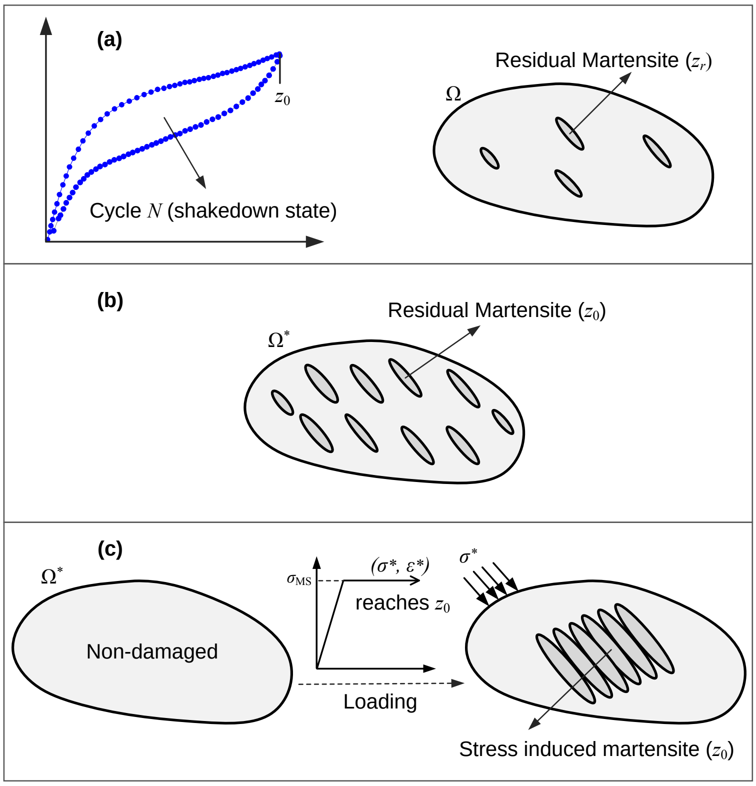
(a)
z_0
Cycle N (shakedown state)
Residual Martensite (z_r)
Ω
(b)
Residual Martensite (z_0)
Ω^*
(c)
Ω^*
Non-damaged
σ_{MS}
(σ^*, ε^*)
reaches z_0
Loading
σ^*
Stress induced martensite (z_0)

Figure 4.15 Martensite in different configurations at same temperature condition: (a) a real SMA configuration Ω, the volume fraction of residual martensite reaches z_r after N cycles; (b) a hypothetical SMA configuration Ω^*, the volume fraction of residual martensite is assumed to reach z_0; (c) the hypothetical non-damaged SMA configuration Ω^*, the volume fraction of martensite after forward phase transformation reaches z_0.

$$E_{\mathrm{st}}^{z_r} = \sum_{N} \int_{\mathrm{cycle}} E_{\mathrm{st}}^{z} \mathrm{d}t. \tag{4.55}$$

Considering that the martensite is completely oriented for any value of the martensite fraction z because the orientation finish stress is lower than the critical stress for forward phase transformation (Patoor et al., 2006a), and if the temperature keeps invariant, the amount of the stored energy in the residual martensite could be assumed to be proportional to the fraction of the residual martensite. Hence the relation $E_{\mathrm{st}}^{z_r}/z_r$ = constant, holds. In this case, for any other configuration Ω^* corresponding to a stored energy $E_{\mathrm{st}}^{z^*}$, and residual martensite volume fraction z^*, the following relation holds :

$$E_{\mathrm{st}}^{z^*} = \frac{E_{\mathrm{st}}^{z_r}}{z_r} \cdot z^*. \tag{4.56}$$

Now assume that in the configuration Ω^*, the volume fraction of residual martensite reaches z_0 (see Figure 4.15b, $z^* = z_0$), similarly the stored energy in residual martensite variants, denoted as $E_{\mathrm{st}}^{z_0,*}$, is given as

$$E_{\mathrm{st}}^{z_0,*} = \frac{E_{\mathrm{st}}^{z_r}}{z_r} \cdot z_0. \tag{4.57}$$

In addition, the total stored energy during one complete cycle consists of two parts: $\int_{\mathrm{cycle}} E_{\mathrm{st}}^{\xi}\mathrm{d}t$ and $\int_{\mathrm{cycle}} E_{\mathrm{st}}^{z}\mathrm{d}t$. However, these two parts are not independent; in fact, higher density of dislocations will result in a larger internal stress field as well as more "locked in" residual martensite variants (Brinson et al., 2004; Iadicola and Shaw, 2002; Hamilton et al., 2005; Siredey et al., 2005; Sedmák et al., 2015; Chowdhury and Sehitoglu, 2017), which means that an increase in $\int_{\mathrm{cycle}} E_{\mathrm{st}}^{\xi}\mathrm{d}t$ is accompanied by an increase in $\int_{\mathrm{cycle}} E_{\mathrm{st}}^{z}\mathrm{d}t$. If we assume that the variations in $\int_{\mathrm{cycle}} E_{\mathrm{st}}^{\xi}\mathrm{d}t$ and $\int_{\mathrm{cycle}} E_{\mathrm{st}}^{z}\mathrm{d}t$ are proportional, the relation shown in Eq. (4.57) holds for the total stored energy as shown below:

$$E_{\mathrm{st}}^{*} = \frac{E_{\mathrm{st}}}{z_r} \cdot z_0, \tag{4.58}$$

where E_{st}^{*} and E_{st} represent the accumulation of total stored energy in the hypothetical SMA, Ω^* (Figure 4.15b) and the real SMA, Ω (Figure 4.15a) respectively.

Having all the ingredients in hand, we can now link the stored energy to the total strain energy as follows: assume that the hypothetical non-damaged SMA configuration, Ω^* is loaded into forward phase transformation until reaching z_0 (Figure 4.15c). Since the configuration is assumed to be undamaged, no internal stresses are formed and the energy needed to drive the phase transformation can be calculated as:

$$e_0^* = \int_{\Omega} \int_{\mathrm{loading}} \sigma^* \mathrm{d}\varepsilon^* \mathrm{d}\Omega. \tag{4.59}$$

Then under same temperature condition, we have

$$e_0^* = E_{\mathrm{st}}^*, \tag{4.60}$$

where E_{st}^* is the total stored energy in the hypothetical configuration Ω^* (Figure 4.15b) due to internal stresses. This means that, under the same temperature, the energy needed to obtain the same volume fraction of martensite (z_0) in the hypothetical configuration is the same no matter what the supplied energy by internal stress (E^*_{st}; in this case z_0 is considered as residual martensite volume fraction) or by applied stress is(e^*_0; in this case z_0 is considered as martensite volume fraction reached after the application of the external load).

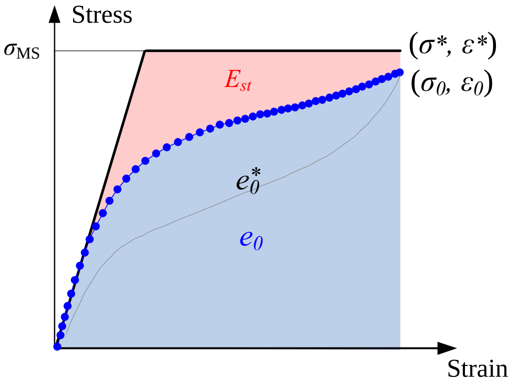

Figure 4.16 Stress-strain curves during forward phase transformation up to z_0: $\sigma_0 - \varepsilon_0$ corresponds to the real damaged SMA and $\sigma^* - \varepsilon^*$ corresponds to the hypothetical undamaged SMA.

Figure 4.16 compares the loading paths given in Figure 4.15a and c, $\sigma_0 - \varepsilon_0$ corresponds to the real damaged SMA, and $\sigma^* - \varepsilon^*$ corresponds to the hypothetical undamaged SMA[1]. For the curve $\sigma_0 - \varepsilon_0$ of the real damaged SMA, the slip deformations induce internal stresses that assist the formation of stress induced martensite. As a consequence, forward phase change yield stress decreases with increasing number of cycle. Similarly to Eq. (4.54), if we supply the energy $\int_\Omega \int_{\mathrm{loading}} \sigma_0 \mathrm{d}\varepsilon_0 \mathrm{d}\Omega$ to the hypothetical undamaged material, the volume fraction of martensite does not reach z_0; in fact, in order to reach z_0, the stored energy must be taken into account. This means that the difference of energy between the real damaged configuration and the hypothetical undamaged one is the accumulation of stored energy as shown below:

$$e^*_0 - e_0 = E_{\mathrm{st}}, \tag{4.61}$$

then combining Eqns (4.58), (4.60) and (4.61), we obtain

$$\frac{E_{\mathrm{st}}}{z_r} \cdot z_0 - e_0 = E_{\mathrm{st}}, \tag{4.62}$$

finally,

$$E_{\mathrm{st}} = \frac{z_r}{z_0 - z_r} \cdot e_0, \tag{4.63}$$

this equation illustrates that upon cyclic loading, as the residual martensite volume fraction accumulates and reaches z_r, the stored energy accumulates inside the SMA and supplies the energy needed to drive crack initiation and propagation. Now the problem is how to measure the value of the stabilized residual martensite fraction z_r. It is well known that during stress induced phase transformation, the martensite is completely oriented for any value of the martensite fraction because the orientation finish stress is lower than the critical stress for forward phase transformation, and the phase transformation strain can be expressed as (Patoor et al., 2006a; Zaki and Moumni, 2007b; Lagoudas et al., 2012; Cisse et al., 2016; Wang et al., 2017):

---

[1] The $\sigma^* - \varepsilon^*$ curve is unknown because upon cycling the stress-strain curve changes as a result of the thermomechanical coupling.

$$\boldsymbol{\varepsilon}_{z_0}^{\text{ori}} = z_0 \cdot \boldsymbol{\gamma}, \tag{4.64}$$

where $\boldsymbol{\varepsilon}_{z_0}^{\text{ori}}$ is the phase transformation strain corresponding to the martensite fraction z_0 and $\boldsymbol{\gamma}$ is the maximum orientation strain (its equivalent value is a material constant). In this case, for the proportional loadings, we have

$$z_0 = \frac{\mid \boldsymbol{\varepsilon}_{z_0}^{\text{ori}} \mid_{\text{eq}}}{\mid \boldsymbol{\gamma} \mid_{\text{eq}}}, \quad z_r = \frac{\mid \boldsymbol{\varepsilon}_{z_r}^{\text{r}} \mid_{\text{eq}}}{\mid \boldsymbol{\gamma} \mid_{\text{eq}}}, \quad \text{with} \mid \boldsymbol{\varepsilon} \mid_{\text{eq}} = \sqrt{\frac{2}{3}\boldsymbol{\varepsilon} : \boldsymbol{\varepsilon}}, \tag{4.65}$$

and therefore Eq. (4.63) can be written as

$$E_{\text{st}} = \frac{\mid \boldsymbol{\varepsilon}_{z_r}^{\text{r}} \mid_{\text{eq}}}{\mid \boldsymbol{\varepsilon}_{z_0}^{\text{ori}} \mid_{\text{eq}} - \mid \boldsymbol{\varepsilon}_{z_r}^{\text{r}} \mid_{\text{eq}}} \cdot e_0, \tag{4.66}$$

where $\boldsymbol{\varepsilon}_{z_r}^{\text{r}}$ is the residual strain related to the residual martensite z_r and the definition $\mid \boldsymbol{\varepsilon} \mid_{\text{eq}}$ represents the equivalent strains. As shown in Figure 4.17, when a SMA reaches the shakedown state, the saturated residual strain consists of two components: plastic strain and the irreversible strain related to the residual martensite. For the stabilized cycle (cycle 300 in Figure 4.17), residual martensite with the fraction z_r already exists inside the material before loading; during the forward phase transformation, the martensite fraction reaches its maximum value z_0 (z_0 up to 1 in Figure 4.17); then after unloading, only residual martensite (z_r) stays in martensite state. Apparently, the variation of the martensite fraction during one stabilized cycle equals the value of $z_0 - z_r$, which corresponds to the stabilized transformation strain(expressed as $\boldsymbol{\varepsilon}^{\text{ori}}$). As a consequence, Eq. (4.66) can be written as

$$E_{\text{st}} = \frac{\mid \boldsymbol{\varepsilon}_{z_r}^{\text{r}} \mid_{\text{eq}}}{\mid \boldsymbol{\varepsilon}^{\text{ori}} \mid_{\text{eq}}} \cdot e_0, \tag{4.67}$$

The residual strain related to the residual martensite ($\boldsymbol{\varepsilon}_{z_r}^{\text{r}}$) is difficult to be directly measured, however, as has been indicated above, the residual strains induced by plastic deformation and residual martensite are not independent: higher density of dislocations will result in a larger internal stress field as well as more “locked in” residual martensite variants (Brinson et al.,

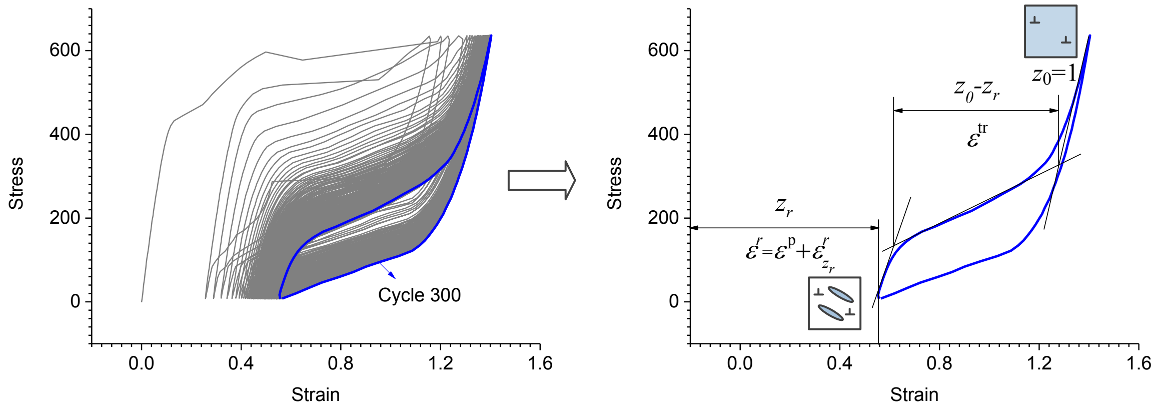

Figure 4.17 The analysis of the stabilized strain components.

2004; Iadicola and Shaw, 2002; Hamilton et al., 2005; Siredey et al., 2005; Sedmák et al., 2015; Chowdhury and Sehitoglu, 2017). As a consequence, $\boldsymbol{\varepsilon}^{\mathrm{r}}_{z_r}$ can be considered as a fraction of the total residual strain as:

$$\boldsymbol{\varepsilon}^{\mathrm{r}}_{z_r} = \nu\boldsymbol{\varepsilon}^{\mathrm{r}}. \tag{4.68}$$

Now Eq. (4.67) becomes

$$\frac{E_{\mathrm{st}}}{\nu} = \frac{\mid \boldsymbol{\varepsilon}^{\mathrm{r}} \mid_{\mathrm{eq}}}{\mid \boldsymbol{\varepsilon}^{\mathrm{ori}} \mid_{\mathrm{eq}}} \cdot e_0, \tag{4.69}$$

Although the coefficient ν is unknown, the term E_{st}/ν can be used as a generalized form of stored energy for the fatigue predictions. Figure 4.18 displays 12 groups of fatigue test results, where the stress-strain curve corresponds to cycle 300. The value of E_{st}/ν is calculated by Eq. (4.69); the fatigue lifetime and E_{st}/ν are plotted using a logarithmic scale in Figure 4.19a, the almost linear character of the data allows to represent E_{st}/ν in the following form:

$$\frac{E_{\mathrm{st}}}{\nu} = \frac{\mid \boldsymbol{\varepsilon}^{\mathrm{r}} \mid_{\mathrm{eq}}}{\mid \boldsymbol{\varepsilon}^{\mathrm{ori}} \mid_{\mathrm{eq}}} \cdot e_0 = \omega N_f^k, \tag{4.70}$$

where ω and k are material constants; E_{st}/ν is calculated using total strain energy, stabilized transformation strain and residual strain (1D in the results given in Figure 4.18). The error analysis of the criterion (4.70) is performed in Figure 4.19b, where experimental fatigue lifetime compares very well with the predictions of the criterion; the good predictivity of this criterion confirms that the stored-energy-based model is a reliable tool for the prediction of fatigue lifetime in SMAs.

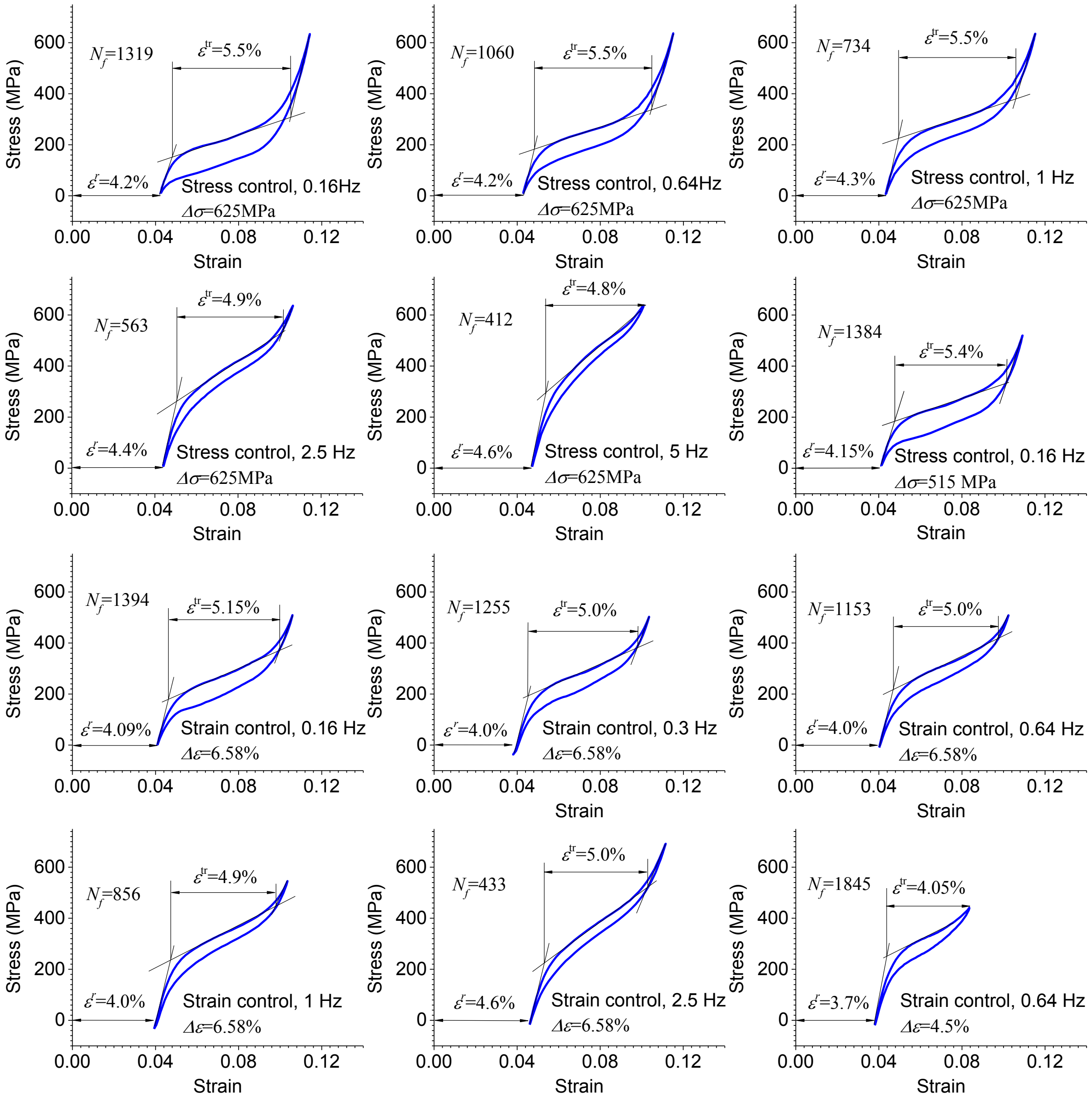

Figure 4.18 The fatigue test results with the stabilized stress-strain response (cycle 300). For the strain controlled tests, the specimens are first subjected to stress controlled loading for 20 cycles (maximum stress 637.0 MPa, 0.04 Hz) to accommodate large residual strains. Small residual strains still accumulate upon strain controlled cyclic loading and lead to a slight compression (within -30 MPa); the accumulated residual strain at cycle 300 is measured at zero-stress state.

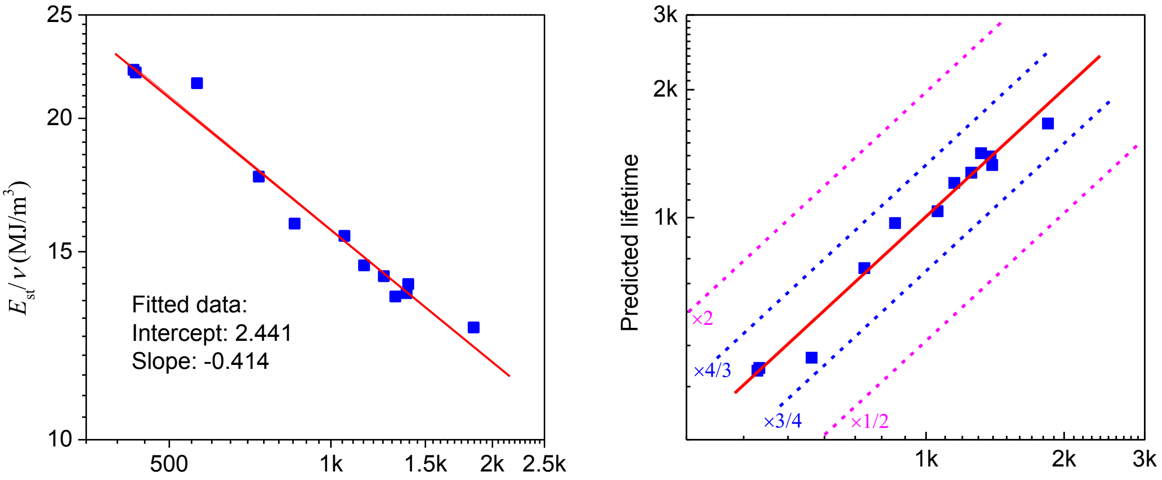

(a) Fatigue lifetime vs. generalized stored energy E_{st}/v

(b) Error analysis

Figure 4.19 (a) Fatigue lifetime vs. generalized stored energy E_{st}/v; (b) error analysis.

Comparison with the strain energy-based criterion

Figure 4.20 displays the predictions of the fatigue lifetime given in Figure 4.18 by the strain energy-based model (3.15). All of the points lie within half and twice lifetime and the predictions are acceptable. The comparison between Figure 4.19b and 4.20 shows that the

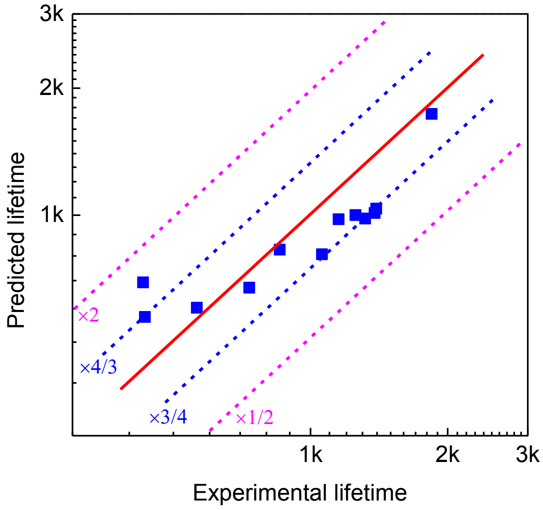

Figure 4.20 The predictions of the fatigue lifetime given in Figure 4.18 by the strain energy-based model (3.15).

stored-energy-based criterion has higher accuracy than the strain energy-based one. In fact, the difference between these two criteria resides on the proportion defined by $|\boldsymbol{\varepsilon}^r|_{\text{eq}} / |\boldsymbol{\varepsilon}^{\text{ori}}|_{\text{eq}}$

(see Eq. (4.70)), which represents the residual strain induced by unit volume fraction of phase transformation (hereinafter referred as Unit Transformation Induced Residual Strain, UTRIRS). It is well known that, during phase transformation, plastic deformation being triggered even if the applied macroscopic stress is lower than the yield stress of austenite or martensite phase is mainly due to the so-called transformation induced plasticity (TRIP) (Hamilton et al., 2005; Norfleet et al., 2009; Simon et al., 2010; Kato and Sasaki, 2013; Yu et al., 2015a): the unmatched inelastic deformation between austenite-martensite interfaces creates high local stresses, and this triggers dislocation slip. Apparently, more phase transformation produces larger number of austenite-martensite interfaces that accelerate TRIP, resulting in more dislocations slip (lager $\boldsymbol{\varepsilon}^{\mathrm{p}}$), and thus more "locked in" residual martensite variants (lager $\boldsymbol{\varepsilon}^{\mathrm{r}}_{z,r}$); this means that the residual strain is proportional to the volume fraction of phase transformation. It is not correct to say that UTRIRS is a material constant because the material state and experiment conditions can not be exactly identical for each test, however, there is no doubt that the variation in UTRIRS should be limited: for all the tests from 0.16Hz to 5Hz, the maximum variation in UTRIRS, $\mid \boldsymbol{\varepsilon}^{r} \mid_{\mathrm{eq}} / \mid \boldsymbol{\varepsilon}^{\mathrm{ori}} \mid_{\mathrm{eq}}$, is less than 20.3%. The limited variation in UTRIRS and the stored-energy-based criterion (4.70) together provide the physical foundation of the strain energy-based criterion. The stored-energy-based criterion has higher accuracy since it takes into account the variation in UTRIRS, however, the strain energy based criterion can be conveniently used in a larger variety of applications because it does not need to record the residual strain during stabilization, which in fact cannot be directly measured in some situations, e.g., the internal loops under strain control in pseudoelasticity (see Figure 3.5).

4.5 Conclusion

In this chapter, a new stored-energy-based fatigue criterion for shape memory alloys is proposed. To this end, and for the first time, a theoretical proof of the partition of the hysteresis work into dissipation and stored energy in SMAs is provided. Key conclusions of this study are listed as follows:

- During pseudoelastic deformation, the hysteresis work is partially dissipated into heat. The remainder, the so-called stored energy, in part accumulates in dislocations, and in part is stored as internal energy in residual martensite variants. During initial cycles, a large amount of dislocations and residual martensite variants form and persist which results in a large amount of stored energy that strongly affects the thermomechanical behavior. Upon cyclic loading, the number of dislocations and residual martensite variants tend to saturate, the amount of stored energy gradually decreases and finally tends to zero at macro-scale.

- Before the shakedown state reached, the amount of dissipation could be smaller than total hysteresis work, which means that the hysteresis work is not equal to the dissipated heat. In fact, part of the hysteresis goes into the stored energy. When the shakedown state is reached, the stored energy tends to zero at macro-scale, and the hysteresis work can be regarded as equal to the dissipation which is totally transferred to the surroundings.

- At micro-scale, the stored energy still accumulated along cycling; when it reaches a critical value, fatigue cracks initiate and propagate, leading to an instantaneous release of energy and to failure. The magnitude of stored energy depends on dislocations and residual martensite variants densities and increases with the temperature of the material. A stored-energy-based criterion for low cycle fatigue of SMAs is proposed, and the results show that the stored energy is the relevant parameter to predict the fatigue lifetime of SMAs.

Chapter 5

Low cycle fatigue crack initiation in shape memory alloys

In this chapter, a multiscale investigation of fatigue crack initiation in shape memory alloys (SMAs) based on Transformation Induced Plasticity (TRIP) is presented. A mechanism for fatigue crack initiation during cyclic stress-induced phase transformation along with theoretical model is proposed. The results show that, (i) TRIP appearing on phase transformation interfaces is the key factor that drives the fatigue crack initiation during cyclic stress-induced phase transformation in SMAs; (ii) maximum temperature during phase transformation is a relevant indicator to predict low-cycle fatigue of SMAs and, (iii) within the range of pseudoelasticity and below the plastic yield, low-cycle fatigue of SMAs is not directly correlated with the mechanical loads applied at macro-scale; in the sense that, if the maximum temperature reached during loading cycles is kept constant, the fatigue lifetime remains unchanged whatever the amplitude of the mechanical loading is. Based on the findings, a new criterion for pseudoelastic low-cycle fatigue of SMAs is proposed and validated experimentally.

5.1 Introduction

The previous chapters successfully show that phase transformation makes the mechanism of fatigue in SMAs much more complex than the one in “classical" materials because the material structure and the related physical fields (such as stress, strain, temperature, etc.) are highly influenced by phase transformation. In fact, it is well established that fatigue of SMAs is related to local phenomena occurring at meso-scopic (grain) scale (Shaw and Kyriakides, 1997a,b; Sittner et al., 2005; Feng and Sun, 2006; Pieczyska et al., 2006; Daly et al., 2007; He and Sun, 2010a; Zhang et al., 2010; Hallai and Kyriakides, 2013; Pieczyska et al., 2013; Reedlunn et al., 2014; Zhang and He, 2017). A series of experimental works on fatigue behavior of pseudoelastic NiTi plates have been proposed by Zheng et al. (2016b,a, 2017) and the results show that fatigue cracks initiate in the so-called *active zone* where SMAs undergo locally cyclic phase transformation. Many other experimental works at micro-scale or meso-scale using X-ray diffraction (XRD) (Koster et al., 2015; Sedmák et al., 2015), Scanning Electron Microscope (SEM) (Eggeler et al., 2004; Predki et al., 2006; Nayan et al., 2008; Frotscher et al., 2009; Rahim et al., 2013; Koster et al., 2015) and Transmission Electron Microscope (TEM) (McKelvey and Ritchie, 2001; Frotscher et al., 2009; Pelton, 2011) have been carried out. It is believed that fatigue damage in pseudoelastic SMAs is resulting from permanent dislocation slips that occur on phase transformation interfaces (Brinson et al., 2004; Delville et al., 2011; Kundin et al., 2015; Sedmák et al., 2015). Furthermore, dislocation slips (Condó et al., 2008; Delville et al., 2011; Gloanec et al., 2013; Polatidis et al., 2015), as well as residual oriented martensite *locked-in* by internal stress field induced by dislocations, (Iadicola and Shaw, 2002; Brinson et al., 2004; Hamilton et al., 2005; Siredey et al., 2005; Kan and Kang, 2010; Sedmák et al., 2015; Chowdhury and Sehitoglu, 2017), induce residual deformations. This residual strain has been chosen as an indicator for fatigue damage of SMAs (Lagoudas et al., 2009; Zheng et al., 2017). During stress induced phase transformation, the macro-stress applied to trigger the phase transformation is usually lower than the plastic yield of the material. Nevertheless, even when the macroscopic stress field is below the plastic yield, dislocation slips are triggered due to the so-called Transformation Induced Plasticity (TRIP) (Kang et al., 2009; Norfleet et al., 2009; Simon et al., 2010; Kato and Sasaki, 2013; Yu et al., 2015a; Paranjape et al., 2017): when phase transformation takes place, a high-level local stress field is created as a result of the unmatched deformation in austenite-martensite (A-M) interfaces (i.e., austenite-martensite interface, hereinafter referred to as A-M interface) which assist dislocations slip in the A-M interface. Upon cycling, the accumulation of dislocations get saturated and the mechanical response of SMAs reaches a stabilized state after dozens of cycles (Moumni et al., 2005; Morin et al., 2011b; Zaki and Moumni, 2007a; Gu et al., 2017; Wang et al., 2017). However, although TRIP is believed to be the key factor in fatigue crack initiation during cyclic stress induced phase transformation in SMAs (Wagner et al., 2008; Lagoudas et al., 2009; Zheng et al., 2016b, 2017), the physical mechanisms related to this process is still unclear and there is no theoretical model available to present a quantitative assessment of the fatigue crack initiation in SMAs.

This chapter aims at filling the aforementioned gap by giving an experimental and theoretical assessment of the link between TRIP and fatigue crack initiation in SMAs. In section 5.2, first the physical mechanism of fatigue crack initiation in shape memory alloys is presented, and then a theoretical TRIP-based model for crack initiation is established. Experimental validations of the model are presented in section 5.3. In section 5.4, some issues related to the low-cycle fatigue of SMAs are discussed including the dependence of the fatigue lifetime on the macroscopic mechanical loads as well as the spatial location of the fatigue failure. Finally, summary and conclusions are given in section 5.5.

5.2 TRIP-based modeling of fatigue crack initiation

In this section, first, a TRIP-based physical mechanism of fatigue crack initiation in pseudoelastic SMAs is provided; second, a theoretical TRIP-based model is established for the phenomenon.

5.2.1 Physical mechanism of fatigue crack initiation

As indicated in section 5.1, during stress-induced phase transformation within the range of pseudoelasticity and below the plastic yield, unmatched deformations in A-M interfaces create high local stresses that exceed plastic yield stress and trigger dislocation slip. Figure 5.1 gives a schematic of TRIP deformation: when a virgin SMA in the austenitic state is first subjected to an applied stress, dislocation slips are activated in A-M interfaces. Following the movement of A-M interfaces, the dislocations spread throughout the transformed regions (point i in Figure 5.1). When the applied stress is removed, the SMA recovers to the austenitic state, leaving a great number of dislocations and a macroscopic residual strain (point j in Figure 5.1). During subsequent pseudoelastic cycles, as a result of plastic hardening, the slip deformation becomes more difficult and higher local stress is needed to create new dislocation slip (point k in Figure

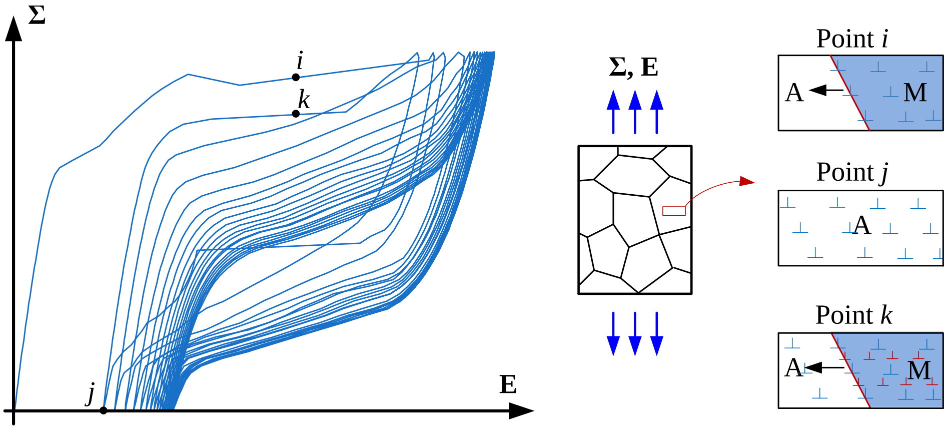

Figure 5.1 Schematic of TRIP deformation, $\mathbf{\Sigma}$ and $\boldsymbol{E}$ are global stress and strain, A and M represent austenite and martensite phases.

5.1). This process repeats itself with cyclic loading until the plastic yield surface reaches a size for which no new dislocation slip can be triggered; TRIP is saturated, the local stress is at its maximum value and the mechanical response of the SMA is stabilized.

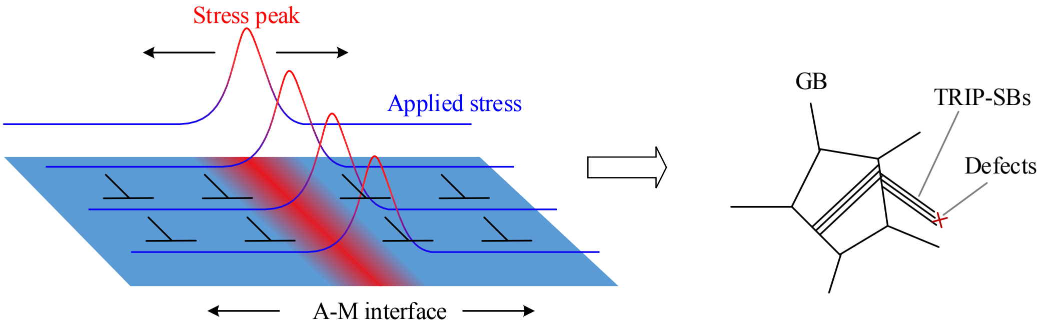

Figure 5.2 Schematic of stress peak in A-M interface initiating fatigue cracks through interactions between TRIP-SBs and grain boundary (GB), or other defects inside the material.

As shown in Figure 5.2, during subsequent cyclic phase transformation, it is expected that material points in martensitic regions will be swept over by the steady stress peak following the back and forth movement of the A-M interface. According to fatigue theory of ductile materials, fatigue cracks in SMAs initiate under cyclic stress peak probably via interactions among TRIP-SBs and grain boundaries (GB), or other defects inside the material.

5.2.2 Theoretical modeling

The stabilized state

During the pseudoelastic process (below macroscopic plastic yielding), three dissipative phenomena: phase transformation, martensite orientation and TRIP are considered; z, $\boldsymbol{\varepsilon}^{\mathrm{ori}}$ and $\boldsymbol{\varepsilon}^{\mathrm{p}}$ are the dissipative variables and the pseudo-potential of dissipation $\mathbb{D}$ is given by

$$\mathbb{D} = D(\dot{z}, \dot{\boldsymbol{\varepsilon}}^{\mathrm{ori}}, \dot{\boldsymbol{\varepsilon}}^{\mathrm{p}}). \tag{5.1}$$

Thermodynamic forces associated with the dissipative variables $\mathcal{A}_z$, $\mathcal{A}_{\boldsymbol{\varepsilon}^{\mathrm{ori}}}$, $\mathcal{A}_{\boldsymbol{\varepsilon}^{\mathrm{p}}}$, belong to the sub-gradients of the pseudo-potential of dissipation $\mathbb{D}$ as shown below:

$$\mathcal{A}_z \in \partial_{\dot{z}}\mathbb{D} \tag{5.2a}$$

$$\mathcal{A}_{\boldsymbol{\varepsilon}^{\mathrm{ori}}} \in \partial_{\dot{\boldsymbol{\varepsilon}}^{\mathrm{ori}}}\mathbb{D}, \tag{5.2b}$$

$$\mathcal{A}_{\boldsymbol{\varepsilon}^{\mathrm{p}}} \in \partial_{\dot{\boldsymbol{\varepsilon}}^{\mathrm{p}}}\mathbb{D}. \tag{5.2c}$$

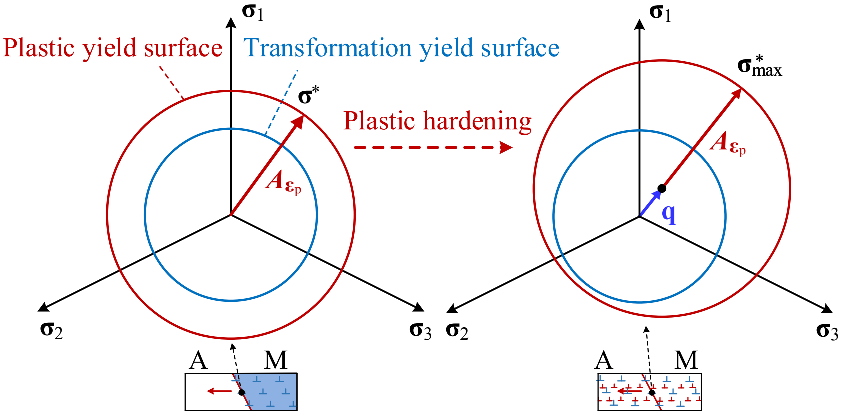

(a) During first cycle (b) At stabilized state

Figure 5.3 Local phase transformation and TRIP (π plane, where $\boldsymbol{\sigma}^*$ is the local stress in A-M interface that triggers TRIP and reaches the maximum $\boldsymbol{\sigma}^*_{\max}$ when the stabilized state is reached): (a) during first cycle, high level local stress $\boldsymbol{\sigma}^*$ created by the unmatched deformation in A-M interface activates local plasticity (b) the plastic yield surface changes as a result of plastic hardening; when stabilized state is reached, local stress $\boldsymbol{\sigma}^*$ reaches its highest value and no new plasticity is triggered.

As indicated in section 2.1, upon cyclic loading, the triggering of TRIP becomes more difficult due to plastic hardening and when the stabilized state is reached, the number of plastic slip bands per cycle tends to zero[1]. In this state, the local stress that activates TRIP (expressed as σ^*) reaches its maximum which is the critical stress corresponding to the stabilized yield surface (see Figure 5.3b), and is given by the following relation :

$$\mathcal{A}_{\boldsymbol{\varepsilon}^{\mathrm{p}}} = \boldsymbol{\sigma}^*_{\max} - \boldsymbol{B} \in \partial_{\dot{\boldsymbol{\varepsilon}}^{\mathrm{p}}}\mathbb{D}|_{\substack{\boldsymbol{\varepsilon}^*_{\mathrm{p}}\to\text{saturated}\\ \dot{\boldsymbol{\varepsilon}}^{\mathrm{p}}=0}}, \tag{5.3}$$

where $\boldsymbol{\varepsilon}^*_{\mathrm{p}}$ is the accumulated TRIP strain that is saturated and $\boldsymbol{B}$ is the back stress related to the kinematic hardening (see Figure 5.3b), which is defined by a kinematic hardening modulus tensor $\boldsymbol{H}$:

$$\boldsymbol{B} = \boldsymbol{H} : \boldsymbol{\varepsilon}^{\mathrm{p}}. \tag{5.4}$$

Finally, the steady stress peak discussed in section 2.1 can be calculated as:

$$\boldsymbol{\sigma}^*_{\max} - \boldsymbol{H} : \boldsymbol{\varepsilon}^*_{\mathrm{p}} \in \partial_{\dot{\boldsymbol{\varepsilon}}^{\mathrm{p}}}\mathbb{D}|_{\substack{\boldsymbol{\varepsilon}^*_{\mathrm{p}}\to\text{saturated}\\ \dot{\boldsymbol{\varepsilon}}^{\mathrm{p}}=0}}. \tag{5.5}$$

---

[1] Localized plastic deformation could still occur in some grains at the meso-scopic (grain) scale. However, compared to the large plastic strain before the stabilized state, this local plastic deformation during one cycle is negligible.

Since $\boldsymbol{\varepsilon}_{\mathrm{p}}^{*}$ is a saturated value in the stabilized state, the maximum stress peak $\boldsymbol{\sigma}_{\max}^{*}$ can be considered as a steady value.

Local-global relations

Assumption: *the martensite is completely oriented for any value of the martensite fraction because the orientation finish stress is lower than the critical stress for forward phase transformation* (Patoor et al., 2006b).

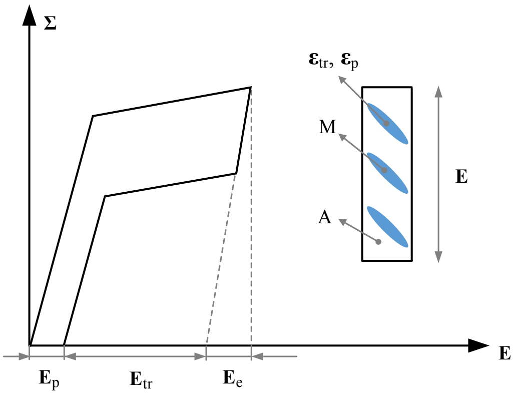

Figure 5.4 A schematic of phase transformation, $\boldsymbol{E}$, $\boldsymbol{E}_{\mathrm{p}}$ and $\boldsymbol{E}_{\mathrm{ori}}$ are global strains, $\boldsymbol{\varepsilon}_{\mathrm{p}}$ and $\boldsymbol{\varepsilon}_{\mathrm{ori}}$ are local strain components for TRIP and phase transformation.

Let $\boldsymbol{\Sigma}$ and $\boldsymbol{E}$ be the global (i.e. macroscopic in the sense of continuum mechanics) stress and strain as shown in Figure 5.4, phase transformation always initiates in some local material region and then propagates through out the entire domain. If the phase transformation is not complete, some material regions remain in austenitic state. Based on the *assumption* above, the local orientation strain is a constant strain tensor proportional to the deviatoric stress tensor; thus, the global phase transformation strain can be written as follows :

$$\boldsymbol{E}_{\mathrm{ori}} = z \cdot \boldsymbol{\varepsilon}^{\mathrm{ori}}. \tag{5.6}$$

Furthermore, TRIP triggers only in A-M interfaces and spreads within martensite regions. As a consequence, the relation between $\boldsymbol{E}^{\mathrm{p}}$ and $\boldsymbol{\varepsilon}^{\mathrm{p}}$ can be written as:

$$\boldsymbol{E}^{\mathrm{p}} = z \cdot \boldsymbol{\varepsilon}^{\mathrm{p}}. \tag{5.7}$$

Eq.(5.7) indicates that, at fixed temperature, an increase in $\boldsymbol{E}^{\mathrm{p}}$ is a result of an expansion of the phase transformation regions where TRIP is triggered.

When the stabilized state is reached, TRIP is saturated and we have:

$$\boldsymbol{E}_{\mathrm{p}}^{*} = z \cdot \boldsymbol{\varepsilon}_{\mathrm{p}}^{*}, \tag{5.8}$$

where the asterisk designates the saturated value. As a consequence, the stress peak defined in Eq. (5.5) can be written as:

$$\boldsymbol{\sigma}_{\mathrm{max}}^{*} - \boldsymbol{H} : \frac{\boldsymbol{E}_{\mathrm{p}}^{*}}{z} \in \partial_{\dot{\boldsymbol{\varepsilon}}^{\mathrm{p}}} \mathbb{D} \Big|_{\substack{\boldsymbol{E}_{\mathrm{p}}^{*}/z \rightarrow \mathrm{saturated} \\ \dot{\boldsymbol{\varepsilon}}^{\mathrm{p}} = 0}}. \tag{5.9}$$

Eq. (5.9) links local fields to global ones and makes the calculation of $\boldsymbol{\sigma}_{\mathrm{max}}^{*}$ by using the global response; $\boldsymbol{E}_{\mathrm{p}}^{*}/z$ is the upper limit of the plastic strain that can be triggered per unit volume of phase transformation (or in other words, it represents the dislocation density in the transformed region).

As indicated in section 2.1, under the cyclic stress peak $\boldsymbol{\sigma}_{\mathrm{max}}^{*}$, dislocations slip bands coalesce and form fatigue cracks. The above analysis shows that :

- Higher magnitude of $\boldsymbol{\sigma}_{\mathrm{max}}^{*}$ triggers more TRIP per unit volume of phase transformation and therefore a higher potential crack source density is introduced inside the material;
- Higher magnitude of $\boldsymbol{\sigma}_{\mathrm{max}}^{*}$ results in more potential crack source swept over by higher cyclic stress peak and results in acceleration of crack initiation.

Consequently, $\boldsymbol{\sigma}_{\mathrm{max}}^{*}$ can be chosen as the control force for fatigue crack initiation.

Multi-scale analysis of the local stress-peak

The analysis above shows that the local stress, $\boldsymbol{\sigma}_{\mathrm{max}}^{*}$ controls the fatigue crack initiation and has an intrinsic stabilized value that is independent of macro stress and strain. As shown in Figure 5.5, at the martensite band front, there are a number of grains undergoing phase transformation with different A-M interfaces (Yin et al., 2016; Zheng et al., 2016a). The values of $\boldsymbol{\sigma}_{\mathrm{max}}^{*}$ that are associated with those interfaces are difficult to be directly measured or calculated; however, as it will be shown in the next paragraph, they can be indicated by the temperature at the martensite band front, T_{front}, which can be regarded as a homogeneous state variable at small scale and is easy to be obtained at macro-scale:

$$\text{at grain } i: \ \boldsymbol{\sigma}_{\mathrm{max},i}^{*} = f(T_{\mathrm{front}}), \tag{5.10}$$

where i is the number of the grain at martensite band front. Eq. (5.10) links the mesoscopic stress peak to the macro-scale and it can be proven using an energy-based approach as follows:

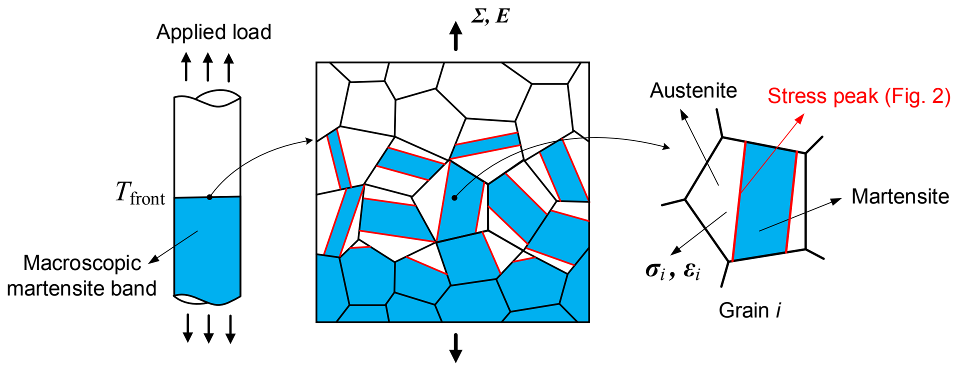
Applied load
Σ, E
Austenite
Stress peak (Fig. 2)
T_{front}
Martensite
Macroscopic martensite band
σ_i, ε_i
Grain i

Figure 5.5 Multi-scale analysis of the stress peak: macroscopic $\boldsymbol{\Sigma}$, $\boldsymbol{E}$ are defined at macro-scale and mesoscopic $\boldsymbol{\sigma}_i$, $\boldsymbol{\varepsilon}_i$ are defined at mesoscopic scale. Within the martensite band front, there are a number of grains undergoing phase transformation with different A-M interfaces. The local stress peak at each grain can be evaluated by the temperature at martensite band front (T_{front}), which can be regarded as a homogeneous state variable at mesoscopic scale and is very easy to be obtained at macro-scale.

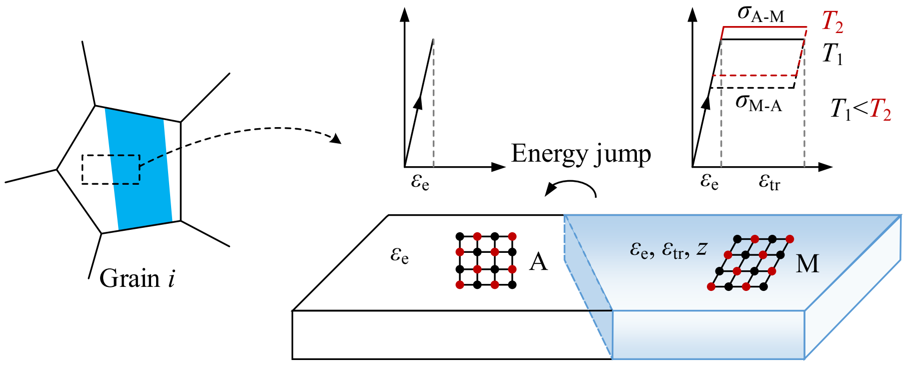
Grain i
Energy jump
ε_e
$\sigma_{\text{A-M}}$
T_2
T_1
$\sigma_{\text{M-A}}$
$T_1<T_2$
ε_e
ε_tr
ε_e
A
ε_e, ε_tr, z
M

Figure 5.6 Energy jump in A-M interface during forward phase transformation.

As shown in Figure 5.6, within grain i, we assume that there exists a theoretical state at which the local mechanical response is distributed homogeneously in austenitic and martensitic phases and is not continuous in the A-M interface (expressed as $\boldsymbol{\varepsilon}_i$, $\boldsymbol{\varepsilon}_{\mathrm{e},i}$, $\boldsymbol{\varepsilon}_{\mathrm{ori},i}$ and z_i, where $\boldsymbol{\varepsilon}_{\mathrm{ori},i}$ has a constant magnitude and $z_i = 1$ at martensitic phase and both of them are 0 in the austenitic phase). This state cannot exist in a real SMA because an energy jump in A-M interface occurs due to the energy difference between austenitic and martensitic phases. This energy jump results in a stress concentration in the A-M interface triggering local plastic flow. Hence, a higher energy jump in an A-M interface will result in a higher stress concentration, i.e. a higher value of $\boldsymbol{\sigma}^*_{\max}$, and as a consequence in more TRIP.

For an ideal SMA (cf. Figure 5.6), the calculation of the energy jump is carried out using the local Helmholtz free energy. As has been analyzed in chapter 4.2, the increase in free energy during forward phase transformation, expressed as $\psi_{z_i} \cdot \dot{z}_i$, consists of two parts: one part is the mechanical energy stored in martensite (expressed as $\dot{e}_{\mathrm{M},i}$), and the other one is the latent heat (expressed as $\dot{l}$):

$$\psi_{z_i} \cdot \dot{z}_i = \dot{e}_{\mathrm{M},i} + \dot{l}. \tag{5.11}$$

$\dot{e}_{\mathrm{M},i}$ is the difference in the mechanical energy between the two sides of A-M interface. By using Eq. (4.7) and (5.11), $\dot{e}_{\mathrm{M},i}$ can be written as:

$$\dot{e}_{\mathrm{M},i} = \boldsymbol{\sigma}_i : \dot{\boldsymbol{\varepsilon}}_{\mathrm{ori},i} - D - \dot{l}. \tag{5.12}$$

Integrating this equation for an ideal SMA with the behavior given in Figure 5.6 and for a monotonic loading path, $e_{\mathrm{M},i}$ can be given by the following equation:

$$e_{\mathrm{M},i} = \sigma_{\text{A-M}} \cdot \varepsilon_{\mathrm{ori},i} - D_{\mathrm{forward}} - l, \tag{5.13}$$

where $\sigma_{\text{A-M}}$ is the yield stress for forward phase transformation, austenite A → martensite M, and D_{forward} is the dissipation generated during forward phase transformation. In Eq. (5.13), $\varepsilon_{\mathrm{ori},i}$ and l are constants. Furthermore, the mechanical dissipation is generated during both forward and reverse phase transformations, thus the value of D_{forward} is lower than the total dissipation in one complete cycle (expressed here as D_{cycle}):

$$D_{\mathrm{forward}} < D_{\mathrm{cycle}} = \sigma_{\text{A-M}} \cdot \varepsilon_{\mathrm{ori},i} - \sigma_{\text{M-A}} \cdot \varepsilon_{\mathrm{ori},i}, \tag{5.14}$$

where $\sigma_{\text{M-A}}$ is the yield stress for reverse phase transformation. Considering that $\sigma_{\text{M-A}}$ is an increasing function of temperature (see Figure 5.6, when temperature increases, $T_1 \rightarrow T_2$, austenite becomes more stable and higher stresses are needed for both forward and reverse phase transformations); based on Eq. (5.13) and inequality (5.14), we have

$$\boldsymbol{\sigma}^*_{\mathrm{max},i} \propto e_{\mathrm{M},i} > \sigma_{\text{M-A}}(T_{\mathrm{front}}) \cdot \varepsilon_{\mathrm{ori},i} - l, \tag{5.15}$$

where l is independent of temperature[1]. Eq. (5.15) illustrates that an increase in temperature will result in a higher value of the energy jump in A-M interface and therefore a higher level of TRIP. Consequently, the temperature can be used as an indicator to evaluate $\boldsymbol{\sigma}^*_{\mathrm{max}}$ which governs fatigue crack initiation in SMAs. As a consequence, *the temperature during phase transformation can be used as an indicator to predict low-cycle fatigue of SMAs*: at higher temperature, austenite becomes more stable and stress-induced transformation becomes more difficult, leading to a higher energy jump and therefore to a higher local stress in A-M interface.

---

[1] The value of the latent heat is proportional to the saturated temperature amplitude (He and Sun, 2010a; Yin et al., 2014), as it will be shown experimentally in the next section, the temperature amplitude (due to the latent heat) does not increase when the temperature level rises.

Consequently, the local plasticity is accelerated and the fatigue lifetime shortens.

5.3 Experimental validation

In this section, the material and the experimental setup are first described. Then, the dependence of TRIP on temperature is experimentally validated. Finally, the proposed model is used to provide a quantitative assessment of low-cycle fatigue of SMAs.

5.3.1 Experiment

In order to validate the dependence of the TRIP on temperature, as shown in Figure 5.7, static loading-unloading tests are carried out: NiTi wires were subjected to tensile loading making sure that the phase transformation was complete ($z = 1$, in this case according to Eq. (5.7), $\boldsymbol{\varepsilon}^{\mathrm{p}} = \boldsymbol{E}^{\mathrm{p}}$) and then unloaded to zero. The frequency of this one-cycle test was 5×10^{-3} Hz (in such low frequency the effect of thermomechanical coupling on the material response is limited). An environment control chamber was used to control the temperature during the tests. Three different temperatures were tested with 40 ± 2°C, 52 ± 2°C, 65 ± 2°C respectively.

Low cycle fatigue tests results are taken from chapter 2.

5.3.2 Dependence of TRIP on temperature

Figure 5.8 shows the results of quasi-static loading-unloading test of SMA wires and clearly confirms that TRIP increases with temperature following a quasi-linear relation (phase transformation is complete; in the case of $z = 1$, $\boldsymbol{E}^{\mathrm{p}} = \boldsymbol{\varepsilon}^{\mathrm{p}}$). According to equation (5.9) the increase of TRIP will result in a higher magnitude of $\boldsymbol{\sigma}^{*}_{\mathrm{max}}$. Furthermore, a quasi-linear character in the relation between TRIP $\boldsymbol{\varepsilon}^{\mathrm{p}}$ ($\boldsymbol{E}^{\mathrm{p}}$) and temperature T holds also in the relation between $\boldsymbol{\sigma}^{*}_{\mathrm{max}}$ and T.

5.3.3 Maximum temperature as fatigue indicator

It is well known that in the case of high frequency, heat transfer is not sufficient to remove the heat generated inside the material to the surroundings. As a consequence, an oscillation of temperature occurs upon cycling. As shown in Figure 5.9, forward phase transformation takes place and propagates as Lüders-like martensite bands. Furthermore, TRIP is triggered in A-M interfaces within the martensite bands and the temperature of the material increases significantly

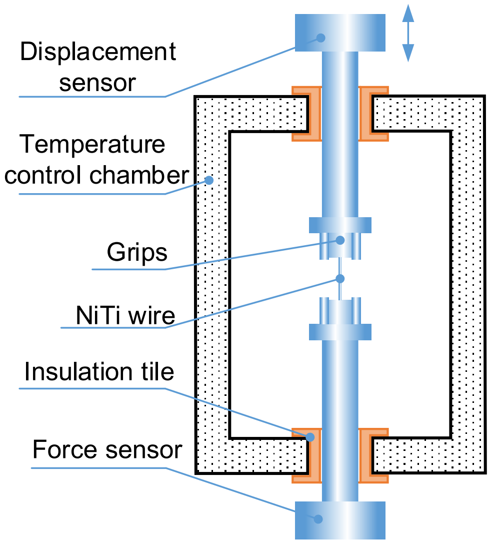

Figure 5.7 Experimental setup

as a result of accumulation of the heat generated during forward phase transformation[1]; the temperature of the material reaches its maximum value at the end of the forward phase transformation (i.e. when the phase transformation is complete or just before the unloading process). Hence, material points within martensite band front at the end of the forward phase transformation have the highest temperatures and therefore A-M interfaces here undergo highest value of $\boldsymbol{\sigma}^*_{\max}$ as indicated by Eq. (5.15). As a consequence, the maximum temperature during the whole cycle can be used as an indicator to predict low-cycle fatigue of SMAs. This statement will be validated experimentally in the next paragraphs where all thermal and mechanical responses correspond to stabilized cycles of tests.

Figure 5.10 and Figure 5.11 display mechanical and thermal responses for different frequencies under strain-controlled loading; 0-4.61% and 0-6.58% respectively[2]. Due to thermomechanical coupling, when the frequency increases, the temperature of the material increases. As a consequence, according to Eq. (5.9) and (5.15), $\boldsymbol{\sigma}^*_{\max}$ increases and accelerates crack initiation resulting in a decrease of fatigue lifetime (see Figure 5.12). Fatigue lifetime and maximum temperature for all strain-controlled results are plotted in Figure 5.13 where a quasi-linear evolution is shown. This indicates the direct relation between the maximum temperature and the fatigue lifetime confirming that the maximum temperature is a relevant indicator to predict low-cycle fatigue of SMAs.

Figure 5.14 displays the mechanical and thermal response under stress-controlled loading

---

[1] Although, the temperature distribution is not homogeneous, the heat conduction can increase the mean temperature in the material even in regions where phase transformation has not been activated.

[2] For the sake of a relevant comparison of the phase transformation plateaus, the relative strain (total strain minus the residual strain) of the stabilized cycle is used.

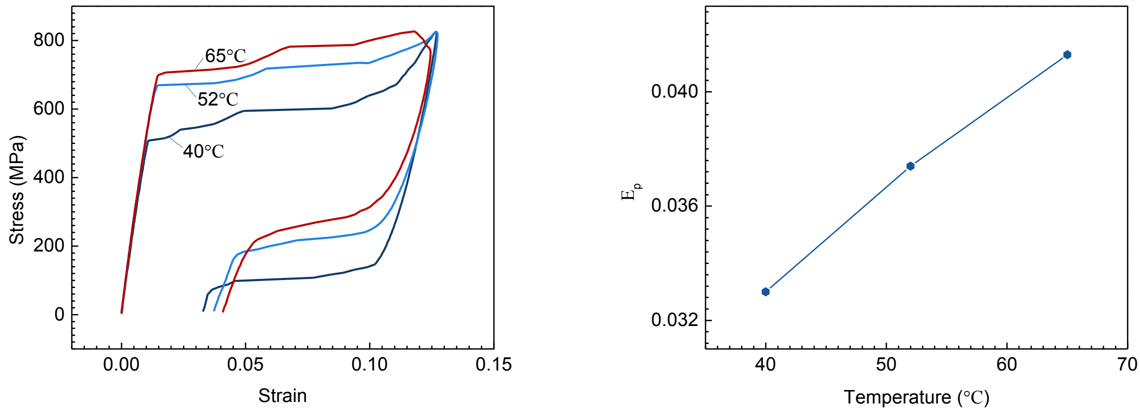

Figure 5.8 The experimental evidence of the dependence of TRIP on temperature : the results of quasi-static tests of SMA wires at 40°C, 52°C, 65°C respectively, where the phase transformation is completed ($z = 1$), in this case according to Eq.(5.7), $\boldsymbol{\varepsilon}^{\mathrm{p}} = \boldsymbol{E}^{\mathrm{p}}$.

with the amplitude 0-637.0 MPa (in the case of such high stress level, phase transformations are completed for all frequencies). The same phenomena as in the case of strain-controlled loadings are observed (Figure 5.15): an increase in frequency results in a rise of the maximum temperature and on a reduction of the fatigue lifetime. A quasi-linear relation between the fatigue lifetime and the maximum temperature is also obtained, as shown in Figure 5.16.

The results under stress controlled loading with the lower amplitude, 0-471.3 MPa, are quite different from the case of the high stress-controlled loading: fatigue lifetime for low amplitude is quasi-constant when the frequency changes. The difference between the two cases shown in Figure 5.14 and 5.17 depends on whether the phase transformation is complete ($z = 1$) or not : for the 0-637.0 MPa loading, phase transformations are complete for all frequencies; however, for the 0-471.3 MPa loading, triggering phase transformation is reduced with increasing frequency. This can be explained by thermomechanical coupling: when the frequency is high, the mean temperature of the material rises and leads to an increase in yield stress of forward phase transformation. Hence, since the maximum stress is fixed in the case of stress-controlled loading, the same amplitude of the applied stress triggers more phase transformation at low frequency than at high frequency, resulting in an incomplete phase transformation. Furthermore, less phase transformation being triggered means that less latent heat is released, as a result, the temperature amplitude in the stress controlled loading decreases with the frequency [temperature amplitude of SMAs is driven by the release/absorption of latent heat, (He and Sun, 2010b; Yin et al., 2014)]. Consequently, unlike the results under strain controlled, or under stress controlled loading with high amplitude (0-637.0 MPa), the maximum temperature of the material does not increase monotonically with the frequency in the case of loading with amplitude 0-471.3 MPa; in fact, it almost stays unchanged (see Figure

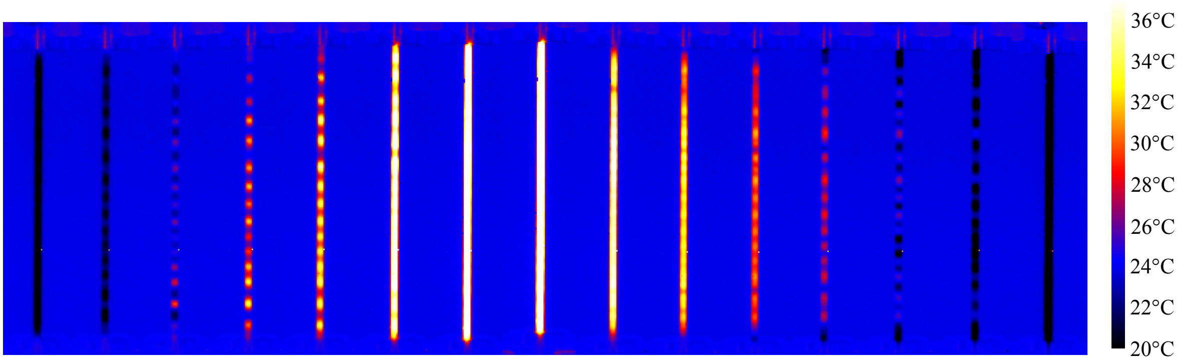

Figure 5.9 Infrared photos of a NiTi wire during one complete cycle: strain control 0-4.61%, 0.3Hz, where the temperature distribution is non-uniform because phase transformation always appears as a local phenomenon, i.e., Lüders-like transformation in SMAs. The temperature of the material reaches its maximum value at the end of the forward phase transformation

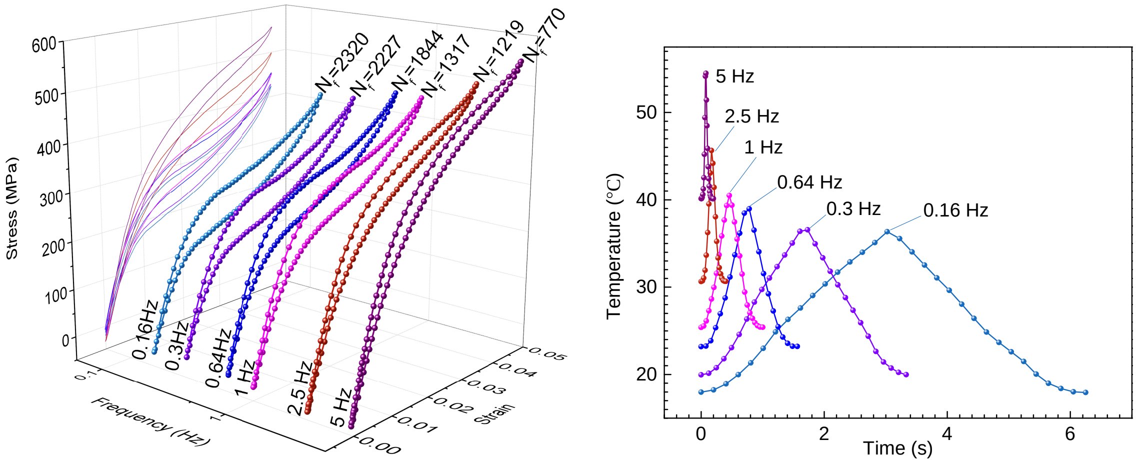

Figure 5.10 Stress-strain, fatigue lifetime and temperature evolutions under strain controlled loading: 0-4.61%. For the sake of a relevant comparison of the phase transformation plateaus, the relative strain of the stabilized cycle is used. N_f is the fatigue lifetime. The maximum temperature increases with the frequency and the fatigue lifetime decreases.

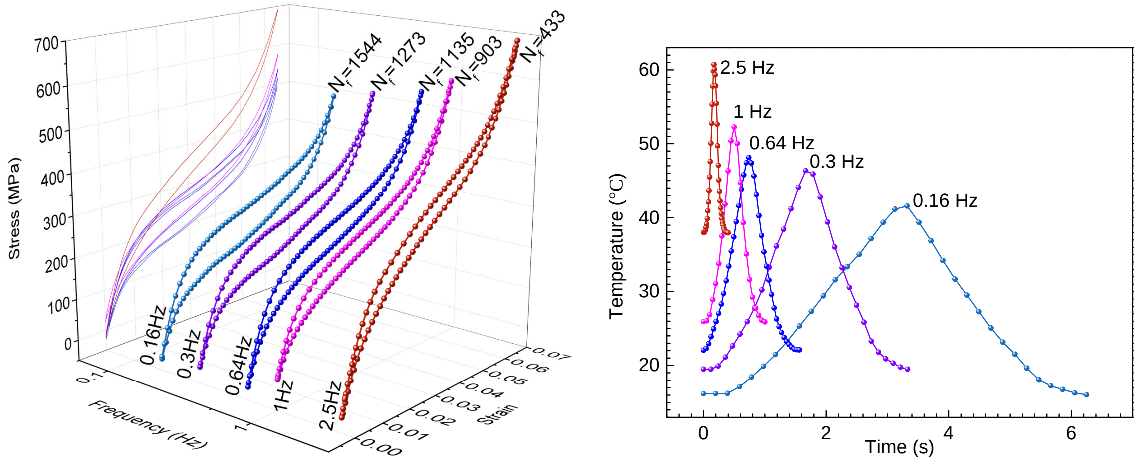

Figure 5.11 Stress-strain, fatigue lifetimes and temperature evolutions under strain-controlled loading: 0-6.58%.

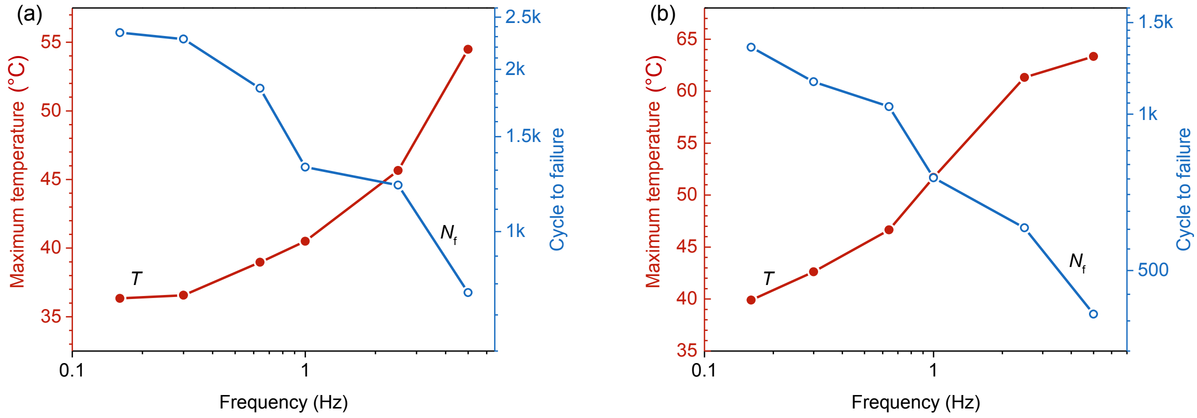

Figure 5.12 Evolution of the maximum temperature and fatigue lifetime with loading frequency for different strain amplitudes: (a) 0-4.61%; (b) 0-6.58%. For both cases, the maximum temperature increases with the frequency and the fatigue lifetime decreases.

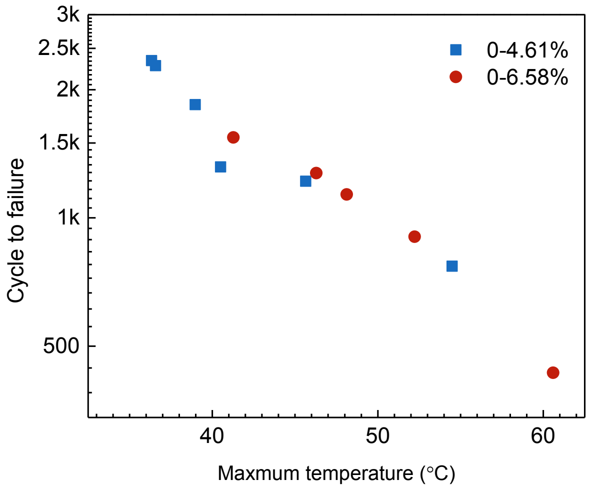

Figure 5.13 Number of cycles to failure versus maximum temperature under strain controlled loading. Fatigue lifetime is a quasi-linear decreasing function of the maximum temperature.

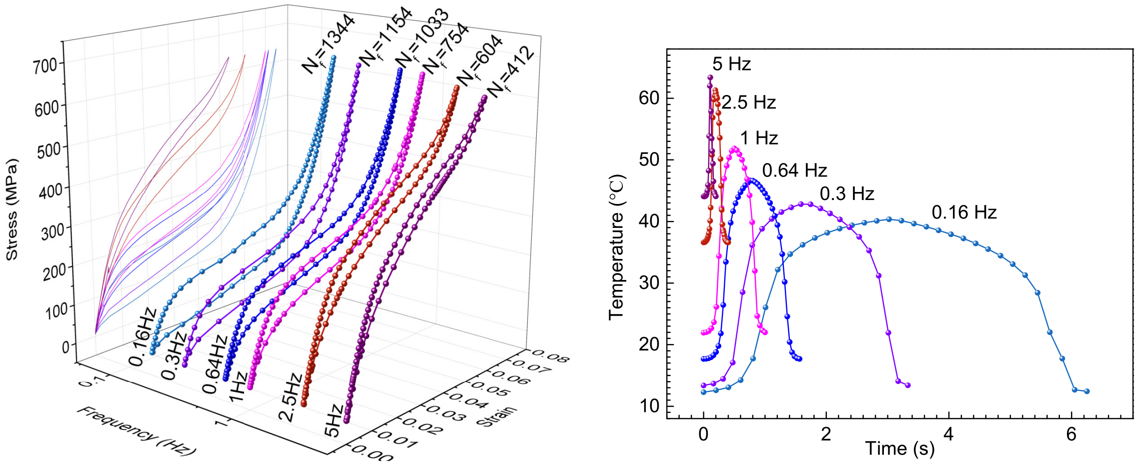

Figure 5.14 Stress-strain, fatigue lifetime and temperature evolutions under stress controlled loading (0-637.0 MPa). In the case of such high stress level, phase transformations are completed for all frequencies; as a result, a tendency similar to the case of strain-controlled loading is observed.

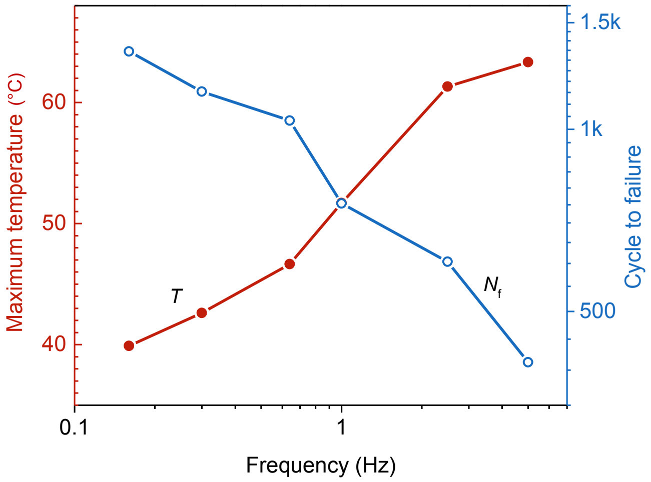

Figure 5.15 Evolution of the maximum temperature ($T_{\max}$) and number of cycles to failure (N_f) with loading frequency under stress controlled loading (0-637.0 MPa); a tendency similar to the case of strain-controlled loading is observed: with increasing the frequency, maximum temperature increases and fatigue lifetime reduces.

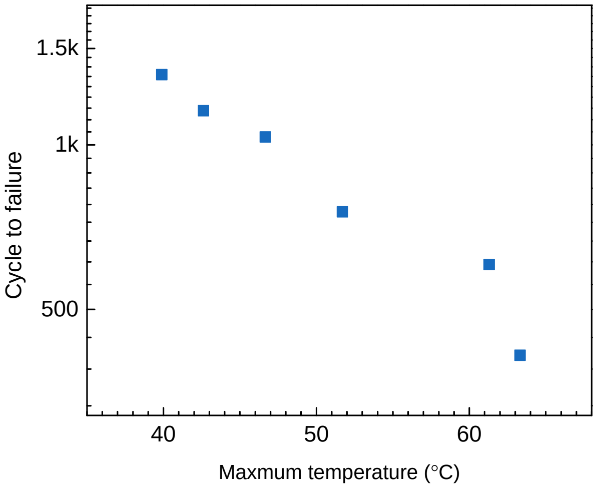

Figure 5.16 Number of cycles to failure (N_f) versus the maximum temperature ($T_{\max}$) under high-amplitude stress controlled loading (0-637 MPa). Fatigue lifetime is a quasi-linear decreasing function of the maximum temperature.

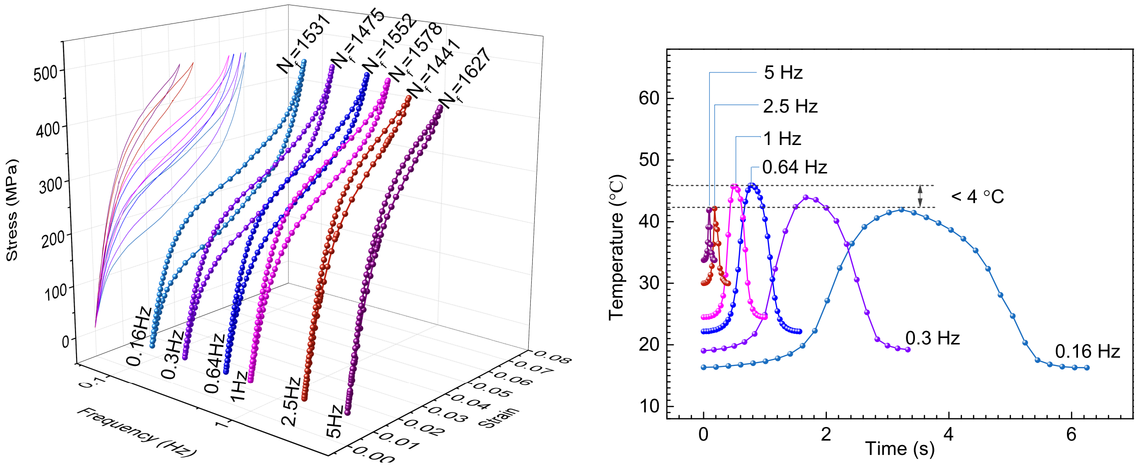

Figure 5.17 Stress-strain, fatigue lives and temperature evolutions under stress controlled loading (0-471.3 MPa). Since the maximum stress is fixed, phase transformation is reduced with increasing frequency at mid-stress level; less latent heat is released, and the temperature decreases.The maximum temperature of the material does not increase monotonically with the frequency.

5.17, where the maximum variation of temperature amplitudes for all frequencies is 4 °C. When compared to Figure 5.14 where the difference in the maximum temperature reaches 25°C, the changes in maximum temperatures in the case of 0-471.3 MPa can be neglected). In summary, for the case of low stress amplitude, the maximum temperature doesn't change with frequency and so is the fatigue lifetime. This is a further evidence that the maximum temperature is the relevant indicator to predict low-cycle fatigue of SMAs.

In all tests, carried out in this work, the values of fatigue lifetime N_f are plotted versus maximum temperature $T_{\max}$ are plotted using a logarithmic scale in Figure 5.18a for strain and stress -controlled loadings at different amplitudes and different frequencies; all results lie on a quasi-linear curve. Hence, the number of cycle to failure can be expressed as a function of the maximum temperature as follows:

$$N_f = \mu T_{\max}^{k}, \tag{5.16}$$

where μ and k are material parameters; for the material studied in this work, $\mu = 1.4521 \times 10^8$ $^\circ C^{-1}$, k=-3.0673 providing a new low-cycle fatigue criterion for SMAs. The error analysis is performed in Figure 5.18b, where experimental fatigue lifetime correlates very well with the predictions of the criterion. The analysis above confirms that the maximum temperature at the stabilized cycle is the relevant parameter to predict low-cycle fatigue of SMAs. In real applications, the maximum temperatures can be calculated by solving thermomechanically coupled equations [see the work proposed in He and Sun (2010b)], or by numerical simulations (Zhang et al., 2017). This criterion clearly shows that improving the thermomechanical conditions (optimizing the shape/size of the structures and the heat transfer conditions) to

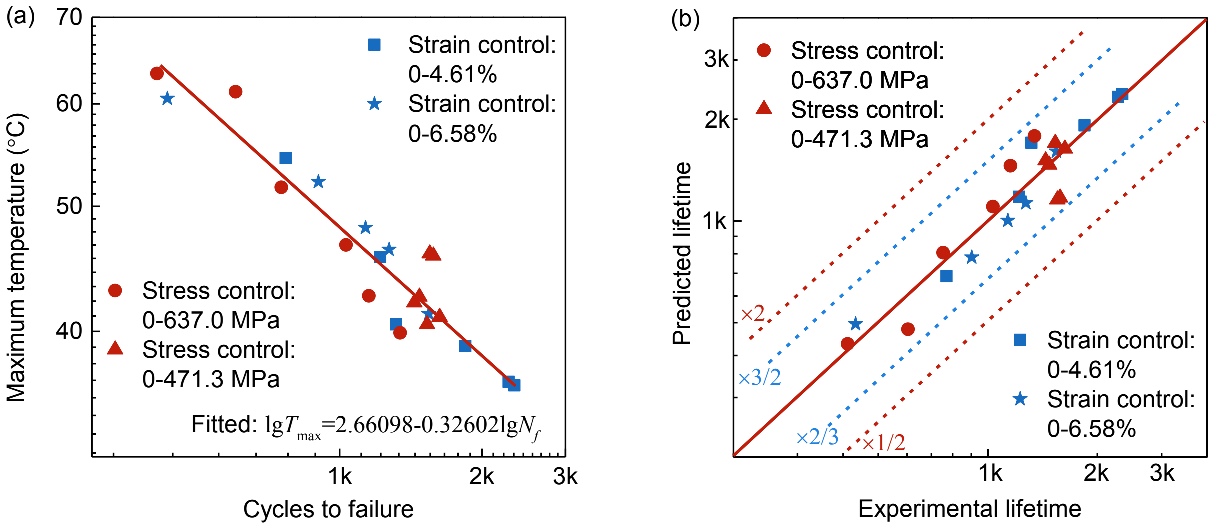

Figure 5.18 Fatigue model: (a) number of cycles to failure versus maximum temperature; (b) error analysis.

reduce the local temperature will enhance the low cycle fatigue property of an SMA structure in which case, the local plasticity will be weakened and therefore the fatigue lifetime will be extended.

5.4 Discussions

In this paragraph, the implication of the previous result, namely the fact that the maximum temperature $T_{\max}$ is the fatigue indicator, on fatigue of SMAs will be discussed. In fact, this statement raises two relevant questions:

- First, it has been shown that the local stress peak $\sigma^*_{\max}$ that occurs on local phase interface controls the fatigue behavior of SMAs via maximum temperature. In this case, can we conclude that fatigue lifetime of shape memory alloys is independent of the mechanical external load ?
- Second, according to the model presented here, fatigue cracks should nucleate at material points at A-M interfaces which undergo the highest temperature change. Then, is it the reason that fatigue failure usually occurs on one of the martensite fronts as has been reported recently in the literature (Sedmák et al., 2016; Zheng et al., 2017; Zhang and He, 2017)?

5.4.1 Response to question 1

The dependence of low-cycle fatigue of SMAs on macroscopic mechanical loads

Figure 5.19 presents an ideal SMA subjected to three loading paths under ideal isothermal condition: (i) OBCDEO, (ii) OBFGEO and (iii) OBHIEO. According to the TRIP-based model presented here, the fatigue lifetimes of these three loading paths should be identical. In fact, as it has been indicated in section 5.2, a larger strain amplitude only means a larger expansion of the phase transformation regions. Hence, although in (i) the macro-strain amplitude is the smallest, its corresponding fatigue lifetime is the same as the two other loading paths, (ii) and (iii), because the fatigue lifetime is only influenced by the local TRIP which always reaches the same level under isothermal condition.

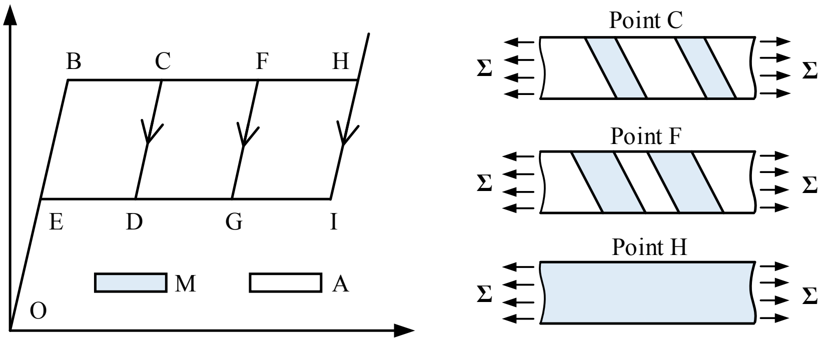

Figure 5.19 Different loading paths for an ideal SMA under ideal isothermal conditions.

Similarly, although the macroscopic response of a real SMA is affected by the dislocation induced internal stresses and temperature (thermomechanical coupling), fatigue lifetime is still driven by the local TRIP in the phase transformation regions. The maximum temperature reaching the same value indicates that the local triggered TRIP has the same level as well. As predicted and validated experimentally by the model presented, the fatigue lifetime will be the same under different mechanical loads. Hence, the dependence of low cycle fatigue in real SMAs on the macroscopic mechanical loads can be addressed as follows:

Isothermal condition:

The quasi-static isothermal condition can be obtained by applying a mechanical loading at an extremely small loading rate. For our analysis in this case, we use the results of low-cycle fatigue tests of NiTi plates in air at room temperature as proposed by Zheng et al. (2016b). (N_f is around 200 cycles). As shown in Figure 5.20, the NiTi plates were tested to failure at a strain rate of 10^{-4} s $^{-1}$ under three types of strain controlled loading paths with 1.5%, 1.25% and 1% amplitudes respectively. Although the macro applied loads are different, fatigue lifetimes range

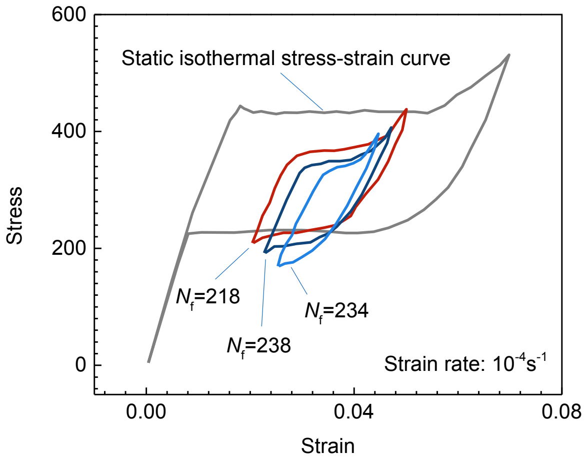

Figure 5.20 The fatigue test results of polycrystalline NiTi shape memory alloys at quasi-static isothermal condition: strain controlled loading with the amplitudes 1.5%, 1.25%, 1% and 0.75% respectively (Zheng et al., 2016b).

within the same level for the three loadings paths confirming the predictions of the TRIP-based model.

Non-isothermal condition with the same maximum temperature:

SMAs in real applications always show strong thermomechanical coupling, the temperature of the material is governed by mechanical loading and heat transfer. As a consequence, it is possible to tune test parameters (heat transfer conditions, loading rate or ambient temperature) in order to reach the same maximum temperature at different mechanical loading and amplitudes.

Figure 5.17 shows fatigue lifetime results at different macro-strains and the same maximum temperature. These tests were performed at a fixed applied stress (stress control: 0-471.3 MPa), the difference in strain amplitudes is a result of thermomechanical coupling. The results show again that fatigue lifetimes are quite identical for all tests.

Finally, four additional tests were conducted under different applied loads (different amplitude and different loading types) for which the loading frequencies were adjusted to reach the same maximum temperature : (1) stress controlled loading, 0-471.3 MPa, 2.5 Hz, (2) strain controlled loading, 0-4.61%, 1 Hz, (3) stress controlled loading, 0-522.3 MPa, 0.16 Hz, (4) stress controlled loading 0-637.0 MPa, 0.16 Hz. The results are plotted in Figure 5.21: for the same maximum temperature $T_{\max}$, the variation of temperature is less than 2 °C, the fatigue lifetime N_f lies within the same level.

Comparison with classical criteria

All the results shown above confirm the prediction of the TRIP-based model: in the pseudo-elastic domain, if the maximum temperature is kept constant fatigue lifetime remains unchanged

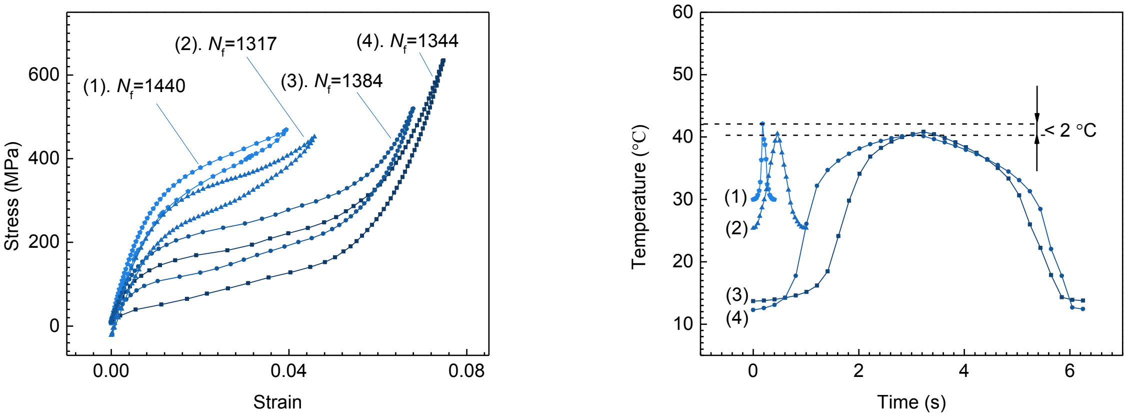

Figure 5.21 The results obtained under different mechanical loads but with the same fatigue lifetime: (1) stress controlled loading, 0-471.3 MPa, 2.5 Hz; (2) strain controlled loading, 0-4.61%, 1 Hz; (3) stress controlled loading, 0-522.3 MPa, 0.16 Hz; (4) stress controlled loading, 0-637.0 MPa, 0.16 Hz.

whatever the mechanical loads and the frequency.

However, in the literature on fatigue of SMAs, the macro mechanical response is usually used to predict the fatigue lifetime (Moumni et al., 2005; Maletta et al., 2012, 2014; Song et al., 2015a,b,c; Zhang et al., 2016). In fact, the model presented here doesn't not contradict the classical criteria in the sense that the temperature is not independent of the applied mechanical load. The key difference resides on whether the thermomechanical coupling is taken into account or not: when the heat transfer conditions are unchanged (no need to consider the thermomechanical coupling), the higher is the amplitude of the applied load (stress or strain controlled) the shorter is the fatigue lifetime (for example, see Figure 5.22 when the frequency is fixed, a higher loading amplitude induces more phase transformation and consequently results in more heat inside the material causing a higher temperature and lower fatigue lifetime). However, when thermomechanical coupling is considered, the temperature of the material is not only function of the mechanical load, but it is also strongly affected by the heat transfer conditions (e.g., the loading frequency). In that case, the macroscopic response is no longer suitable to predict fatigue lifetime of SMAs. Figure 5.23 presents two isotherms in mechanical load amplitude-frequency diagram; all points belonging to the isotherm present the same fatigue lifetime; only when the loading frequency is fixed, the macroscopic mechanical response is directly correlated with the fatigue lifetime of the SMA.

5.4.2 Response to question 2: location of the fatigue cracks initiation

As it has been analyzed in section 3.3, the material points within the martensite band front at the end of the forward phase transformation undergo the highest temperature change and

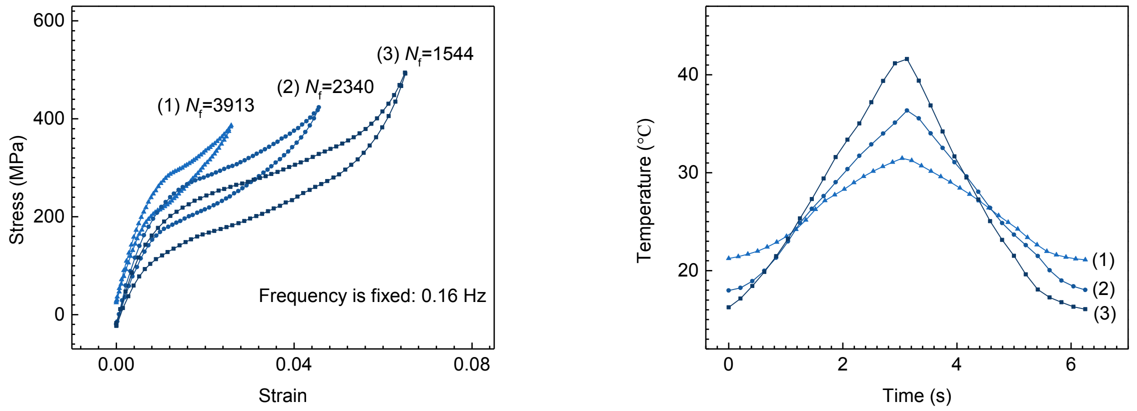

Figure 5.22 The results obtained under fixed frequency 0.16 Hz: strain controlled loading with amplitudes (1) 0-2.63%; (2) 0-4.61%; (3)0-6.58%.

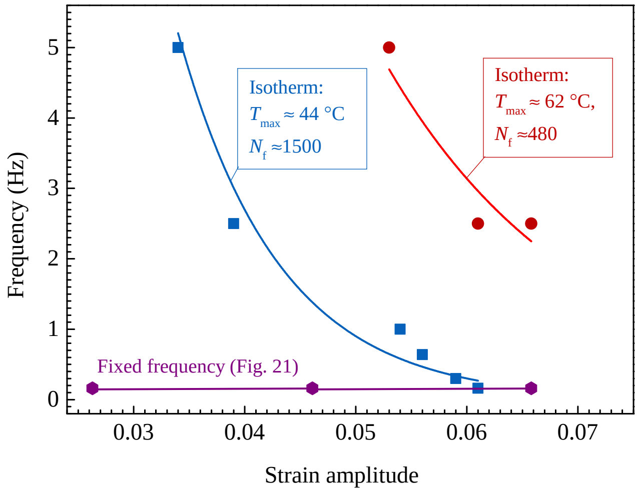

Figure 5.23 Isotherms in mechanical load amplitude-frequency diagram: all points belonging to the isotherm present the same fatigue lifetime; only when the frequency is fixed, the macroscopic mechanical response is directly correlated with the fatigue lifetime of SMAs.

therefore the A-M interfaces here have the highest $\sigma^*_{\max}$. After few cycles, when the stabilized state is reached, the martensite bands reach a stabilized pattern as shown in (Zheng et al., 2017). Hence, it is expected that fatigue cracks initiate on martensite fronts at the end of the forward phase transformation. As show in Figure 5.24, due to the accumulation of the heat generated during forward phase transformation, the temperature of the material increases and finally reaches the maximum level in the martensitic region at time t_4. As a result, the fatigue failure will have the highest probability to occur on one of the martensite fronts (indicated by arrows in Figure 5.24f). Particularly, if two martensite fronts merge in a local region at time t_4, the fatigue crack can also initiate at this merging interface (indicated by an arrow in Figure 5.24g).

In our tests, fatigue failure occurs within the “fracture region“ as indicated in Figure 5.24d; however, it is quite difficult to clearly distinguish the martensite fronts in a SMA wire. For this reason, we used the results of Zheng et al. (2017) to validate our prediction; the evolution of martensite bands and position of the fatigue failure crack of NiTi SMA plates were observed

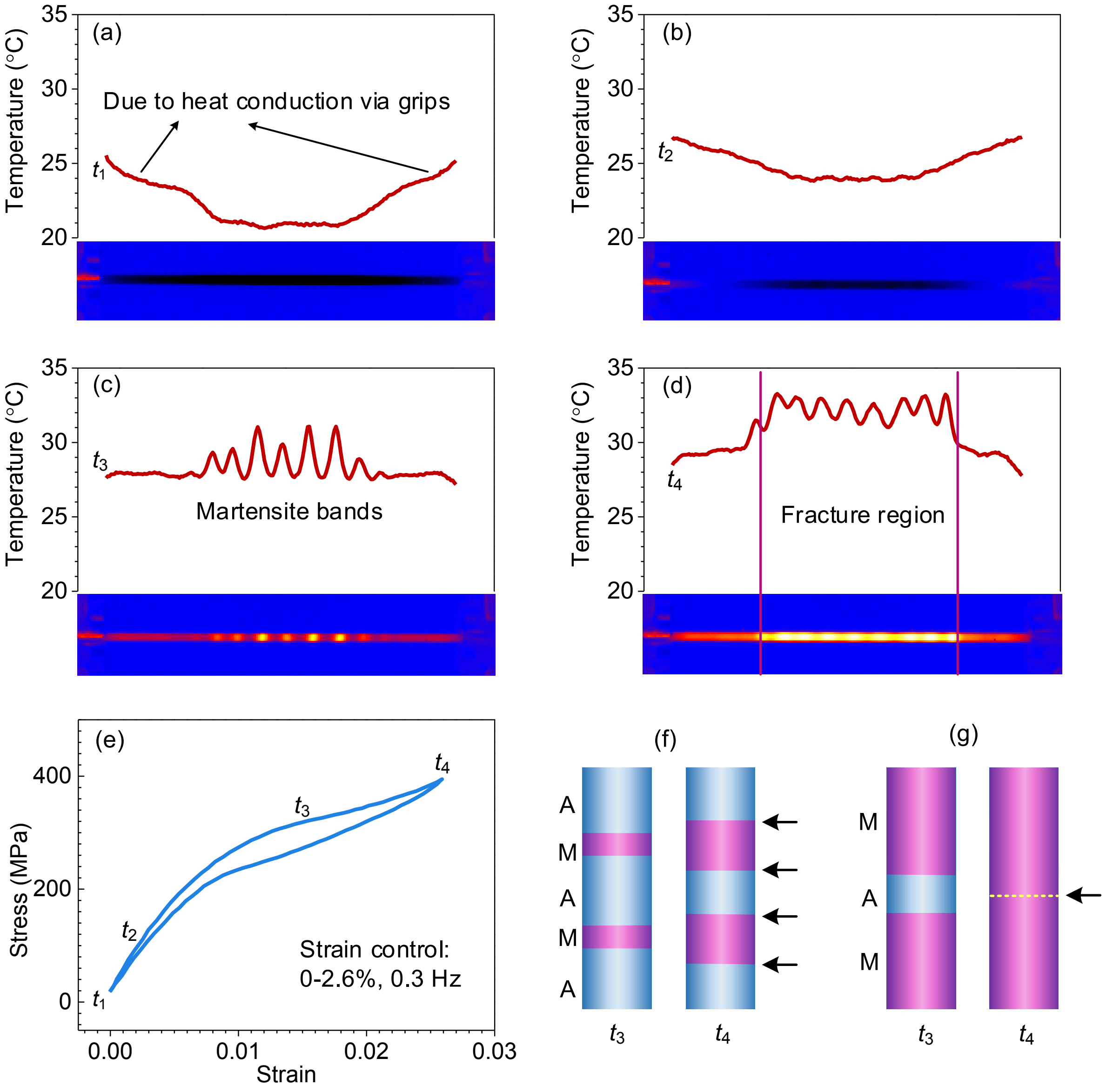

Figure 5.24 Schematic of the fatigue fracture position: (a)-(d) the evolution of temperature distribution along the SMA wire during forward phase transformation; (e) the corresponding global stress-strain curve. At time t_4 (end of the forward phase transformation), the temperature of the SMA reaches its maximum level; fatigue crack initiates at (indicated by arrows) (f) one of the martensite fronts or (g) the interface in which two martensite fronts merge.

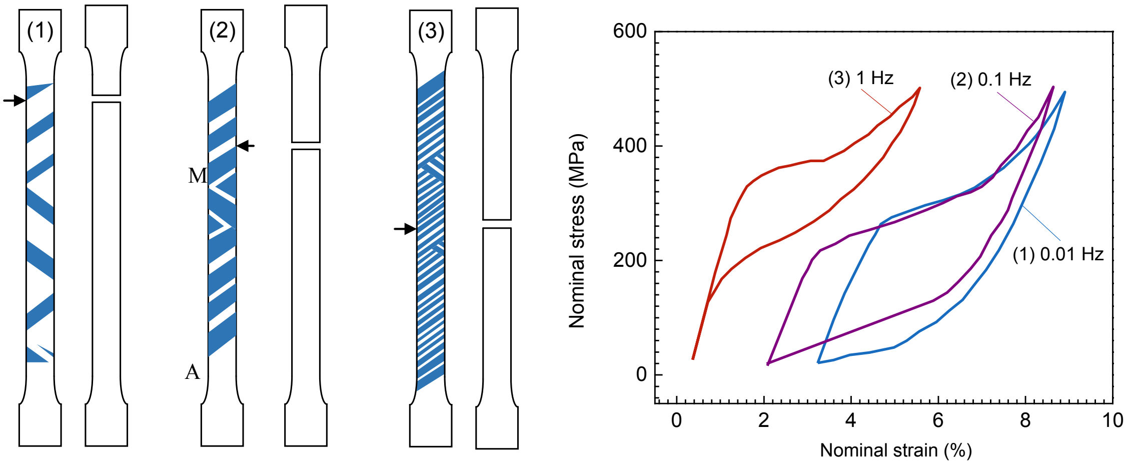

(a) In-situ optical observed results

(b) Nominal stress-strain curves

Figure 5.25 Fatigue test results of NiTi plates, obtained from Zheng et al. (2017): (a) in-situ optical observed results; (b) corresponding nominal stress-strain curves, where the arrow in each figure indicates the initiation position of the fatigue failure crack and all results correspond to the moment the forward phase transformation ends (i.e., the maximum temperature) at the stabilized state (50 cycles):

by using in-situ optical method. As shown in Figure 5.25, the crack initiation position is close to one of the macro-band fronts of the "steady-state" cycle (in Figure 5.25, the distribution of martensite bands corresponds to the end of the forward phase transformation at the stabilized cycle, and the position of the initiation of the fatigue failure crack is indicated by an arrow). As expected, all fatigue cracks initiate on one of the martensite fronts at the end of the forward phase transformation.

5.5 Conclusions

In this chapter, a TRIP-based model for low-cycle fatigue of SMAs is proposed and then experimentally validated. During stress-induced phase transformation, TRIP is triggered as a result of high local stresses induced by the unmatched deformation in A-M interfaces. However, due to hardening, upon cyclic loading slip deformation becomes more difficult to be triggered and a locally stabilized state is reached characterized by the saturation of the TRIP and by a maximum local stress in A-M interface $\boldsymbol{\sigma}^*_{\max}$. In other words, when the stabilized state is reached, dislocation slips accumulate to a saturated level and become potential crack sources. During subsequent fatigue loading, material points at transformed regions are swept over by a steady stress peak ($\boldsymbol{\sigma}^*_{\max}$) following the forth and back movement of A-M interface until the initiation of fatigue cracks from these potential crack sources. Based on modelling and experimental results, a new low-cycle fatigue criterion is developed and some relevant issues relative to low-cycle fatigue of SMAs are discussed. Key conclusions of this study are:

- Local TRIP (evaluated by $T_{\max}$) drives the fatigue of SMAs. Once forward phase transformation takes place, a mechanical energy jump in A-M interface occurs. Due to this energy jump, material points in A-M interface undergo plastic flow to accommodate deformation incompatibilities and redistribute the energy between the two sides of the interface. An increase in temperature increases this energy jump and thus accelerates TRIP (i.e., higher value of $\boldsymbol{\sigma}^*_{\max}$). At the end of the forward phase transformation, the temperature of the SMA reaches its maximum value, and material points in the corresponding A-M interfaces undergo the highest stress peak $\boldsymbol{\sigma}^*_{\max}$. Consequently, the maximum temperature during the whole cycle can be used as the indicator for low cycle fatigue of SMAs.

- The external mechanical load drives the forward phase transformation, during which mechanical dissipation is generated and latent heat is released. The temperature of the SMA is determined together by the mechanical load and the heat transfer condition: when thermomechanical loads increase the maximum temperature of the material, the fatigue lifetime decreases; for different thermomechanical loads for which the maximum temperature reaches the same level, fatigue lifetimes stay at the same level even though the amplitudes of macroscopic mechanical loads are different. If and only if the heat transfer conditions are fixed (e.g., the same loading frequency) that macroscopic mechanical loads can be directly linked to the fatigue of SMAs, because in this case the maximum temperature is a function of mechanical loads: higher mechanical loads result in more phase transformation and in more heat inside the material, leading to a higher value of maximum temperature.

- The material points within the martensite band front at the end of the forward phase transformation have the highest temperature and therefore A-M interfaces have the highest value of $\boldsymbol{\sigma}^*_{\max}$, triggering highest level local plasticity. As a result, fatigue failure always occurs at one of the martensite fronts (or the merging interface of two martensite fronts) at the end of the forward phase transformation.

Chapter 6

Effect of the training stress on fatigue lifetime of SMAs

This chapter presents a mechanical training process that allows enhancing resistance to low cycle fatigue of shape memory alloys. To this end, three training stresses were tested (0-509.6 MPa, 0-637.0 MPa, 0-764.3 MPa); for each case, NiTi wires were first subjected to the corresponding load during first 20 cycles, and then tested to failure under strain-controlled fatigue loading. Results show that fatigue lifetime is training-dependent in the sense that specimens with higher training stresses present a better fatigue lifetime. Indeed, for sufficiently high training stress, fatigue lifetime can be 10 times extended.

6.1 Introduction

Chapters 2-5 clearly show that phase transformation plateau, which is affected by temperature and indicates the magnitude of strain energy and stored energy, significantly affects the low cycle fatigue lifetime of SMAs. As has discussed in chapter 5, when subjected to cyclic pseudoelastic loading, SMAs present residual deformations mainly due to TRIP. Hence, dislocations are created and result in a residual internal stress field. This residual stress can assist the nucleation of martensite variants and therefore lower the stress plateau during forward transformation. Considering that SMAs always need to be trained for several cycles in order to stabilize their mechanical behavior before being utilized for practical applications, it is of most importance to analyze the influence of the amplitude of the training load on the phase transformation stresses as well as the fatigue lifetime of SMAs. It has been experimentally shown that large pre-strains significantly reduce the fatigue lifetime of Nitinol wires during the fully reversed rotary bending fatigue tests which induces both tensile and compressive residual stresses (Gupta et al., 2015).

However, their results are obtained by bending-rotation tests; the detailed mechanism of the influence of the uniaxial tensile (or compressive) residual stresses fields introduced by the training loads on the fatigue lifetime of SMAs is still unclear.

6.2 Experimental results and discussion

The same material and experiment setup in chapter 2 are used to study the effect of the training stress on low cycle fatigue of SMAs. The tests were classified into three groups according to the amplitudes of the training stresses during first 20 cycles (0.04 Hz; stress control): *Case* I: 0-509.6 MPa, *Case* II: 0-637.0 MPa and *Case* III: 0-764.3 MPa; the specimens in each group were subsequently submitted to the same fatigue loading (0.2 Hz, strain control, $\varepsilon_{\min} = 0$, $\varepsilon_{\max}$ ranging from 2.5% to 6.1%) until failure. Each test was repeated at least twice.

Figure 6.1 gives the results of $\varepsilon - N$ curves for each of the three groups and clearly shows that the fatigue lifetime of SMAs is strongly dependent on the training stress:

- Larger amplitude of the training stress during the first 20 cycles obviously extends the fatigue lifetime of SMAs. The lowest lifetime corresponds to *Case* I, for which the training stress during first 20 cycles is not high enough to complete the phase transformation. When the training stress is sufficiently high to complete the phase transformation, fatigue lifetime increases (*Case* II); the longest lifetime is obtained in *Case* III, in which the SMA wire is overloaded after the phase transformation being completed. For the sake of clarity, this effect hereinafter is referred to as *training stress effect*.

- *Training stress effect* depends on the amplitude of the subsequent fatigue loading. The *training stress effect* is significant when the strain amplitude of the subsequent fatigue loading is small (see Figure 6.1; for the minimum strain amplitude 0-2.5%, the fatigue lifetime in *Case* III increases by more than 10 times compared to *Case* I). When the strain amplitude of the fatigue load increases, the *training stress effect* weakens and nearly vanishes when the strain amplitude reaches 0-6.1%.

Figure 6.2 provides the explanation of how the residual internal stress field assists the forward phase transformation in a material RVE (Representative Volume Element) in which $\boldsymbol{\Sigma}$ and $\boldsymbol{E}$ are macroscopic stress and strain, $\boldsymbol{\sigma}$ and $\boldsymbol{\varepsilon}$ are the corresponding local responses at mesoscopic scale: according to TRIP theory, dislocations are created during forward phase transformation and when the applied load is completely removed, dislocations remain and result in a residual internal stress field $\boldsymbol{\sigma}_r$. During subsequent cycles, the internal stress, which is of the same kind of the applied stress as pointed out by (Miyazaki et al., 1986), assists

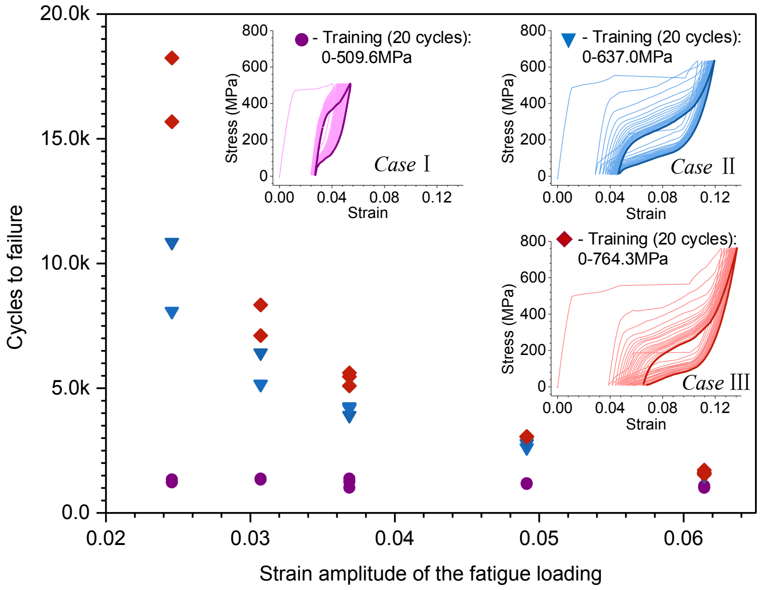

Figure 6.1 $N - \varepsilon$ curves, loading ratio = 0; $0 \leftrightarrow \varepsilon_{\mathrm{max}}$.

the nucleation of martensite variants, leading to a significant reduction in the yield stress required to trigger the forward phase transformation (Figure 6.2b). As a consequence, the yield transformation surface shrinks during subsequent cycles (Miyazaki et al., 1986; Zaki and Moumni, 2007a). In region A (Figure 6.2a; close to the dislocations), the amplitude of the local residual stress is high and therefore a reduction in the yield stress of the phase transformation occurs. Furthermore, the residual stress field has a gradient in its strength (Miyazaki et al., 1986; Yawny et al., 2005; Yu et al., 2015a) in such a way that when the phase transformation propagates from region A to region B the amplitude of the internal stress reduces (see Figure 6.2b, the magnitude of $\boldsymbol{\sigma}_r^{\mathrm{A}}$ is larger than the magnitude of $\boldsymbol{\sigma}_r^{\mathrm{B}}$). As a consequence, in order to continue the forward phase transformation, the macro stress must be increased (see Figure 6.2c) resulting in a higher slope of phase transformation plateau. Furthermore, since the fatigue loading is strain-controlled, the macro stress-strain response of the trained SMAs necessary lies under the response of the virgin SMAs. In fact, since the phase transformation is triggered at lower yield stress, it induces a macroscopic stress relaxation phenomena resulting in a reduction of the amplitude of the fatigue stresses and an increase of the fatigue lifetime.

As shown above, the residual local stress ($\boldsymbol{\sigma}_r$) field plays an important role in the fatigue of SMAs. Due to the complicated micro-structure, it is very difficult to evaluate it at the mesoscopic scale. Nevertheless, if one considers the RVE as a structure (Figure 6.2a), it is clear that a higher amplitude of the macroscopic stress $\Delta(\boldsymbol{\Sigma})$ will result in a lower fatigue lifetime (Eggeler et al., 2004; Nayan et al., 2008). Furthermore, tensile pre-deformation creates compressive residual stresses on the surface of polycrystalline SMA samples (Gupta et al., 2015;

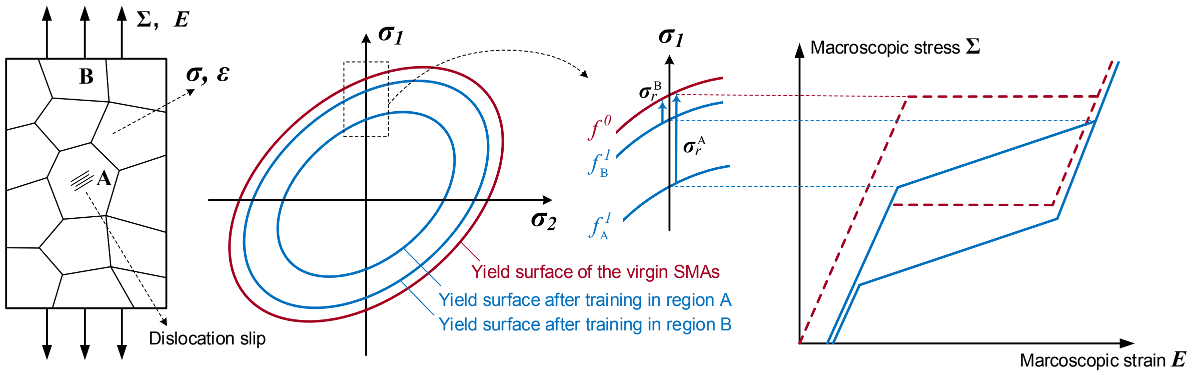
Σ, E
B
A
σ, ε
Dislocation slip
σ1
σ2
Yield surface of the virgin SMAs
Yield surface after training in region A
Yield surface after training in region B
σ1
σ_r^B
σ_r^A
f^0
f_B^1
f_A^1
Macroscopic stress Σ
Marcoscopic strain E

(a) Dislocations (b) Local yield surface of phase transformation after training (c) Macroscopic stress-strain response after training

Figure 6.2 The residual stress induced by dislocation slip can assist the phase transformation, where $\boldsymbol{\Sigma}$ and $\boldsymbol{E}$ are macro stress and strain; $\boldsymbol{\sigma}$ and $\boldsymbol{\varepsilon}$ are the corresponding local responses; $\boldsymbol{\sigma}_r^{\mathrm{A}}$ and $\boldsymbol{\sigma}_r^{\mathrm{B}}$ are local residual internal stresses in region A and region B respectively, f^0 is the yield surface of the virgin SMA and f_{A}^1 and f_{B}^1 are yield surfaces during a subsequent cycle corresponding to region A and region B respectively.

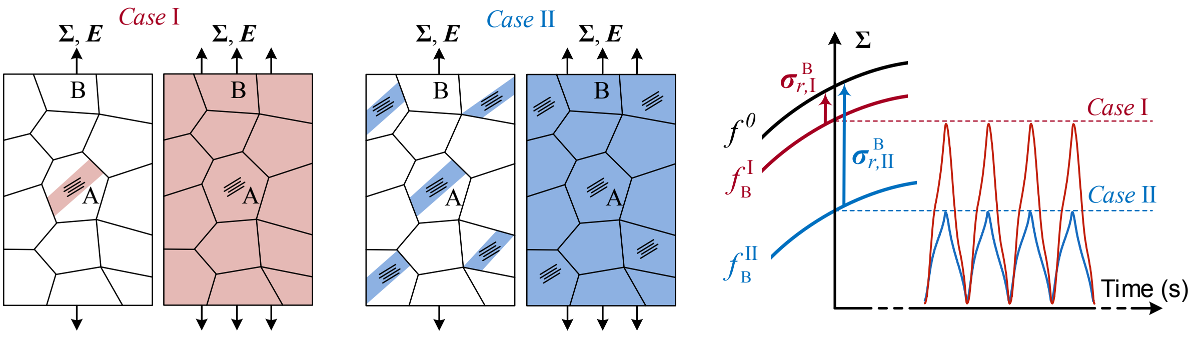
Case I
Σ, E
Σ, E
B
A
Case II
Σ, E
Σ, E
B
A
Σ
σ_{r,I}^B
σ_{r,II}^B
f^0
f_B^I
f_B^II
Case I
Case II
Time (s)

Figure 6.3 Schematic of the influence of the training stress on the stress required to trigger the same fraction of phase transformation during subsequent fatigue loadings, where $\boldsymbol{\sigma}_{r,\mathrm{I}}^{\mathrm{B}}$ and $\boldsymbol{\sigma}_{r,\mathrm{II}}^{\mathrm{B}}$ are the internal stresses after training in *Case* I and *Case* II respectively (both in region B); the cyclic stress responses versus time correspond the fatigue loading 0-2.5%: *Case* I in red and *Case* II in blue.

Paranjape et al., 2017), which naturally improve the subsequent fatigue resistance because the crack opening is prevented.

The previous analysis allow to give a physical interpretation of the *training stress effect* as follows : as shown in Figure 6.1, from *Case* I to *Case* III, the higher TRIP is triggered in the training step, the more dislocations remain after unloading (see Figure 6.1). As a consequence the residual strain after the training process increases from *Case* I to *Case* III. Figure 6.3 gives a schematic comparison between the stresses required to trigger the same fraction of phase transformation in *Case* I and *Case* II during the subsequent fatigue loading. For both cases, the maximum internal residual stresses occur in the region where dislocation slip occurs. Hence, the forward phase transformation is first triggered in the very close

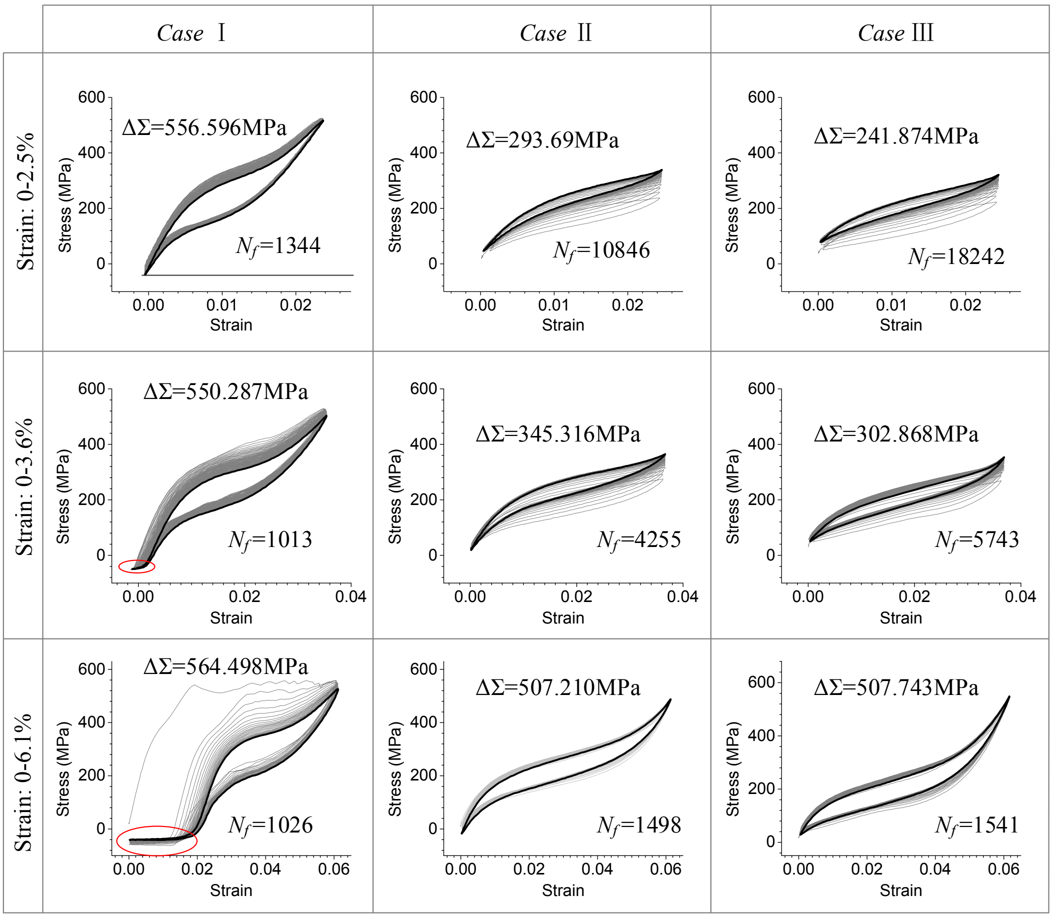

Figure 6.4 Stabilization of stress-strain curves during subsequent fatigue loadings, where N_f is the corresponding fatigue lifetime. The red circle indicates the residual strain due to the buckling of the wire; if this buckling can be avoided, the fatigue lifetime is expected to decrease because the SMA wires will be further tensioned.

neighbourhood of dislocations and then propagates until the whole RVE is transformed. For *Case* I, few dislocations remain after training and thus far from dislocations (region B) the local residual internal stress, expressed as $\boldsymbol{\sigma}^{\mathrm{B}}_{r,\mathrm{I}}$, is small (or equals zero); in such cases, a high level macroscopic stress $\boldsymbol{\Sigma}$ is required to trigger the phase transformation in this region and to complete the phase transformation of the RVE. In *Case* II, much more dislocations remain after training inducing higher and more homogeneous local internal residual stress field. As a consequence, the macroscopic stress required to complete phase transformation of the RVE is much lower than in *Case* I because the dislocation induced residual stress in region B ($\boldsymbol{\sigma}^{\mathrm{B}}_{r,\mathrm{II}}$) is also high since the dislocations distribution is more homogeneous. As a consequence the fatigue lifetime in *Case* II is higher than in *Case* I. This tendency is confirmed in *Case* III where TRIP is the highest (the material is overloaded after phase transformation), thus the greatest number of dislocations occur and therefore the residual internal stress field reaches its highest magnitude. Consequently, the macro stress required for the phase transformation falls down to a minimum value resulting in the highest fatigue lifetime. Figure 6.4 compares the amplitudes of the macro stress between three groups: the maximum fatigue stress $\Delta\Sigma$ occurs in *Case* I. As a consequence, the fatigue lifetime is the shortest in this case. It is worthy to note that this beneficial effect of the amplitude of the training stress decreases with the amplitude of the fatigue loading. In fact, for a high-amplitude fatigue loading (e.g. strain amplitude 0-6.1%), the fatigue loading itself induces a great number of dislocations during first fatigue few cycles which mitigates the effect of the gradient of the local internal stresses due to the training process. As a consequence, the *training stress effect* decreases with the amplitude of fatigue loading.

6.3 Conclusion

In conclusion, low cycle fatigue resistance of NiTi shape memory alloys can be improved by applying a large-amplitude training stress during first few cycles: large-amplitude training stress during first few cycles produces dislocation-induced local residual stress field. During subsequent strain-controlled fatigue loading, this residual stress can assist the phase transformation and thus reduces the yield stress of phase transformation as well as the amplitude of the macroscopic applied stress. As a consequence, the fatigue lifetime increases. This result is very valuable for SMA applications, especially for the situations in which the fatigue loading is not very high. For example, in the present study, for a strain controlled fatigue loading with an amplitude of 0-2.5%, the fatigue lifetime has been be extended by more than 10 times.

Chapter 7

Conclusion and future work

7.1 Conclusion

This thesis proposed a comprehensive investigation of low cycle fatigue of shape memory alloys. Main conclusions are summarized in following aspects:

7.1.1 Thermomechanical coupling in low cycle fatigue behaviors

Thermomechanical coupling in low cycle fatigue of SMAs is due to two aspects: frequency dependence and loading mode dependence. Under strain controlled loading, almost equal amount of phase transformation for all the frequencies leads to an equal amount of austenite-martensite and martensite-martensite interfaces that are potential crack sources. An increase in temperature level makes the austenite more stable, and increases the stress associated with the A-M interfaces. Hence, the crack initiation is accelerated and the fatigue lifetime decreases. Under stress control, the fatigue lifetime is influenced by a combined effect of reduction in the potential crack sources and an increase in the driving stress. For a relatively low stress level, fatigue lifetime is dominated by the reduction in the potential crack sources; for high stress level, the evolution of fatigue lifetime is controlled by the increase in the driving stress, and for intermediate stress level, the two effects can balance each other, as a consequence, the fatigue lifetime becomes frequency independent.

From energy point of view, during pseudoelastic deformation, the hysteresis work is partially dissipated into heat. The remainder, the so-called stored energy, in part accumulates in dislocations, and in part is stored as internal energy in residual martensite variants. The stored energy is the key factor to predict the fatigue of SMAs, and its magnitude depends on dislocations and residual martensite variants densities and increases with the temperature of the material. For strain controlled loading, the phase transformation is triggered up to the same level for all the frequencies because the deformation amplitude is fixed; higher loading frequencies cause an increase in temperature. As a result, the stored energy increases and shorten the fatigue lifetime; for stress controlled loading, an increase in mean temperature of the material sometimes cause a reduction in phase transformation, accompanied with a reduction of the temperature amplitude as well as the potential source of dislocations or residual martensite, which can reduce the stored energy. Consequently, the fatigue lifetime, that is determined by the stored energy, shows a maximum stress-dependent trend.

7.1.2 Crack initiation

During stress-induced phase transformation, TRIP is triggered due to high local stresses produced by the unmatched deformation in A-M interfaces and will get saturated (the SMA reaches the stabilized state) after few cycles, with the local stress in A-M interface reaching the maximum. When the stabilized state is reached, dislocation slips accumulate to a saturated level and can be regarded as the potential crack sources and the cyclic stress peak in A-M interface the driving force. Under this cyclic stress peak, the fatigue crack finally initiates from these potential crack sources.

An increase in temperature makes the energy jump in A-M interface more significant and thus accelerates more TRIP. At the end of the forward phase transformation, the temperature of SMAs reaches its maximum value, which means that material points in corresponding A-M interfaces undergo the highest stress peak. Consequently, the maximum temperature during the whole cycle can be used as the indicator for low cycle fatigue of SMAs, and low cycle fatigue of SMAs is not directly correlated with the mechanical loads applied at macro-scale within the range of phase transformation and below the plastic yield. The material points in A-M interfaces at the end of the forward phase transformation undergo the highest temperature and therefore the highest value of stress peak, as a result, fatigue failure always occurs at one of the martensite fronts (or the merging interface of two martensite fronts) at the end of forward phase transformation.

7.1.3 Fatigue criteria

Three fatigue criteria for SMAs are proposed and validated in this work; results show that the total strain energy, stored energy as well as the maximum temperature can be used individually to predict the fatigue lifetime of SMAs including thermomechanical coupling. In fact, these three responses are not independent and they can be correlated with each other as summarized below:

- Stored energy can be correlated to the stabilized strain energy [Eq. (4.63) of chapter 4.4]. As discussed in chapter 4.4, the stored-energy-based criterion provide the physical foundation of the strain-energy-based criterion.
- Stored energy is strongly affected by the temperature of the material. When temperature rises, the austenite becomes more stable and therefore higher energy is needed to keep the material points stay in residual martensite state. As a result, the accumulation of the stored energy increases and cause a reduction in fatigue lifetime (see Figure 4.13 of chapter 4.4).
- Since the macroscopic stress plateau strongly depends on the temperature, the same correlation also holds between the maximum temperature and the total strain energy.

The maximum temperature-based based criterion has a theoretical highest accuracy since it is directly linked to the fatigue crack initiation; it applies to all the loading types. However, its application is limited by the measurement of temperature, which is complex and always introduce large errors. For the energy-based criteria, the stored-energy-based one has higher accuracy, however, the strain energy based one has a larger variety of applications because it does not need to record the residual strain during stabilization.

7.1.4 Improvement of low cycle fatigue performance

Low cycle fatigue lifetime of SMAs is training-dependent; it can be improved by applying a large-amplitude training stress during first few cycles: large-amplitude training stress produces dislocation-induced local residual stress field. During subsequent strain-controlled fatigue loading, this residual stress can assist the phase transformation and thus reduces the yield stress of phase transformation as well as the amplitude of the macroscopic applied stress. As a consequence, the fatigue lifetime is extended.

7.2 Future work

In this work, though some theoretical explanations have been proposed based on the mesoscopic considerations, a further understanding of low cycle fatigue of SMAs is still limited due to the lack of microscopic experimental evidence. Hence, experimental investigations at mesoscopic and microscopic scale are strongly required in the future work. For instance, a measurement of dislocations and residual martensite variants during cyclic loading will offer an opportunity to calculate the internal stress field and the local stored energy density, which can be directly correlated to the fatigue of SMAs.

Furthermore, this work will be also continued in aerospace industry. Thanks to the rapid development of the unmanned system and 3D printing technology, SMAs now becomes a potential candidate for some major structures (e.g., morphing wing of an unmanned aerial vehicle) as well as complex smart structures. The design and optimization of these SMA structures against fatigue will be an interesting and challenging issue.

Bibliography

Anahid, M. and Ghosh, S. (2013). Homogenized constitutive and fatigue nucleation models from crystal plasticity fe simulations of ti alloys, part 2: Macroscopic probabilistic crack nucleation model. *International Journal of Plasticity*, 48:111 – 124.

Anand, L., Gurtin, M. E., and Reddy, B. D. (2015). The stored energy of cold work, thermal annealing, and other thermodynamic issues in single crystal plasticity at small length scales. *Int. J. Plast.*, 64:1 – 25.

Benafan, O., Noebe, R., Padula, S., Garg, A., Clausen, B., Vogel, S., and Vaidyanathan, R. (2013). Temperature dependent deformation of the B2 austenite phase of a NiTi shape memory alloy. *International Journal of Plasticity*, 51:103 – 121.

Benke, M. and Mertinger, V. (2014). In situ optical microscope study of the thermally induced displacive transformations in cualni-based shape-memory alloys. *Journal of Materials Engineering and Performance*, 23(7):2333–2338.

Benzerga, A., Bréchet, Y., Needleman, A., and Van der Giessen, E. (2005). The stored energy of cold work: Predictions from discrete dislocation plasticity. *Acta Mater.*, 53(18):4765–4779.

Berry, M. and Garcia, E. (2008). Bio-inspired shape memory alloy actuated hexapod robot. In *Active and Passive Smart Structures and Integrated Systems 2008*, volume 6928, page 69281M. International Society for Optics and Photonics.

Brinson, L. C., Schmidt, I., and Lammering, R. (2004). Stress-induced transformation behavior of a polycrystalline niti shape memory alloy: micro and macromechanical investigations via in situ optical microscopy. *J. Mech. Phys. Solids*, 52(7):1549–1571.

Buehler, W. J., Gilfrich, J., and Wiley, R. (1963). Effect of low-temperature phase changes on the mechanical properties of alloys near composition tini. *Journal of applied physics*, 34(5):1475–1477.

Bundhoo, V., Haslam, E., Birch, B., and Park, E. J. (2009). A shape memory alloy-based tendon-driven actuation system for biomimetic artificial fingers, part i: design and evaluation. *Robotica*, 27(1):131–146.

Calhoun, C., Wheeler, R., Baxevanis, T., and Lagoudas, D. (2015). Actuation fatigue life prediction of shape memory alloys under the constant-stress loading condition. *Scripta Materialia*, 95:58 – 61.

Carlo, M. and Metin, S. (2006). A biomimetic climbing robot based on the gecko. *Journal of Bionic Engineering*, 3(3):115 – 125.

Chatziathanasiou, D., Chemisky, Y., Chatzigeorgiou, G., and Meraghni, F. (2016). Modeling of coupled phase transformation and reorientation in shape memory alloys under non-proportional thermomechanical loading. *Int. J. Plast.*, 82:192 – 224.

Chen, B., Jiang, J., and Dunne, F. P. (2017). Is stored energy density the primary meso-scale mechanistic driver for fatigue crack nucleation? *International Journal of Plasticity*.

Cho, K.-J., Hawkes, E., Quinn, C., and Wood, R. J. (2008). Design, fabrication and analysis of a body-caudal fin propulsion system for a microrobotic fish. In *Robotics and Automation, 2008. ICRA 2008. IEEE International Conference on*, pages 706–711. IEEE.

Chowdhury, P. and Sehitoglu, H. (2017). A revisit to atomistic rationale for slip in shape memory alloys. *Progress in Materials Science*, 85:1–42.

Chrysochoos, A., Maisonneuve, O., Martin, G., Caumon, H., and Chezeaux, J. (1989). Plastic and dissipated work and stored energy. *Nucl. Eng. Des.*, 114(3):323–333.

Cisse, C., Zaki, W., and Zineb, T. B. (2016). A review of constitutive models and modeling techniques for shape memory alloys. *International Journal of Plasticity*, 76(Supplement C):244 – 284.

Cocco, V. D., Iacoviello, F., Natali, S., Volpe, V., and Maiolino, F. (2014). Fatigue crack propagation micromechanisms in a cu-zn-al alloy with pseudoelastic effect. *Procedia Materials Science*, 3:363 – 368. 20th European Conference on Fracture.

Condó, A., Lovey, F., Olbricht, J., Somsen, C., and Yawny, A. (2008). Microstructural aspects related to pseudoelastic cycling in ultra fine grained ni–ti. *Materials Science and Engineering: A*, 481-482(Supplement C):138 – 141. Proceedings of the 7th European Symposium on Martensitic Transformations, ESOMAT 2006.

Cuniberti, A. and Romero, R. (2004). Differential scanning calorimetry study of deformed cuznal martensite. *Scripta Mater*, 51:315–320.

Daly, S., Ravichandran, G., and Bhattacharya, K. (2007). Stress-induced martensitic phase transformation in thin sheets of nitinol. *Acta Materialia*, 55(10):3593 – 3600.

Delville, R., Malard, B., Pilch, J., Sittner, P., and Schryvers, D. (2011). Transmission electron microscopy investigation of dislocation slip during superelastic cycling of ni–ti wires. *International Journal of Plasticity*, 27(2):282 – 297.

DesRoches, R. and Delemont, M. (2002). Seismic retrofit of simply supported bridges using shape memory alloys. *Engineering Structures*, 24(3):325 – 332.

Dunand-Châtellet, C. and Moumni, Z. (2012). Experimental analysis of the fatigue of shape memory alloys through power-law statistics. *Int. J. Fatigue*, 36(1):163 – 170.

Dunne, F., Wilkinson, A., and Allen, R. (2007). Experimental and computational studies of low cycle fatigue crack nucleation in a polycrystal. *International Journal of Plasticity*, 23(2):273 – 295.

Eggeler, G., Hornbogen, E., Yawny, a., Heckmann, a., and Wagner, M. (2004). Structural and functional fatigue of NiTi shape memory alloys. *Mater. Sci. Eng. A*, 378(1-2):24–33.

Entemeyer, D., Patoor, E., Eberhardt, A., and Berveiller, M. (2000). Strain rate sensitivity in superelasticity. *Int. J. Plast.*, 16:1269–1288.

Feng, P. and Sun, Q. (2006). Experimental investigation on macroscopic domain formation and evolution in polycrystalline niti microtubing under mechanical force. *Journal of the Mechanics and Physics of Solids*, 54(8):1568 – 1603.

Figueiredo, A. M., Modenesi, P., and Buono, V. (2009). Low-cycle fatigue life of superelastic niti wires. *International Journal of Fatigue*, 31(4):751 – 758.

Frotscher, M., Nörtershäuser, P., Somsen, C., Neuking, K., Böckmann, R., and Eggeler, G. (2009). Microstructure and structural fatigue of ultra-fine grained niti-stents. *Materials Science and Engineering: A*, 503(1):96 – 98. International Symposium on Bulk Nanostructured Materials: from Fundamentals to Innovation, BNM 2007.

Gall, K. and Maier, H. (2002). Cyclic deformation mechanisms in precipitated niti shape memory alloys. *Acta Materialia*, 50(18):4643 – 4657.

Gandhi, F. and Wolons, D. (1999). Characterization of the pseudoelastic damping behavior of shape memory alloy wires using complex modulus. *Smart Mater. Struct.*, 8(1):49–56.

Gloanec, A.-L., Bilotta, G., and Gerland, M. (2013). Deformation mechanisms in a tini shape memory alloy during cyclic loading. *Materials Science and Engineering: A*, 564(Supplement C):351 – 358.

Grabe, C. and Bruhns, O. (2008). On the viscous and strain rate dependent behavior of polycrystalline NiTi. *Int. J. Solids Struct.*, 45(7-8):1876–1895.

Gu, X., Zhang, W., Zaki, W., and Moumni, Z. (2017). An extended thermomechanically coupled 3d rate-dependent model for pseudoelastic smas under cyclic loading. *Smart Materials and Structures*, 26(9):095047.

Gupta, S., Pelton, A. R., Weaver, J. D., Gong, X.-Y., and Nagaraja, S. (2015). High compressive pre-strains reduce the bending fatigue life of nitinol wire. *Journal of the Mechanical Behavior of Biomedical Materials*, 44:96 – 108.

Hallai, J. F. and Kyriakides, S. (2013). Underlying material response for lüders-like instabilities. *International Journal of Plasticity*, 47(Supplement C):1 – 12.

Hamilton, R., Sehitoglu, H., Efstathiou, C., Maier, H., Chumlyakov, Y., and Zhang, X. (2005). Transformation of co–ni–al single crystals in tension. *Scripta Mater.*, 53(1):131 – 136.

Hartl, D. J., Lagoudas, D. C., Calkins, F. T., and Mabe, J. H. (2010a). Use of a ni60ti shape memory alloy for active jet engine chevron application: I. thermomechanical characterization. *Smart Materials and Structures*, 19(1):015020.

Hartl, D. J., Mooney, J. T., Lagoudas, D. C., Calkins, F. T., and Mabe, J. H. (2010b). Use of a ni60ti shape memory alloy for active jet engine chevron application: Ii. experimentally validated numerical analysis. *Smart Materials and Structures*, 19(1):015021.

He, Y. and Sun, Q. (2010a). Rate-dependent domain spacing in a stretched niti strip. *International Journal of Solids and Structures*, 47(20):2775 – 2783.

He, Y. J. and Sun, Q. P. (2010b). Frequency-dependent temperature evolution in NiTi shape memory alloy under cyclic loading. *Smart Mater. Struct.*, 19(11):115014.

He, Y. J. and Sun, Q. P. (2011). On non-monotonic rate dependence of stress hysteresis of superelastic shape memory alloy bars. *Int. J. Solids Struct.*, 48:1688–1695.

Hodowany, J., Ravichandran, G., Rosakis, a., and Rosakis, P. (2000). Partition of plastic work into heat and stored energy in metals. *Exp. Mech.*, 40(2):113–123.

Hornbogen, E. (2004). Review thermo-mechanical fatigue of shape memory alloys. *J. Mater. Sci.*, 39(2):385–399.

Iadicola, M. A. and Shaw, J. A. (2002). The effect of uniaxial cyclic deformation on the evolution of phase transformation fronts in pseudoelastic niti wire. *Journal of Intelligent Material Systems and Structures*, 13(2-3):143–155.

Iadicola, M. A. and Shaw, J. A. (2004). Rate and thermal sensitivities of unstable transformation behavior in a shape memory alloy. *International Journal of Plasticity*, 20(4):577 – 605.

Jani, J. M., Leary, M., Subic, A., and Gibson, M. A. (2014). A review of shape memory alloy research, applications and opportunities. *Materials & Design (1980-2015)*, 56(Supplement C):1078 – 1113.

Kamlah, M. and Haupt, P. (1997). On the Macroscopic Description of Stored Energy and Self Heating During Plastic Deformation. *Int. J. Plast.*, 13(10):893–911.

Kan, Q. and Kang, G. (2010). Constitutive model for uniaxial transformation ratchetting of super-elastic niti shape memory alloy at room temperature. *Int. J. Plast.*, 26(3):441 – 465.

Kan, Q., Kang, G., Yan, W., Dong, Y., and Yu, C. (2012). An energy-based fatigue failure model for super-elastic niti alloys under pure mechanical cyclic loading. In *Third International Conference on Smart Materials and Nanotechnology in Engineering*, volume 8409, page 84090F. International Society for Optics and Photonics.

Kan, Q., Yu, C., Kang, G., Li, J., and Yan, W. (2016). Mechanics of Materials Experimental observations on rate-dependent cyclic deformation of super-elastic NiTi shape memory alloy. *Mech. Mater.*, 97:48–58.

Kang, G., Kan, Q., Qian, L., and Liu, Y. (2009). Ratchetting deformation of super-elastic and shape-memory niti alloys. *Mechanics of Materials*, 41(2):139 – 153.

Kato, H. and Sasaki, K. (2013). Transformation-induced plasticity as the origin of serrated flow in an niti shape memory alloy. *Int. J. Plast.*, 50:37 – 48.

Kheirikhah, M. M., Rabiee, S., and Edalat, M. E. (2011). A review of shape memory alloy actuators in robotics. In Ruiz-del Solar, J., Chown, E., and Plöger, P. G., editors, *RoboCup 2010: Robot Soccer World Cup XIV*, pages 206–217, Berlin, Heidelberg. Springer Berlin Heidelberg.

Koster, M., Lee, W., Schwarzenberger, M., and Leinenbach, C. (2015). Cyclic deformation and structural fatigue behavior of an fe–mn–si shape memory alloy. *Materials Science and Engineering: A*, 637:29 – 39.

Kundin, J., Pogorelov, E., and Emmerich, H. (2015). Numerical investigation of the interaction between the martensitic transformation front and the plastic strain in austenite. *Journal of the Mechanics and Physics of Solids*, 76:65 – 83.

Lagoudas, D., Hartl, D., Chemisky, Y., Machado, L., and Popov, P. (2012). Constitutive model for the numerical analysis of phase transformation in polycrystalline shape memory alloys. *International Journal of Plasticity*, 32-33(Supplement C):155 – 183.

Lagoudas, D. C. (2008). *Shape memory alloys: modeling and engineering applications*. Springer Science & Business Media.

Lagoudas, D. C., Miller, D. A., Rong, L., and Kumar, P. K. (2009). Thermomechanical fatigue of shape memory alloys. *Smart Materials and Structures*, 18(8):085021.

Laster, Z., MacBean, A., Ayliffe, P., and Newlands, L. (2001). Fixation of a frontozygomatic fracture with a shape-memory staple. *The British journal of oral & maxillofacial surgery*, 39(4):324.

Lubarda, V. A. (2016). On the recoverable and dissipative parts of higher order stresses in strain gradient plasticity. *Int. J. Plast.*, 78:26 – 43.

Maletta, C., Sgambitterra, E., Furgiuele, F., Casati, R., and Tuissi, A. (2012). Fatigue of pseudoelastic niti within the stress-induced transformation regime: a modified coffin–manson approach. *Smart Materials and Structures*, 21(11):112001.

Maletta, C., Sgambitterra, E., Furgiuele, F., Casati, R., and Tuissi, A. (2014). Fatigue properties of a pseudoelastic niti alloy: Strain ratcheting and hysteresis under cyclic tensile loading. *International Journal of Fatigue*, 66:78 – 85.

Matsui, R., Tobushi, H., Furuichi, Y., and Horikawa, H. (2004). Tensile Deformation and Rotating-Bending Fatigue Properties of a Highelastic Thin Wire, a Superelastic Thin Wire, and a Superelastic Thin Tube of NiTi Alloys. *J. Eng. Mater. Technol.*, 126(4):384.

McKelvey, A. and Ritchie, R. (1999). Fatigue-crack propagation in nitinol, a shape-memory and superelastic endovascular stent material. *Journal of biomedical materials research*, 47(3):301–308.

McKelvey, A. L. and Ritchie, R. O. (2001). Fatigue-crack growth behavior in the superelastic and shape-memory alloy nitinol. *Metallurgical and Materials Transactions A*, 32(3):731–743.

Miyazaki, S., Imai, T., Igo, Y., and Otsuka, K. (1986). Effect of cyclic deformation on the pseudoelasticity characteristics of ti-ni alloys. *Metallurgical Transactions A*, 17(1):115–120.

Morgan, N. (2004). Medical shape memory alloy applications—the market and its products. *Materials Science and Engineering: A*, 378(1):16 – 23. European Symposium on Martensitic Transformation and Shape-Memory.

Morin, C., Moumni, Z., and Zaki, W. (2011a). A constitutive model for shape memory alloys accounting for thermomechanical coupling. *International Journal of Plasticity*, 27(5):748 – 767.

Morin, C., Moumni, Z., and Zaki, W. (2011b). Thermomechanical coupling in shape memory alloys under cyclic loadings: Experimental analysis and constitutive modeling. *International Journal of Plasticity*, 27(12):1959 – 1980. Special Issue In Honor of Nobutada Ohno.

Moumni, Z., Van Herpen, A., and Riberty, P. (2005). Fatigue analysis of shape memory alloys: energy approach. *Smart Mater. Struct.*, 14(5):S287–S292.

Moumni, Z., Zaki, W., and Nguyen, Q. S. (2008). Theoretical and numerical modeling of solid–solid phase change: Application to the description of the thermomechanical behavior of shape memory alloys. *Int. J. Plast.*, 24(4):614–645.

Mróz, Z. and Oliferuk, W. (2002). Energy balance and identification of hardening moduli in plastic deformation processes. *Int. J. Plast.*, 18(3):379 – 397.

Müller, C. and Bruhns, O. (2006). A thermodynamic finite-strain model for pseudoelastic shape memory alloys. *International Journal of Plasticity*, 22(9):1658 – 1682.

Nayan, N., Roy, D., Buravalla, V., and Ramamurty, U. (2008). Unnotched fatigue behavior of an austenitic ni–ti shape memory alloy. *Materials Science and Engineering: A*, 497(1):333 – 340.

Nishida, M., Tanaka, K., and Wang, H. O. (2006). Development and control of a micro biped walking robot using shape memory alloys. In *Proceedings 2006 IEEE International Conference on Robotics and Automation, 2006. ICRA 2006.*, pages 1604–1609.

Norfleet, D. M., Sarosi, P. M., Manchiraju, S., Wagner, M. F., and Uchic, M. D. (2009). Transformation-induced plasticity during pseudoelastic deformation in Ni – Ti microcrystals. *Acta Mater.*, 57(12):3549–3561.

Otsuka, K. and Kakeshita, T. (2002). Science and technology of shape-memory alloys: New developments. *MRS Bulletin*, 27(2):91–100.

Otsuka, K. and Wayman, C. M. (1999). *Shape memory materials*. Cambridge university press.

Paranjape, H. M., Paul, P. P., Sharma, H., Kenesei, P., Park, J.-S., Duerig, T., Brinson, L. C., and Stebner, A. P. (2017). Influences of granular constraints and surface effects on the heterogeneity of elastic, superelastic, and plastic responses of polycrystalline shape memory alloys. *Journal of the Mechanics and Physics of Solids*, 102:46 – 66.

Patoor, E., Lagoudas, D., Entchev, P., Brinson, L., and Gao, X. (2006a). Shape memory alloys, Part I: General properties and modeling of single crystals. *Mech. Mater.*, 38:391–429.

Patoor, E., Lagoudas, D. C., Entchev, P. B., Brinson, L. C., and Gao, X. (2006b). Shape memory alloys, part i: General properties and modeling of single crystals. *Mechanics of Materials*, 38(5):391 – 429. Shape Memory Alloys.

Pelton, A. R. (2011). Nitinol fatigue: A review of microstructures and mechanisms. *Journal of Materials Engineering and Performance*, 20(4):613–617.

Pieczyska, E., Gadaj, S., Nowacki, W. K., Hoshio, K., Makino, Y., and Tobushi, H. (2005). Characteristics of energy storage and dissipation in TiNi shape memory alloy. *Sci. Technol. Adv. Mater.*, 6:889–894.

Pieczyska, E., Tobushi, H., and Kulasinski, K. (2013). Development of transformation bands in tini sma for various stress and strain rates studied by a fast and sensitive infrared camera. *Smart Materials and Structures*, 22(3):035007.

Pieczyska, E. A., Gadaj, S. P., Nowacki, W. K., and Tobushi, H. (2006). Phase-transformation fronts evolution for stress- and strain-controlled tension tests in tini shape memory alloy. *Experimental Mechanics*, 46(4):531–542.

Pieczyska, E. A., Tobushi, H., Kulasinski, K., and Takeda, K. (2012). Impact of Strain Rate on Thermomechanical Coupling Effects in TiNi SMA Subjected to Compression. *Mater. Trans.*, 53(11):1905–1909.

Piedboeuf, M. C., Gauvin, R., and Thomas, M. (1998). Daping behavior of shape memory alloys: strain amplitude, frequency and temperature effects. *J. Sound Vib.*, 214(5):885–901.

Polatidis, E., Zotov, N., Bischoff, E., and Mittemeijer, E. (2015). The effect of cyclic tensile loading on the stress-induced transformation mechanism in superelastic niti alloys: an in-situ x-ray diffraction study. *Scripta Materialia*, 100(Supplement C):59 – 62.

Poletti, P. A., Becker, C. D., Prina, L., Ruijs, P., Bounameaux, H., Didier, D., Schneider, P. A., and Terrier, F. (1998). Long-term results of the simon nitinol inferior vena cava filter. *European Radiology*, 8(2):289–294.

Predki, W., Klönne, M., and Knopik, A. (2006). Cyclic torsional loading of pseudoelastic niti shape memory alloys: Damping and fatigue failure. *Materials Science and Engineering: A*, 417(1):182 – 189.

Rahim, M., Frenzel, J., Frotscher, M., Pfetzing-Micklich, J., Steegmüller, R., Wohlschlögel, M., Mughrabi, H., and Eggeler, G. (2013). Impurity levels and fatigue lives of pseudoelastic niti shape memory alloys. *Acta Materialia*, 61(10):3667 – 3686.

Reedlunn, B., Churchill, C. B., Nelson, E. E., Shaw, J. A., and Daly, S. H. (2014). Tension, compression, and bending of superelastic shape memory alloy tubes. *Journal of the Mechanics and Physics of Solids*, 63:506 – 537.

Rosakis, P., Rosakis, A. J., and Ravichandran, G. (2000). A thermodynamic internal variable model for the partition of plastic work into heat and stored energy in metals. *J. Mech. Phys. Solids*, 48:581–607.

Runciman, A., Xu, D., Pelton, A. R., and Ritchie, R. O. (2011). An equivalent strain/coffin–manson approach to multiaxial fatigue and life prediction in superelastic nitinol medical devices. *Biomaterials*, 32(22):4987 – 4993.

Rusinek, A. and Klepaczko, J. (2009). Experiments on heat generated during plastic deformation and stored energy for TRIP steels. *Mater. Des.*, 30(1):35–48.

Saadat, S., Salichs, J., Noori, M., Hou, Z., Davoodi, H., Bar-on, I., Suzuki, Y., and Masuda, A. (2002). An overview of vibration and seismic applications of niti shape memory alloy. *Smart Materials and Structures*, 11(2):218.

Saleeb, A., Padula, S., and Kumar, A. (2011). A multi-axial, multimechanism based constitutive model for the comprehensive representation of the evolutionary response of SMAs under general thermomechanical loading conditions. *International Journal of Plasticity*, 27(5):655 – 687.

Sanders, B., Crowe, R., and Garcia, E. (2004). Defense advanced research projects agency – smart materials and structures demonstration program overview. *Journal of Intelligent Material Systems and Structures*, 15(4):227–233.

Sangid, M. D., Maier, H. J., and Sehitoglu, H. (2011). The role of grain boundaries on fatigue crack initiation – an energy approach. *International Journal of Plasticity*, 27(5):801 – 821.

Schmidt, C., Neuking, K., and Eggeler, G. (2008). Functional fatigue of shape memory polymers. *Advanced Engineering Materials*, 10(10):922–927.

Sedlak, P., Frost, M., Benesova, B., Zineb, T. B., and Šittner, P. (2012). Thermomechanical model for niti-based shape memory alloys including r-phase and material anisotropy under multi-axial loadings. *Int. J. Plast.*, 39:132 – 151.

Sedmák, P., Pilch, J., Heller, L., Kopeček, J., Wright, J., Sedlák, P., Frost, M., and Šittner, P. (2016). Grain-resolved analysis of localized deformation in nickel-titanium wire under tensile load. *Science*, 353(6299):559–562.

Sedmák, P., Šittner, P., Pilch, J., and Curfs, C. (2015). Instability of cyclic superelastic deformation of niti investigated by synchrotron x-ray diffraction. *Acta Mater.*, 94:257 – 270.

Shaw, J. and Kyriakides, S. (1997a). Initiation and propagation of localized deformation in elasto-plastic strips under uniaxial tension. *International Journal of Plasticity*, 13(10):837 – 871.

Shaw, J. and Kyriakides, S. (1997b). On the nucleation and propagation of phase transformation fronts in a niti alloy. *Acta Materialia*, 45(2):683 – 700.

Shaw, J. A. (2000). Simulations of localized thermo-mechanical behavior in a NiTi shape memory alloy. *International Journal of Plasticity*, 16(5):541 – 562.

Shaw, J. A. and Kyriakides, S. (1995). Thermomechanical Aspects of NiTi. *J. Mech. Phys. Solids*, 43(8):1243–1281.

Simo, J. and Ju, J. (1987). Strain- and stress-based continuum damage models—i. formulation. *International Journal of Solids and Structures*, 23(7):821 – 840.

Simon, T., Kröger, A., Somsen, C., Dlouhy, A., and Eggeler, G. (2010). On the multiplication of dislocations during martensitic transformations in NiTi shape memory alloys. *Acta Mater.*, 58:1850–1860.

Siredey, N., Hautcoeur, a., and Eberhardt, a. (2005). Lifetime of superelastic Cu–Al–Be single crystal wires under bending fatigue. *Mater. Sci. Eng. A*, 396(1-2):296–301.

Sittner, P., Liu, Y., and Novak, V. (2005). On the origin of lüders-like deformation of niti shape memory alloys. *Journal of the Mechanics and Physics of Solids*, 53(8):1719 – 1746.

Sofla, A., Meguid, S., Tan, K., and Yeo, W. (2010). Shape morphing of aircraft wing: Status and challenges. *Materials & Design*, 31(3):1284 – 1292.

Song, D., Kang, G., Kan, Q., Yu, C., and Zhang, C. (2015a). Damage-based life prediction model for uniaxial low-cycle stress fatigue of super-elastic niti shape memory alloy microtubes. *Smart Mater. Struct.*, 24(8):085007.

Song, D., Kang, G., Kan, Q., Yu, C., and Zhang, C. (2015b). Experimental observations on uniaxial whole-life transformation ratchetting and low-cycle stress fatigue of super-elastic niti shape memory alloy micro-tubes. *Smart Mater. Struct.*, 24(7):075004.

Song, D., Kang, G., Kan, Q., Yu, C., and Zhang, C. (2015c). Non-proportional multiaxial whole-life transformation ratchetting and fatigue failure of super-elastic niti shape memory alloy micro-tubes. *Int. J. Fatigue*, 80:372–380.

Song, D., Kang, G., Yu, C., Kan, Q., and Zhang, C. (2017). Non-proportional multiaxial fatigue of super-elastic niti shape memory alloy micro-tubes: Damage evolution law and life-prediction model. *Int. J. Mech. Sci.*, 131:325 – 333.

Soul, H., Isalgue, A., Yawny, A., Torra, V., and Lovey, F. C. (2010). Pseudoelastic fatigue of NiTi wires : frequency and size effects on damping capacity. *Smart Mater. Struct.*, 085006.

Tanaka, K., Kobayashi, S., and Sato, Y. (1986). Thermomechanics of transformation pseudoelasticity and shape memory effect in alloys. *International Journal of Plasticity*, 2(1):59 – 72.

Tao, T., Liang, Y.-C., and Taya, M. (2006). Bio-inspired actuating system for swimming using shape memory alloy composites. *International Journal of Automation and Computing*, 3(4):366–373.

Tobushi, H., Hachisuka, T., Hashimoto, T., and Yamada, S. (1998a). Cyclic deformation and fatigue of a tini shape-memory alloy wire subjected to rotating bending. *Journal of engineering materials and technology*, 120(1):64–70.

Tobushi, H., Shimeno, Y., Hachisuka, T., and Tanaka, K. (1998b). Influence of strain rate on superelastic properties of TiNi shape memory alloy. *Mech. Mater.*, 30(2):141–150.

Tobushi, H., Takafumi, N., Yoshirou Shimeno, and Takahiro, H. (2000). Low-Cycle Fatigue of TiNi Shape Memory Alloy and Formulation of Fatigue Life. *J. Eng. Mater. Technol. ASME*, 122(2):186–191.

Tokuda, M., Ye, M., Takakura, M., and Sittner, P. (1999). Thermomechanical behavior of shape memory alloy under complex loading conditions. *Int. J. Plast.*, 15(2):223 – 239.

Van Humbeeck, J. (1991). Cycling effects, fatigue and degradation of shape memory alloys. *Le Journal de Physique IV*, 1(C4):C4–189.

Wagner, M., Sawaguchi, T., Kausträter, G., Höffken, D., and Eggeler, G. (2004). Structural fatigue of pseudoelastic NiTi shape memory wires. *Mater. Sci. Eng. A*, 378(1-2):105–109.

Wagner, M. F.-X., Nayan, N., and Ramamurty, U. (2008). Healing of fatigue damage in niti shape memory alloys. *Journal of Physics D: Applied Physics*, 41(18):185408.

Wan, V., MacLachlan, D., and Dunne, F. (2014). A stored energy criterion for fatigue crack nucleation in polycrystals. *Int. J. Fatigue*, 68:90–102.

Wang, J., Moumni, Z., and Zhang, W. (2017). A thermomechanically coupled finite-strain constitutive model for cyclic pseudoelasticity of polycrystalline shape memory alloys. *Int. J. Plast.*

Wang, Z., Hang, G., Wang, Y., Li, J., and Du, W. (2008). Embedded sma wire actuated biomimetic fin: a module for biomimetic underwater propulsion. *Smart Materials and Structures*, 17(2):025039.

Warren, J. and Wei, D. (2010). A microscopic stored energy approach to generalize fatigue life stress ratios. *Int. J. Fatigue*, 32(11):1853–1861.

Wax, S. G., Fischer, G. M., and Sands, R. R. (2003). The past, present, and future of darpa's investment strategy in smart materials. *JOM*, 55(12):17–23.

Xie, X., Kan, Q., Kang, G., Li, J., Qiu, B., and Yu, C. (2016a). Observation on the transformation domains of super-elastic niti shape memory alloy and their evolutions during cyclic loading. *Smart Materials and Structures*, 25(4):045003.

Xie, X., Kan, Q., Kang, G., Lu, F., and Chen, K. (2016b). Observation on rate-dependent cyclic transformation domain of super-elastic NiTi shape memory alloy. *Mater. Sci. Eng. A*, 671:32–47.

Yawny, A., Sade, M., and Eggeler, G. (2005). Pseudoelastic cycling of ultra-fine-grained niti shape-memory wires. *Zeitschrift fuer Metallkunde/Materials Research and Advanced Techniques*, 96(6):608–618. cited By 68.

Yin, H., He, Y., Moumni, Z., and Sun, Q. (2016). Effects of grain size on tensile fatigue life of nanostructured niti shape memory alloy. *Int. J. Fatigue*, 88:166–177.

Yin, H., He, Y., and Sun, Q. (2014). Effect of deformation frequency on temperature and stress oscillations in cyclic phase transition of NiTi shape memory alloy. *Journal of the Mechanics and Physics of Solids*, 67:100 – 128.

Yin, H., Yan, Y., Huo, Y., and Sun, Q. (2013). Rate dependent damping of single crystal CuAlNi shape memory alloy. *Materials Letters*, 109:287 – 290.

Yu, C., Kang, G., and Kan, Q. (2014). A physical mechanism based constitutive model for temperature-dependent transformation ratchetting of NiTi shape memory alloy: One-dimensional model. *Mech. Mater.*, 78:1–10.

Yu, C., Kang, G., and Kan, Q. (2015a). A micromechanical constitutive model for anisotropic cyclic deformation of super-elastic niti shape memory alloy single crystals. *J. Mech. Phys. Solids*, 82:97–136.

Yu, C., Kang, G., Kan, Q., and Zhu, Y. (2015b). Rate-dependent cyclic deformation of super-elastic niti shape memory alloy: Thermo-mechanical coupled and physical mechanism-based constitutive model. *Int. J. Plast.*, 72:60–90.

Zaki, W. and Moumni, Z. (2007a). A 3D model of the cyclic thermomechanical behavior of shape memory alloys. *J. Mech. Phys. Solids*, 55(11):2427–2454.

Zaki, W. and Moumni, Z. (2007b). A three-dimensional model of the thermomechanical behavior of shape memory alloys. *Journal of the Mechanics and Physics of Solids*, 55(11):2455 – 2490.

Zhang, S. and He, Y. (2017). Fatigue resistance of branching phase-transformation fronts in pseudoelastic niti polycrystalline strips. *International Journal of Solids and Structures*.

Zhang, X., Feng, P., He, Y., Yu, T., and Sun, Q. (2010). Experimental study on rate dependence of macroscopic domain and stress hysteresis in niti shape memory alloy strips. *International Journal of Mechanical Sciences*, 52(12):1660 – 1670.

Zhang, Y., You, Y., Moumni, Z., Anlas, G., Zhu, J., and Zhang, W. (2017). Experimental and theoretical investigation of the frequency effect on low cycle fatigue of shape memory alloys. *Int. J. Plast.*, 90:1 – 30.

Zhang, Y., Zhu, J., Moumni, Z., and Zhang, W. (2016). Energy-based fatigue model for shape memory alloys including thermomechanical coupling. *Smart Mater. Struct.*, 25(3):035042.

Zheng, L., He, Y., and Moumni, Z. (2016a). Effects of lüders-like bands on niti fatigue behaviors. *International Journal of Solids and Structures*, 83(Supplement C):28 – 44.

Zheng, L., He, Y., and Moumni, Z. (2016b). Lüders-like band front motion and fatigue life of pseudoelastic polycrystalline niti shape memory alloy. *Scripta Mater.*, 123:46–50.

Zheng, L., He, Y., and Moumni, Z. (2017). Investigation on fatigue behaviors of niti polycrystalline strips under stress-controlled tension via in-situ macro-band observation. *International Journal of Plasticity*, 90:116 – 145.

Zhu, S. and Zhang, Y. (2007). A thermomechanical constitutive model for superelastic SMA wire with strain-rate dependence. *Smart Mater. Struct.*, 16(5):1696–1707.

universite
PARIS-SACLAY

ÉCOLE DOCTORALE
Sciences mécaniques et
énergétiques, matériaux
et géosciences (SMEMAG)

Titre : Fatigue à faible nombre de cycles des matériaux à mémoire de forme

Mots clés : materiaux a memoire de forme, fatigue à faible nombre de cycles, couplage thermomecanique, critère de fatigue, énergie stockée, l'initiation des fissures.

Résumé : Dans cette thèse, nous proposons une analyse globale multi-échelles de la fatigue à faible nombre de cycles des matériaux à mémoire de forme (MMF). Dans un premier temps, une large campagne d'essais a été menée pour différents chargements thermomécaniques comprenant des tests de fatigue sous contrainte et déformation imposée et pour différentes fréquences de chargement. A partir des résultats des essais, un critère de fatigue, basé sur l'énergie de déformation, a été développé ; on montre que l'énergie de déformation est un paramètre pertinent pour prédire la fatigue des MMF en tenant compte du couplage thermomécanique et du type de chargement : contrainte ou déformation imposée. Ensuite, en prenant appui sur la répartition de l'énergie de l'hystérésis en dissipation et énergie stockée, on avance une interprétation physique du mécanisme de la fatigue des MMF. Dans la troisième partie, on propose une modélisation multi-échelles de l'initiation des fissures de fatigue dans les MMF à partir de la notion de plasticité de transformation (PlTr). Dans ce cadre, on montre que la fatigue de MMF est contrôlée par la (PlTr) et que la température maximale lors de la transformation de phase est le paramètre à retenir pour prédire la rupture par fatigue des MMF. Le modèle permet également de prédire le lieu d'initiation des premières fissures de fatigue. Enfin, un procédé – fondé sur l'«éducation» des MMF – permettant d'améliorer la résistance à la fatigue est proposé.

Title : Low cycle fatigue of shape memory alloys

Keywords : shape memory alloys, low-cycle fatigue, thermomechanical coupling, fatigue criterion, stored energy, crack initiation.

Abstract : The thesis proposes a multi-scale comprehensive analysis of low cycle fatigue of shape memory alloys (SMAs). First, low cycle fatigue of SMAs is experimentally investigated; comprehensive tensile-tensile fatigue tests under both stress and strain controlled loadings at different frequencies are carried out and results are discussed. Second, a new strain energy-based fatigue criterion is developed; it is shown that the use of total strain energy is a relevant parameter to predict fatigue lifetime of SMAs for different thermomechanical conditions and under different types (strain-control or stress-control) loadings. A physical interpretation of the mechanism related to the low-cycle fatigue of SMAs is then provided based on the conversion of hysteresis work into dissipation and stored energy. Third, fatigue crack initiation during cyclic stress-induced phase transformation is modeled based on transformation induced plasticity (TRIP); it is shown that the maximum temperature during the cyclic loading is a relevant indicator of the fatigue of SMA. Furthermore, the effect of the macroscopic mechanical load on the the fatigue lifetime is addressed as well as the spatial location of crack initiation. Finally, a mechanical training process that allows enhancing resistance to low cycle fatigue of SMAs is proposed.

Université Paris-Saclay
Espace Technologique / Immeuble Discovery
Route de l'Orme aux Merisiers RD 128 / 91190 Saint-Aubin, France